ractor Report 4035

rt Composite Fuselage
logy—Impact Dynamics
oustic Transmission

, F. J. Balena, W. L. LaBarge,
Pitman, and G. Wittlin

1-17698

NASA Contractor Report 4035

Transport Composite Fuselage Technology—Impact Dynamics and Acoustic Transmission

A. C. Jackson, F. J. Balena, W. L. LaBarge,
G. Pei, W. A. Pitman, and G. Wittlin
Lockheed-California Company
Burbank, California

Prepared for
Langley Research Center
under Contract NAS1-17698

National Aeronautics
and Space Administration

**Scientific and Technical
Information Branch**

1986

FOREWORD

This is the final report of the program completed by Lockheed-California Company, "Transport Composite Fuselage Technology - Impact Dynamics and Acoustic Transmission," under contract NAS1-17698. This program was conducted from May 1984 to October 1986. The program was sponsored by the National Aeronautics and Space Administration (NASA) Langley Research Center. The program manager for Lockheed was Mr. Arthur M. James. Mr. Herman L. Bohon and Mr. John G. Davis, Jr. were project managers for NASA Langley. The technical representatives for NASA, Langley were Mr. Andrew Chapman and Mr. Marvin Dow.

The following personnel were principal contributors to the program.

Lockheed-California Company

A. C. Jackson	Engineering Manager
F. J. Balena	Acoustics
M. J. Berg	Quality Assurance
C. S. Carayanis	Stress
G. Hull	Materials and Processes
W. L. LaBarge	Aeromechanics
L. J. Linner	Weights
M. Y. Niu	Design
G. Pei	Manufacturing Research
J. Soovere	Aeromechanics
G. Wittlin	Aeromechanics
C. A. Woods	Stress

Lockheed-Georgia Company

W. A. Pitman	Engineering Manager

Consultants (Acoustics Methodology)

L. D. Koval

L. D. Pope

CONTENTS

Page

FOREWORD iii

LIST OF ILLUSTRATIONS vii

LIST OF TABLES xii

SUMMARY. 1

INTRODUCTION 1

1. PRELIMINARY DESIGN OF COMPOSITE FUSELAGE. 3
1.1 Baseline Fuselage Configurations 3
1.1.1 Weight estimates. 6
1.2 Design Requirements for Impact Dynamics. 6
1.2.1 KRASH modeling. 6
1.2.2 Development test plan 13
1.3 Acoustic Transmission Investigation. 16
1.3.1 Acoustic transmission considerations. 16
2. ANALYSIS DEVELOPMENT. 26
2.1 Impact Dynamics Analysis Development 26
2.2 Acoustic Transmission Analysis Development 28
2.2.1 TBL induced interior noise: Comparison of predictions with measurements for a conventional aluminum fuselage. . 29
2.2.2 Performance of a composite fuselage 32
2.2.3 Analysis of the baseline cylinders. 36
3. TOOLING AND FABRICATION 42
3.1 Tooling and Fabrication of Impact Dynamics Specimens 42
3.2 Tooling and Fabrication of Acoustic Cylinder 48
3.2.1 Shell fabrication 52
3.2.2 Assembly. 57
4. TECHNOLOGY DEMONSTRATION. 60
4.1 Panel Static Tests 60
4.1.1 Blade-stiffened metal panel 62
4.1.2 Hat-stiffened composite panel 62
4.1.3 Blade-stiffened composite panel 62
4.1.4 Corrugated composite panel. 66
4.1.5 Summary of panel static test results. 66
4.1.6 Analysis versus test. 68
4.2 Modified Composite Panel Static Tests. 71
4.2.1 Chamfered corrugated composite panels 71
4.2.1.1 Short panel. 71
4.2.1.2 Long panel 71
4.2.2 Chamfered hat-stiffened composite panel 75

CONTENTS (Continued)

Page

4.2.3 Chamfered hat-stiffened composite panel with composite bracket attachments 77
4.2.4 Summary of modified composite panel static test results . 82
4.3 Modified Composite Panel Dynamic Tests 82
4.3.1 Chamfered corrugated panels 82
4.3.2 Chamfered hat-stiffened panels with mechanically fastened attachment brackets. 87
4.3.3 Chamfered hat-stiffened panel with bonded attachment bracket. 90
4.3.4 Summary of modified composite panel dynamic test results. 91
4.4 Summary of Frame Segments Static Tests Results 91
4.5 Summary of Results 95
5. CONCLUDING REMARKS. 97
REFERENCES. 98
APPENDIX A. A-1
A1.1 Analytical Procedures. A-1
A1.2 Program LDCURVE. A-2
A2.0 STATIC FAILURE LOAD PREDICTION. A-3
A2.1 Section Properties A-3
A2.1.1 Metal section properties. A-3
A2.1.2 Composite section properties. A-4
A2.2 Stiffness Properties of Composite Sections A-4
A2.3 Panels Subjected to Compression Loads. A-6
A2.3.1 Stiffened metal panels. A-6
A2.3.2 Composite specimens A-6
A2.3.3 Corrugated panels A-7
A2.4 Fuselage Frame Sections. A-7
A2.4.1 Metal specimens A-7
A2.4.2 Composite specimens A-7
A3.0 LOAD DEFLECTION CURVE A-8
A3.1 Post Failure Load Deflection Curve A-8
A3.1.1 Plastic hinge curve A-8
A3.1.2 Exponential curve A-10
A3.2 Total Load Deflection Curve. A-10
REFERENCES. A-11
APPENDIX B. B-1
REFERENCES. B-42

LIST OF ILLUSTRATIONS

Figure		Page
1	ATX-350I general arrangement.	4
2	Aluminum baseline ATX-350I barrel section	5
3	Composite baseline ATX-350I barrel section.	7
4	Widebody airplane KRASH stick model	10
5	Time history of fuselage frame crushing	11
6	Baseline airplane shear-web frame model	12
7	Baseline airplane frame load-deflection history	13
8	Estimated load deflection requirement for cargo floor support structure	15
9	Stiffened panel elements.	17
10	Frame panel elements.	18
11	Baseline aluminum acoustic cylinder design.	20
12	Baseline composite acoustic cylinder design	23
13	Structural configuration acoustic test cylinder	24
14	Frame configuration	24
15	Stringer configuration.	25
16	Section showing floor support structure	25
17	Floor-to-shell connection	26
18	View of cylinder showing floor support structure.	27
19	Aircraft configuration.	30
20	Interior measurements	31
21	Comparison of predicted interior noise with measured interior noise (aluminum fuselage).	34
22	Predicted interior noise levels composite and aluminum fuselage (equivalent strength designs)	35
23	Aluminum and composite cylinder noise reductions with 1.25 kg/m^2 trim and carbon dioxide exterior	40
24	Aluminum cylinder noise reductions with variable trim and carbon dioxide exterior	40
25	Composite cylinder noise reductions with variable trim and carbon dioxide exterior.	41

LIST OF ILLUSTRATIONS (Continued)

Figure		Page
26	Composite cylinder noise reductions with 1.25 kg/m^2 trim with and without carbon dioxide exterior	41
27	Hat stiffened panel tooling	42
28	Cured hat stiffened panels.	43
29	Z-C frame tooling	44
30	Completed Z-C frame	44
31	Z-C frames and skin assembly.	45
32	Blade stiffened panel tooling	45
33	Blade stiffened panel curing tool	46
34	Prepreg laid into ceramic for sine-wave panel tool.	47
35	Composite/rubber tooling for corrugated stiffened panel	47
36	Cutting of flanges for straight sine wave	49
37	Corrugated stiffened composite panel.	49
38	Composite tool for corrugated frame	50
39	Cutting of flanges for curved corrugated stiffener.	50
40	Composite corrugated frame/skin test panel.	51
41	Mandrel mounted in filament winder.	51
42	Cross section of frame tool	52
43	Stringer tool	53
44	Winding of first ± 45-degree plies in progress.	53
45	The winding complete.	55
46	Wound shell trimmed for bagging	55
47	Caul sheets in place.	56
48	The shell being moved into position for support structure assembly.	56
49	The frames being preassembled and drilled prior to installation .	58
50	The frames installed with the aid of a spacer	58
51	Aluminum substructure to support a plywood floor.	59
52	Completed fuselage section.	59
53	Load deflection and energy absorption parameters.	61
54	Predicted load-deflection curve for below cargo floor structure .	61

LIST OF ILLUSTRATIONS (Continued)

Figure		Page
55	Deflected shape of test specimen prior to failure of stiffeners, blade-stiffened metal panel	63
56	Measured load versus deflection, blade-stiffened metal panel. . .	63
57	Failed panel from stiffener side, hat-stiffened composite panel .	64
58	Measured load versus deflection, hat-stiffened composite panel. .	64
59	Failed panel from stiffener side, blade-stiffened composite panel	65
60	Measured load versus deflection, blade-stiffened composite panel	65
61	Corrugated composite panel, failed specimen	66
62	Load versus deflection, corrugated composite panel.	67
63	Pre-tested predicted load deflection curve versus measured load deflection curve, blade-stiffened metal panel.	68
64	Predicted failure load versus effective skin width.	69
65	Modified predicted load deflection curve versus measured load deflection curve, blade-stiffened metal panel.	70
66	Hat-stiffened panel test configurations, failure modes and load deflection curves	72
67	Short corrugated composite panel salvaged from composite panel concept #2.	73
68	Short corrugated composite panel, failed specimen	73
69	Load versus deflection, short corrugated composite panel.	74
70	Long corrugated composite panel design	74
71	Long corrugated composite panel, failed specimen	75
72	Load versus deflection, long corrugated composite panel	76
73	Hat-stiffened chamfered composite panel cut lines	76
74	Chamfered hat-stiffened composite panel failed specimen - stiffener side	77
75	Load versus deflection, chamfered hat-stiffened composite panel .	78
76	Bracket test specimens.	79
77	Composite angle bracket attachment.	80

LIST OF ILLUSTRATIONS (Continued)

Figure		Page
78	Hat-stiffened composite panel/composite bracket load versus deflection curve.	81
79	Hat-stiffened composite panel/composite bracket brooming failure detail	81
80	Hat-stiffened composite panel/composite bracket post-failure specimen	82
81	Short corrugated composite column pre-dynamic test arrangement. .	84
82	Corrugated composite panel load versus deflection curve - impact velocity 10 ft/sec.	85
83	Failed corrugated composite dynamic test specimen - impact velocity 10 ft/sec.	86
84	Corrugated composite panel load versus deflection curve - impact velocity 13.9 ft/sec.	86
85	Failed corrugated composite dynamic test specimen - impact velocity 13.9 ft/sec.	87
86	Hat-stiffened composite panel/composite bracket load versus delection - impact velocity 11 ft/sec	88
87	Hat-stiffened composite panel/composite bracket brooming failure details - impact velocity 11 ft/sec.	88
88	Hat-stiffened composite panel/composite bracket post-failure specimens - impact velocity 11 ft/sec.	89
89	Hat-stiffened composite panel/bracket (one end) load versus deflection curve - impact velocity 13 ft/sec.	89
90	Hat-stiffened composite panel/bonded bracket load versus deflection - impact velocity 12 ft/sec.	90
91	Hat-stiffened composite panel/bonded bracket brooming failure mode - impact velocity 12 ft/sec.	91
92	Test setup for aluminum frame segment	92
93	Load versus deflection, aluminum frame segment.	93
94	Measured load versus deflection, composite frame #1	93
95	Measured load versus deflection, composite frame #2	94
96	Deformed shape for the aluminum frame segment	94
97	Combined panel - frame static load deflection curves.	96
A-1a	LDCURVE program flow diagram routine.	A-4

LIST OF ILLUSTRATIONS (Continued)

Figure		Page
A-1b	Flow diagram - program LDCURVE.	A-5
A-2	Stiffened panel segment during post failure deformation	A-9
A-3	Post-failure load-deflection curves	A-9
B-1	Acoustic transmission prediction program.	B-2
B-2	Acoustic analysis flow diagram.	B-2
B-3	Geometry of stiffener	B-21
B-4	Circular cylindrical shell with a longitudinal partition.	B-29

LIST OF TABLES

Tables		Page
1	ATX-350I Fuselage Weight Breakdown	8
2	Advanced Composite Fuselage Baseline Weight Savings	9
3	Maximum Beam Loads Twenty-Inch Frame Segment (1 Bay)	14
4	Summary of Impact Dynamics Concept Development Tests	16
5	Design Criteria for Noise Attentuation Demonstration Test Specimens	22
6	Acoustic Cylinder Weights	22
7	Aircraft Fuselage and Trim Characteristics	33
8	Composite Fuselage Shell	36
9	Structural and Cavity Modes for Baseline Cylinders	38
10	Predicted Noise Reductions for Baseline Cylinders	39
11	Comparison of Stiffened Panel Test Results	67
12	Energy Absorption Parameter Summary, Blade-Stiffened Metal Panel	70
13	Bracket Test Results	79
14	Static Test Results, Modified Composite Panels At 2 Inch Crushing Deflection	83
15	Static Test Results, Modified Composite Panels At 6 Inch Crushing Deflection	83
16	Dynamic Test Results, Modified Composite Panels	92
17	Comparison of Frame Segment Test Results	95

TRANSPORT COMPOSITE FUSELAGE TECHNOLOGY - IMPACT DYNAMICS AND ACOUSTIC TRANSMISSION

FINAL REPORT

A. C. Jackson, F. J. Balena, W. L. LaBarge, G. Pei, W. A. Pitman
and G. Wittlin

SUMMARY

A program was performed to develop and demonstrate the impact dynamics and acoustic transmission technology for a composite fuselage which meets the design requirements of a 1990 large transport aircraft without substantial weight and cost penalties.

The program developed the analytical methodology for the prediction of acoustic transmission behavior of advanced composite stiffened shell structures. The methodology predicted that the interior noise level in a composite fuselage due to turbulent boundary layer will be less than in a comparable aluminum fuselage. The verification of these analyses will be performed by NASA Langley Research Center using a composite fuselage shell fabricated by filament winding.

The program also developed analytical methodology for the prediction of the impact dynamics behavior of lower fuselage structure constructed with composite materials. Development tests were performed to demonstrate that the composite structure designed to the same operating load requirement can have at least the same energy absorption capability as aluminum structure.

INTRODUCTION

Secondary and empennage composite structures for civil and military transport aircraft have been successfully developed under the Aircraft Energy Efficiency (ACEE) Program. The cost and weight benefits of such composite structures have been validated by the design, manufacture, and test of several components. Confidence in these applications has been achieved through interface with Federal Aviation Administration (FAA) and the airlines. These programs are complete, and the aircraft manufacturers are beginning to incorporate versions of such structures in plans for future aircraft.

Composite technology for secondary and empennage structures is now considered state of the art. The major payoff will come with the application of composites to primary structure, which comprises about 75 percent of transport structural weight. However, a comprehensive data base is needed to assure that both technical and financial risks are acceptable before incorporating these materials into safety-of-flight structure. The Advanced Composite

Structures Technology (ACST) program was initiated to develop a composites primary airframe structures technology data base that achieves the full potential of weight and cost savings available for the design of U.S. civil and military transport aircraft in the early 1990s. As part of the ACST program, this contract addressed long-lead-time critical technology for composite fuselage structure identified by the National Aeronautics and Space Administration (NASA), other Government agencies, and industry-sponsored programs. The primary objective of this conract was to develop and demonstrate the impact dynamics and acoustic transmission technology for a composite fuselage which meets all design requirements of a 1990 large transport aircraft without substantial weight and cost penalties.

The Lockheed-California Company was teamed with the Lockheed-Georgia Company in this program. Lockheed-California Company, as prime, contractor, had overall program responsibility and performed the bulk of the effort. Lockheed-Georgia Company was responsible for the design and fabrication of an acoustics demonstration test article, a 5-1/2 foot diameter 12 foot long composite fuselage barrel section.

Use of commercial products or names of manufacturers in this report does not constitute official endorsement of such products or manufacturers, either expressed or implied, by the National Aeronautics and Space Administration.

ABBREVIATIONS AND SYMBOLS

ACEE	Aircraft Energy Efficiency
ACST	Advanced Composites Structures Technology
CO_2	Carbon Dioxide
EA	Average Modulus x Cross-Sectional Area
ET	Average Modulus x thickness
FAA	Federal Aviation Administration
fr	Frequency Ratio
FRL	Fuselage Reference Line
FS	Fuselage Station
Gt	Average Shear Modulus x Thickness
Hz	Hertz
KEAS	Knots Equivalent Air Speed

KIAS	Knots Indicated Air Speed
LaRC	Langley Research Center
LUR	Load Uniformity Ratio
M	Mach Number
NASA	National Aeronautics and Space Administration
TBL	Turbulent Boundary Layer

1. PRELIMINARY DESIGN OF COMPOSITE FUSELAGE

1.1 Baseline Fuselage Configurations

Preliminary designs were developed for two ATX-350I widebody fuselage barrel sections - one made of aluminum and one made of advanced composites. The ATX-350I was used in the Study Program (Reference 1) which preceded this Technology Program. Both fuselage segments were designed to the same structural criteria and are representative of a location just aft of the wing box. These barrel section designs were used as the baselines for a weight comparison of two complete fuselages. These designs were also used as the baseline for analytical studies and design improvements in the areas of acoustic transmission and impact dynamics.

The ATX-350I fuselage has the same diameter as the L-1011, but is approximately 26 feet longer. The aircraft general arrangement is shown in Figure 1. Bending moments were calculated for the lengthened fuselage, and the resulting loads used to design the skin and stringers of both barrel sections. The frames were designed to the same stiffness as a typical L-1011 aft fuselage frame. The remaining components were designed using the critical loads and the design methodologies of the aft fuselage components of the L-1011.

The aluminum fuselage baseline design, shown in Figure 2 is similar to the design of the L-1011, although the skin and stringers were resized to carry the higher loads of the ATX-350I. The upper and lower portions of the skin incorporate Z-section stiffeners spaced 8.5 inches apart. The sidewalls (roughly from the cabin floor to the top of the passenger door) are stringerless. The frames for the aluminum design are channel sections spaced 20 inches apart, and attached to the skin with shear clips. The frames are six inches deep in the top portion of the fuselage, and five inches deep below the passenger floor, but only three inches deep at the windows. Because of this narrowing of the frames and the lack of stiffeners in the sidewalls, the skin is relatively thick at that location. The cabin floor is supported by a J-shaped cross-beam and a pair of I-shaped floor posts at every frame location. The cargo floor is supported by a T-shaped cross-beam and a stiffened shear web at the same locations.

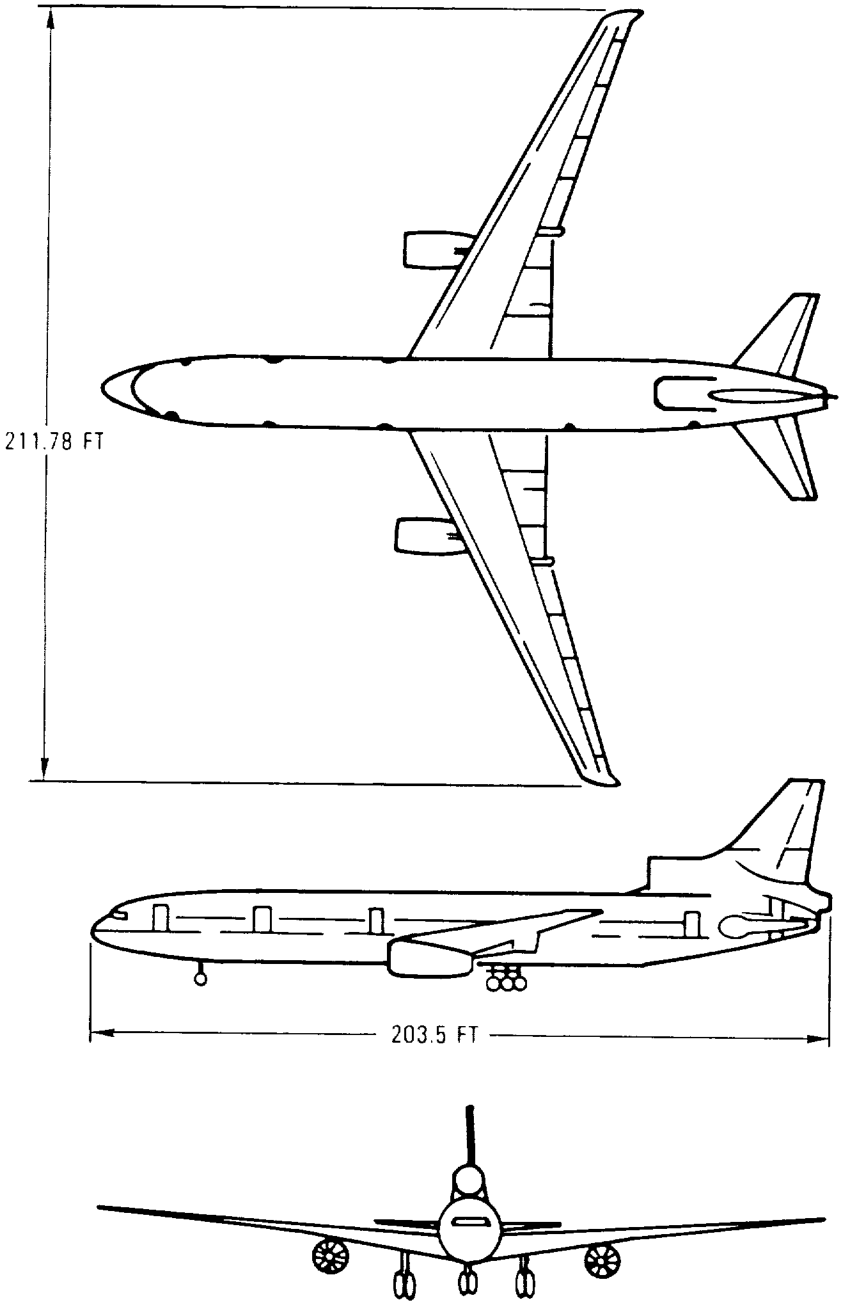

Figure 1. - ATX-350I general arrangement.

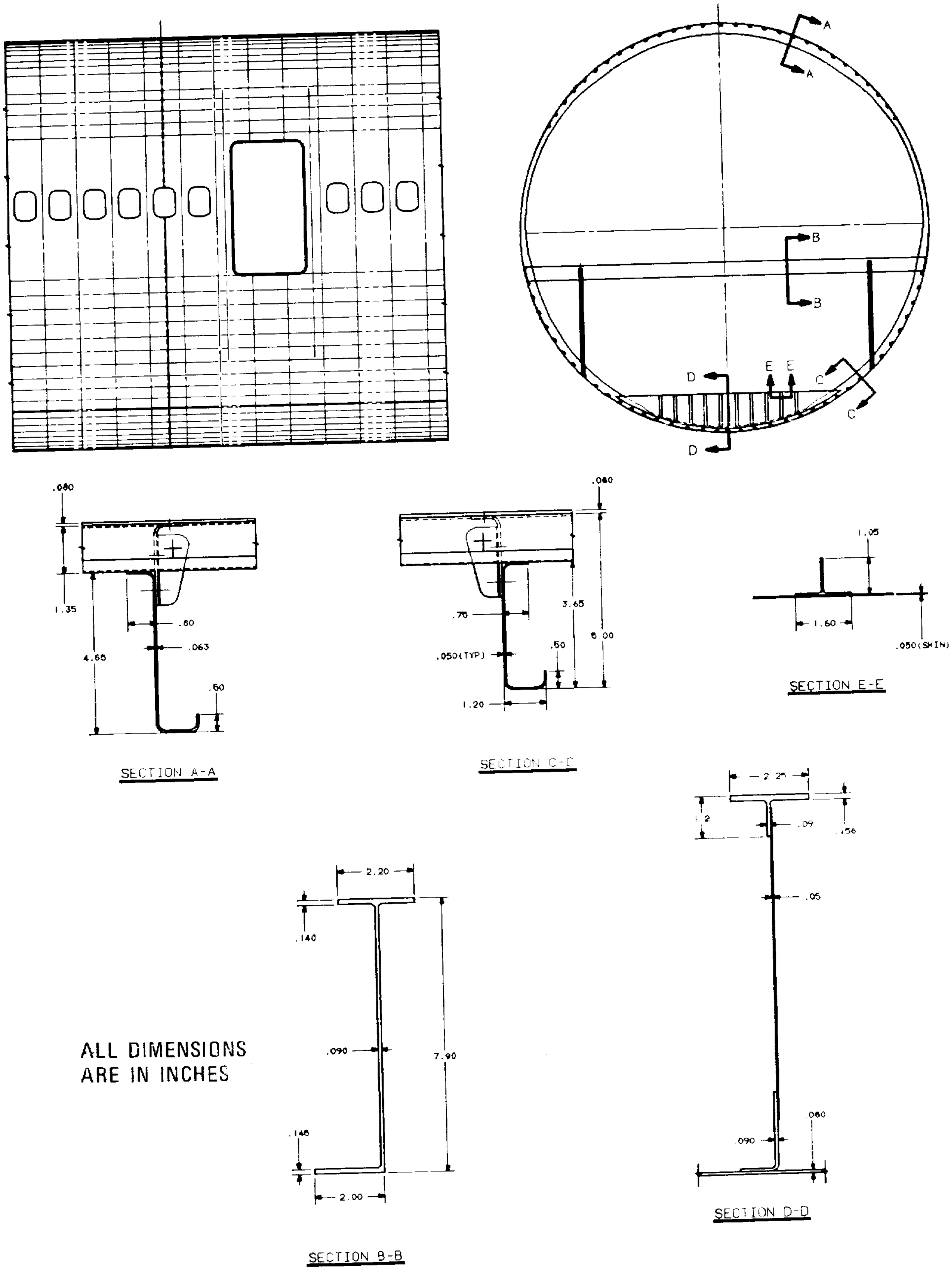

Figure 2. - Aluminum baseline ATX-350I barrel section.

The composite baseline design, shown in Figure 3, consists of J-stiffened skins in the upper and lower portions. Like the aluminum design, it is stringerless on the sides. The J-stiffened skin was selected from among the options considered because of its relative ease of fabrication and installation, lack of problems with fluids in bilge areas, and supportability. The composite frames are Z-sections with integral shear clips. The frame depth was kept constant at six inches for the composite design, with 0° plies added to the flanges in the top and bottom portions of the fuselage to match the stiffnesses of the aluminum frames at those locations. The spacings for both the stringers and the frames remained the same as in the aluminum designs. Also unchanged were the basic shapes and overall dimensions of the cabin and cargo floor beams, the floor posts, and the cargo sub-floor webs, although each of these components was redesigned using composite materials to meet the same criteria as its aluminum counterpart. Cross sections of some of these components of the composite baseline are shown in Figure 3.

1.1.1 Weight estimates.- The weight of the ATX-350I baseline aluminum fuselage was determined parametrically, and a breakdown of fuselage component weight was derived based on L-1011-1 data. This breakdown is shown in Table 1.

Table 2 presents the effect of applying the derived weight savings to the total fuselage of the ATX-350I. Column 1 presents the fuselage baseline weight from Table 1. Column 2 shows the percentage of metallic structure converted to advanced composites. The weight of the composite fuselage components is shown in Column 3. Column 4 shows the weight savings for converting to composites. The total weight saving is 17.9 percent.

1.2 Design Requirements for Impact Dynamics.

1.2.1 KRASH modeling.- Digital computer program KRASH, developed under U.S. Army (Reference 2) and FAA (Reference 3) sponsorship was used to obtain transport airplane structural responses under crash impact conditions. A previously developed widebody airplane model (Reference 4) was refined and analyzed for a range of impact conditions. The stick model consisting of 18 mass elements, interconnected by 17 beam elements and 15 crush springs, is shown in Figure 4. The inertia and stiffness properties, and aerodynamic forces were included in the model definition. The aerodynamic, stiffness and inertia forces were balanced to simulate one-g sea level flight at a forward speed of 163 KEAS.

ORIGINAL PAGE IS OF POOR QUALITY

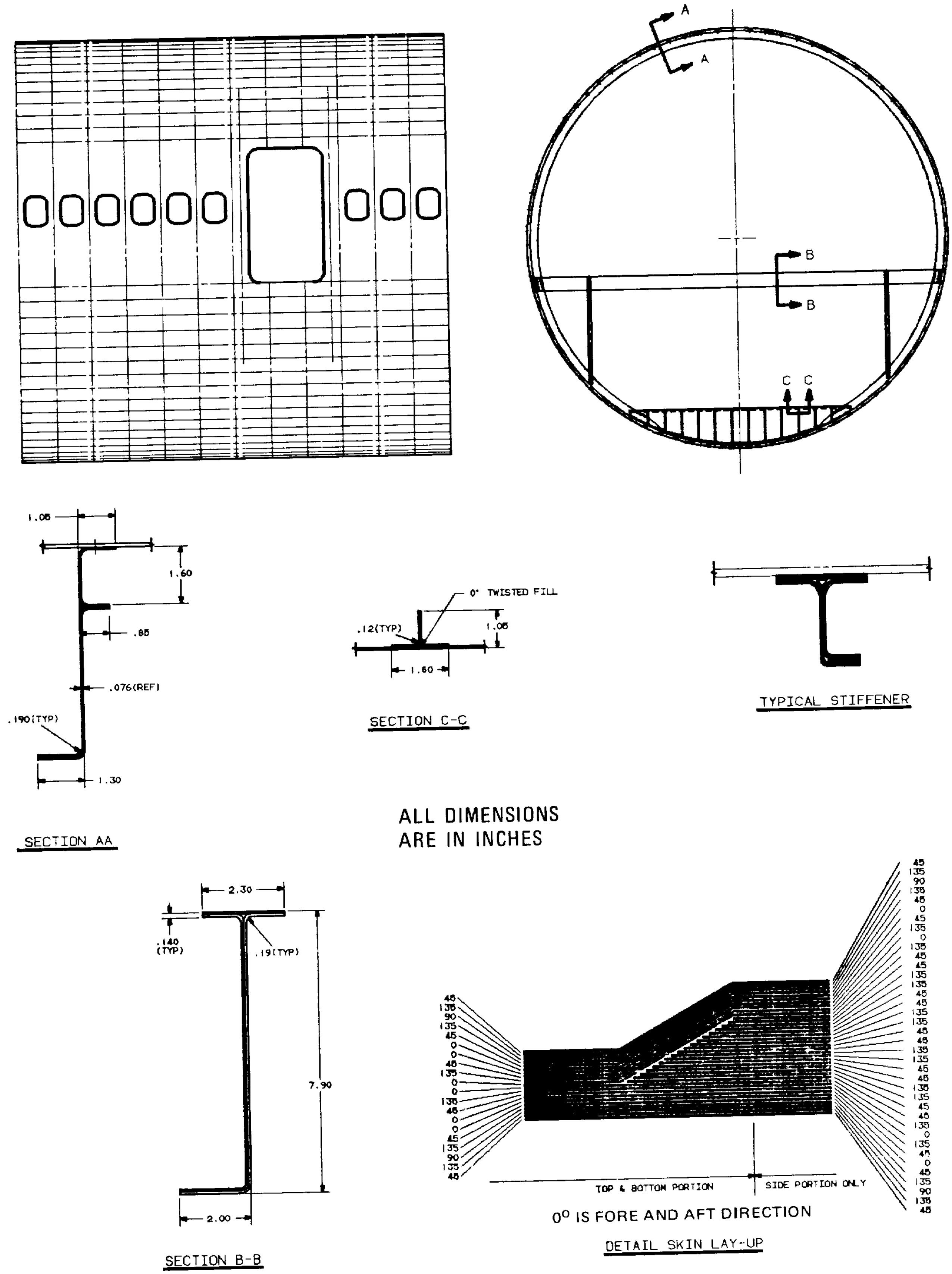

Figure 3. - Composite baseline ATX-350I barrel section.

TABLE 1. - ATX-350I FUSELAGE WEIGHT BREAKDOWN

	Baseline Weight (lb)		% Total Weight
Covering		(19466)	29.3
Skin	14573		
Manufacturing Joints	1127		
Door Surrounds	3766		
Stringers and Longerons		(4691)	7.1
Joints, Splices, and Fasteners		(1024)	1.5
Bulkheads		(7282)	10.9
Minor Frames		(5378)	8.1
Pressure Deck Assembly		(4793)	7.2
Pressure Deck	1633		
Keelson Web	3160		
Floor Support		(6592)	9.9
Flooring and Fairing		(4564)	6.9
Door Structure		(3508)	5.3
Windows		(2442)	3.7
Misc.		(6738)	10.1
Paint and Misc.	623		
APU Support	246		
Seat Tracks	1642		
Cockpit Flooring and Supports	330		
Doors Mechanisms	3011		
Miscellaneous	886		
		66478	100.0

NOTE: Major categories of weight shown in parentheses.

For all analyses a design landing speed of 163 KEAS and a sink speed of 10 ft/sec were used. The 10 ft/sec sink speed is two times the current emergency landing condition requirements, Reference 5. The airplane pitch angle was varied from 2.1 degrees nose-down to 4.4 degrees nose-up.

TABLE 2. - ADVANCED COMPOSITE FUSELAGE BASELINE WEIGHT SAVINGS

	1 Baseline Metal Fus. Wt	2 % of Struc. Conv to Composites	3 Composite Fus Wt	4 % Wt Saving
Covering	19466	100.0	15534	20.2
Stringers & Longeron	4691	100.0	2618	44.2
Jnts, Spl. Fast	1024	10.0	819	[20.0]
Bulkheads	7282	66.4	6190	[15.0]
Minor Frames	5378	100.0	4168	22.5
Press Deck Assy	4793	93.2	4074	[15.0]
Floor Support	6592	100.0	4476	32.1
Floor & Fairing	4564	0.0	4564	0.0
Door Structure	3508	87.0	2982	[15.0]
Windows	2442	0.0	2442	0.0
Misc.	6738	0.0	6738	0.0
TOTAL	66478	73.1	54605	17.9

*Due to reduction in number of fasteners.
[] - denotes assumed savings - not sized by analysis

The primary purpose of the calculations was to determine the location and degree of frame crushing of the fuselage underside for a range of impact attitudes. Mass point locations 1, 2, 4, 5, and 8 in Figure 4 represent "hard points" such as major bulkhead structure, and mass point locations 3, 6, and 7 represent forward (FS 677), mid (FS 1424) and aft (FS 1663) frame crushing regions, respectively.

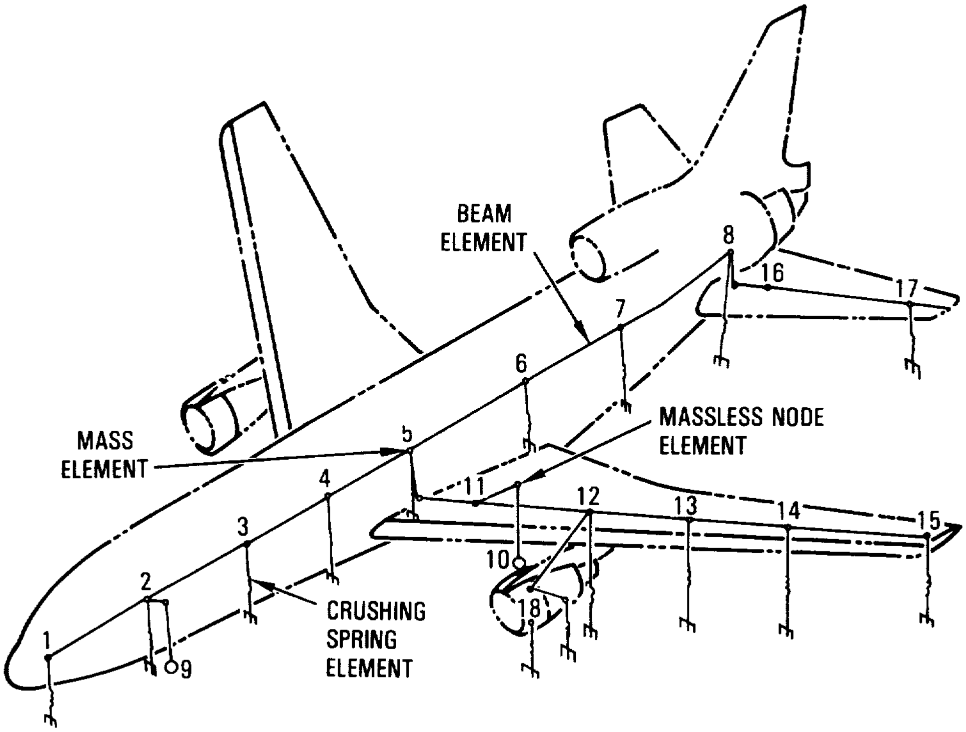

Figure 4. - Widebody airplane KRASH stick model.

The analytical results shown in Figure 5 indicate that crushing of the forward section takes place only during the nose down and zero attitude cases. During these impact conditions, the forward fuselage crush is just under three inches. The nose up cases indicate that severe crushing (10 to 15 inches peak) of the aft sections of the fuselage can occur. The time history of the fuselage frame crushing is shown in Figure 5, for fuselage stations 677, 1424, and 1663.

The analysis indicated that the aft fuselage crushing is more severe than the forward fuselage. It was thus the prime region to be investigated during this study.

An analysis was performed for the metal frame being used as the baseline design for this project. The KRASH model is shown in Figure 6. The fuselage segment represented a 2454-pound section including occupant and cargo loading. The load-deflection-time curve is shown in Figure 7. The results of the analysis indicate that approximately 80 percent of the strain and crushing energy occurs below the cargo floor. An additional 13 percent is absorbed by the frame between the cargo floor and passenger vertical floor post location (beam 3-4, Figure 6).

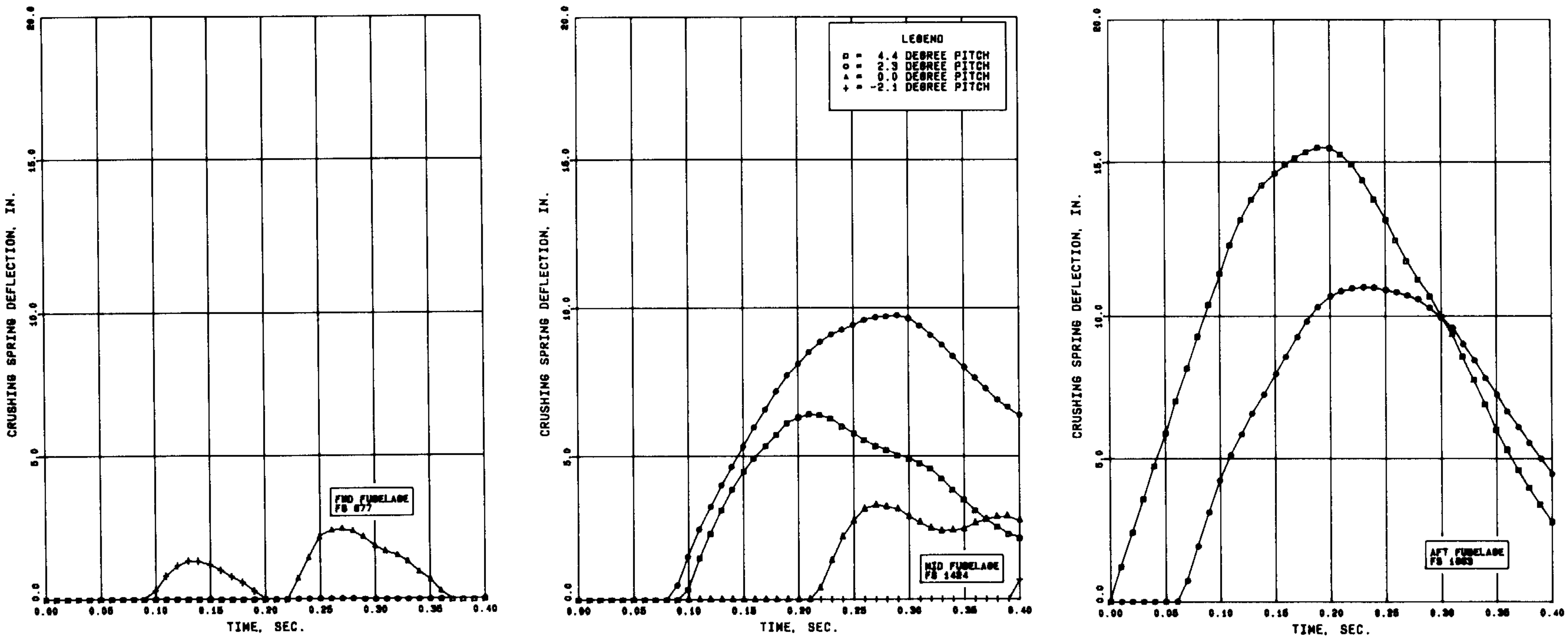

Figure 5. - Time history of fuselage frame crushing

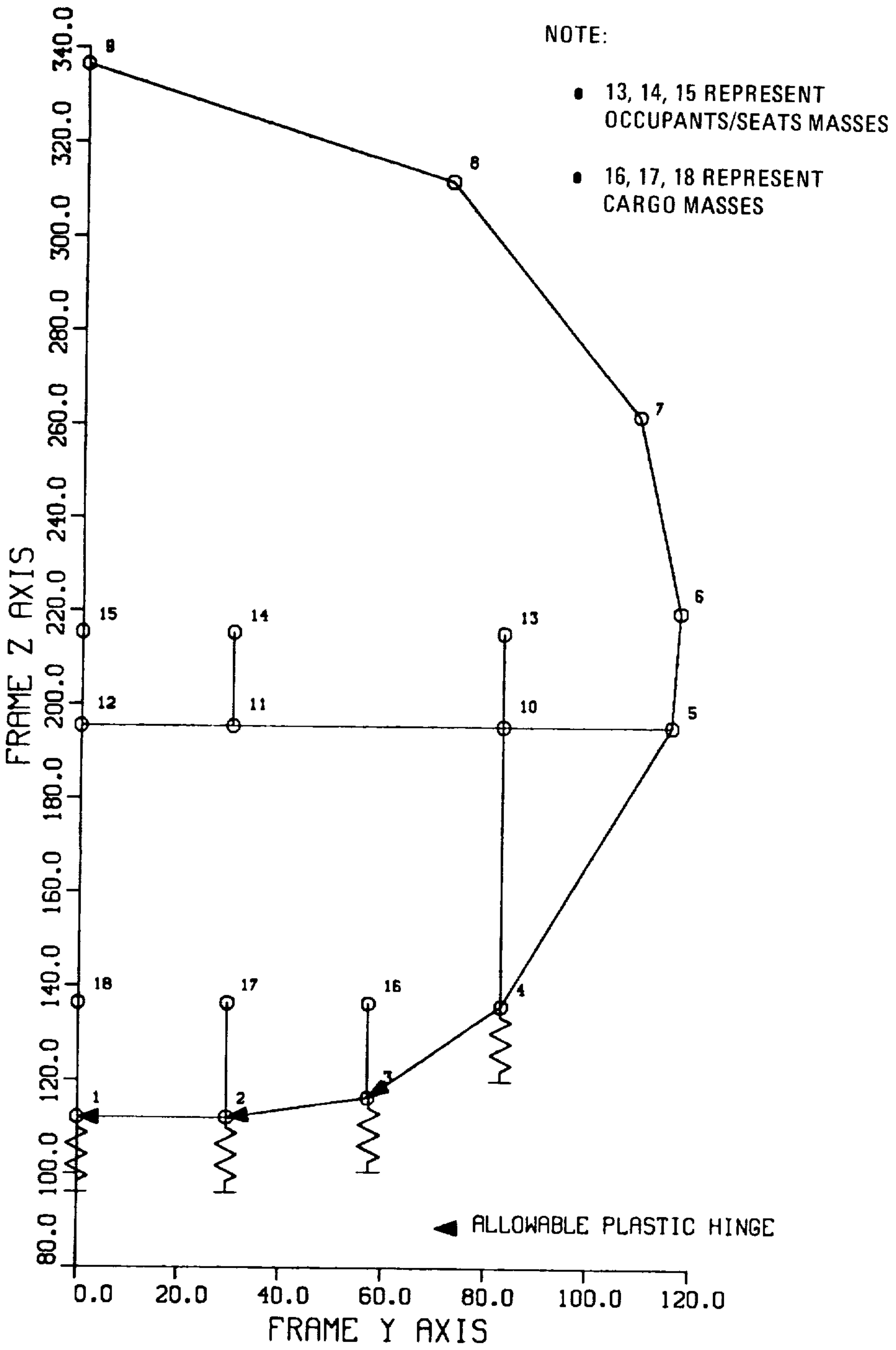

Figure 6. - Baseline airplane shear-web frame model.

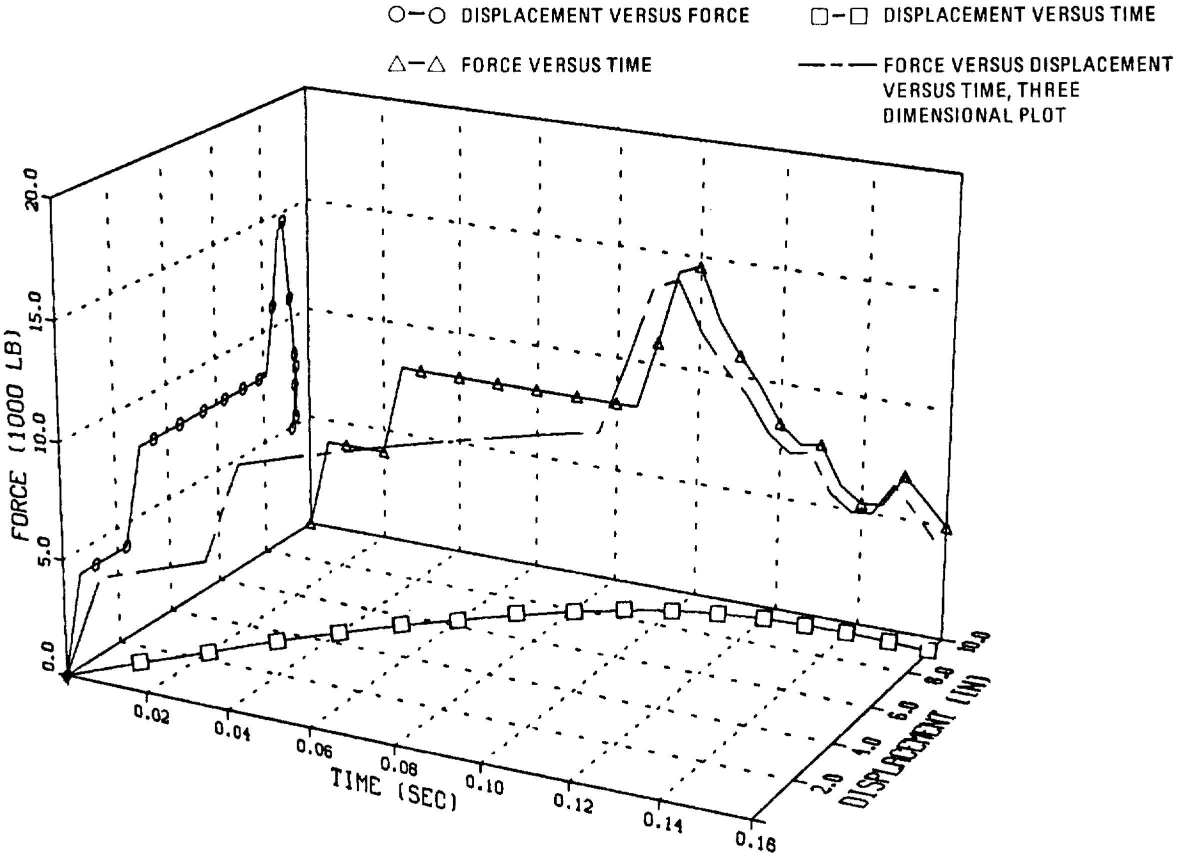

Figure 7. - Baseline airplane frame load-deflection history.

Analytically determined peak loads for the baseline fuselage section, developed during the 10 ft/sec impact for the beam elements in the lower quadrant of the fuselage above the cargo floor, are summarized in Table 3. Based on the frame section impact study, load-deflection requirements for typical composite structure below the cargo floor, were developed for candidate development test specimens (see Figure 8).

1.2.2 Development test plan.- A brief description of each element selected and its purpose is presented below.

- Frame Segment. - During an emergency landing condition, the extreme lower segment of the fuselage could be subject to impact loads. A test was designed to measure frame deformation under such a loading condition. The applied load changes in a continuous manner as the frame is crushed after impact with the ground. The loading configuration represents a normal loading condition for a lower segment of the fuselage. The metal specimen provides baseline data for current under-fuselage structure. The composite specimens provide comparative data to measure load, energy absorption, and efficiency of the respective design concepts. One composite concept was tested dynamically to determine the strain rate sensitivity.

TABLE 3. - MAXIMUM BEAM LOADS TWENTY-INCH FRAME SEGMENT (1 BAY)

BEAM	MASS i, j	PEAK LOADS (BEAM AXIS SYSTEM)				
		F_x (lb)	F_z (lb)	M_{yi} (in lb)	M_{yj} (in lb)	TIME* (sec)
3	3, 4	-3440	2500	34000	47000	.04
		-6600	2500	25000	47000	.10
4	4, 5	-5000	-1000	-48000	-24000	.10
5	4, 10	-5000	–	–	–	–
6	5, 6	-2760	1000	26000	-20000	.10

*APPROXIMATE TIME AT WHICH PEAK OCCURS

SIGN CONVENTION

FORCES F_x, F_y, F_z END i ARE EQUAL AND OPPOSITE TO FORCES AT END j.

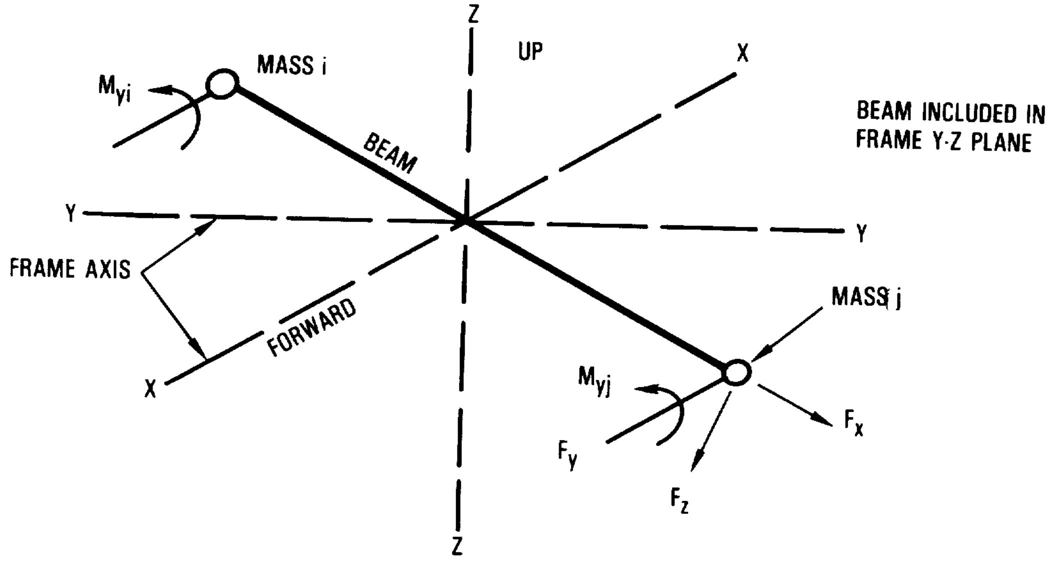

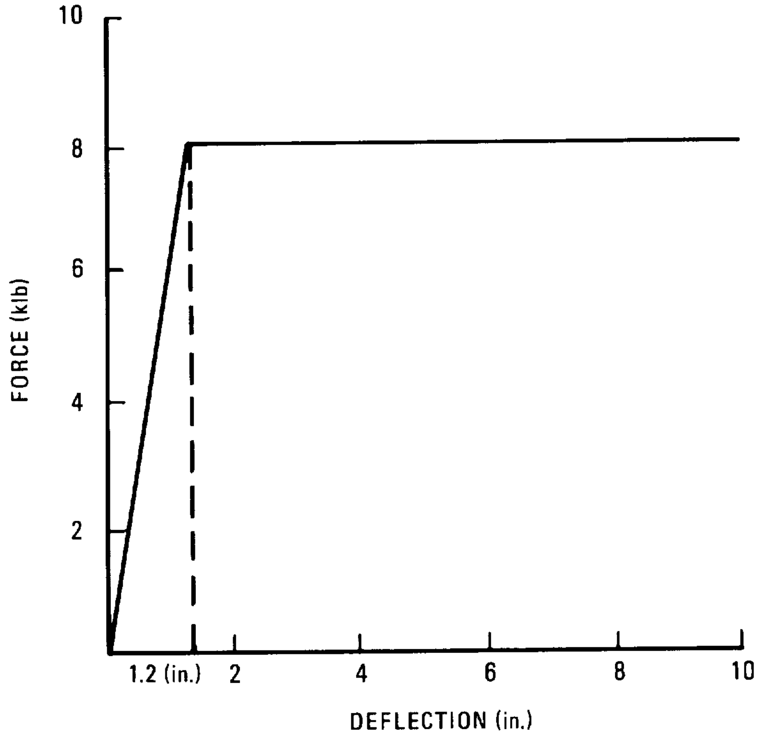

Figure 8. - Estimated load deflection requirement for cargo floor support structure.

- Stiffened Panel. - These panels, under the aforementioned crash impact conditions are subject to normal or combined normal and in-plane loads. Since the initial impact normally occurs on a concrete surface, the coefficient of friction should be relatively low (0.35); thus, a normal load should be adequate for evaluating energy absorption characteristics. The metal design provided baseline data from which the behavior of the composites could be compared. The measured data was used to compare load and energy absorption efficiency of the different design concepts under both static and dynamic loading to determine strain rate sensitivity.

A summary of the development tests is shown in Table 4.

The stiffened panel specimens are shown in Figure 9. The aluminum test panel was similar to the cargo subfloor structure of the ATX-350I baseline and the L-1011. It consisted of four T-shaped stiffeners, spaced 9.3 inches apart, mechanically fastened to the skin. This structure is critical in shear, and was analyzed for the L-1011 loads using partial diagonal tension field theory. It also carries some crushing loads. The first composite specimen was stiffened with four T-sections, spaced 9.3 inches apart and cocured with the skin. The panel was designed on a static strength basis as a

TABLE 4. - SUMMARY OF IMPACT DYNAMICS CONCEPT DEVELOPMENT TESTS

SPECIMEN TYPE	NUMBER	TEST	
		STATIC	*DYNAMIC
STIFFENED PANEL			
METAL – T STIFFENER	1	●	
COMPOSITE – T STIFFENER	1	●	
COMPOSITE – HAT STIFFENER	1	●	
COMPOSITE – CORRUGATED WEB	1	●	
FRAME SEGMENTS			
METAL – J STIFFENER	1	●	
COMPOSITE – J STIFFENER	1	●	
COMPOSITE – CORRUGATION	1	●	
MODIFIED STIFFENED PANELS			
COMPOSITE – HAT STIFFENER-CHAMFERED	2	●	●
COMPOSITE – SHORT CORRUGATION-CHAMFERED	2	●	●
COMPOSITE – CORRUGATION-CHAMFERED	1	●	
ATTACHEMENTS			
ANGLE BRACKETS	3	●	
AIRPLANE INSTALLATION CONFIGURATIONS			
COMPOSITE – HAT STIFFENERS WITH ATTACHMENT BRACKETS	2	●	●

*IMPACT VELOCITY = 10 FT/SEC TO 14 FT/SEC

structural equivalent of the baseline aluminum design with no consideration given to its energy absorption capability. The second composite specimen had three hat-shaped stiffeners, spaced approximately 13 inches apart and also cocured with the web. The corrugated specimen was the same overall size as the other panel specimens.

The frame/skin specimens were 60 inches long (circumferential direction) and 30 inches wide, each containing two frames spaced 20 inches apart. The frame cross sections are shown in Figure 10. The aluminum frame was based on the lower fuselage frame design of the ATX-350I baseline. It consisted of C-section frames attached to the skin through shear clips. The overall frame depth was 5 inches. The first composite frame/skin specimen was based on the composite baseline lower fuselage frame design. As in the baseline design, the test specimen was made of Z-sections with integral clips. Although the baseline had a 6-inch deep frame, the composite test specimen frames were made 5 inches deep to eliminate frame depth as a test variable. The 5-inch deep composite frame was designed to have the same bending stiffness as the aluminum frame. The third frame/skin specimen was a corrugated design with the same depth and bending stiffness as the others.

1.3 Acoustic Transmission Investigation

1.3.1 Acoustic transmission considerations.- The lower fuselage weight, made possible with the use of composites, was expected to result in a higher interior noise level, based on the mass law. A compensating increase in the interior trim could minimize the weight reduction achieved even to the point of eliminating composites from this particular application.

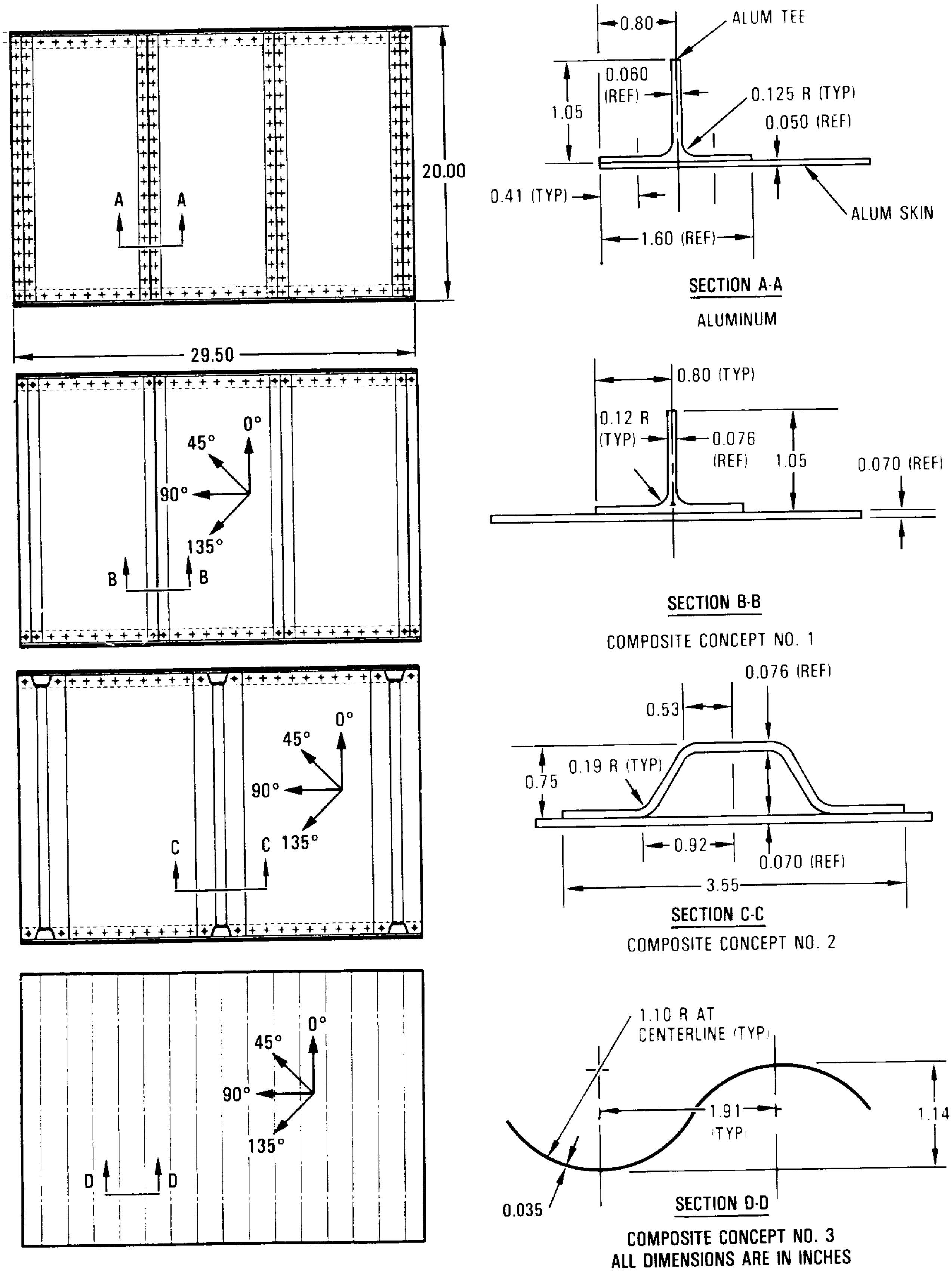

Figure 9. - Stiffened panel elements.

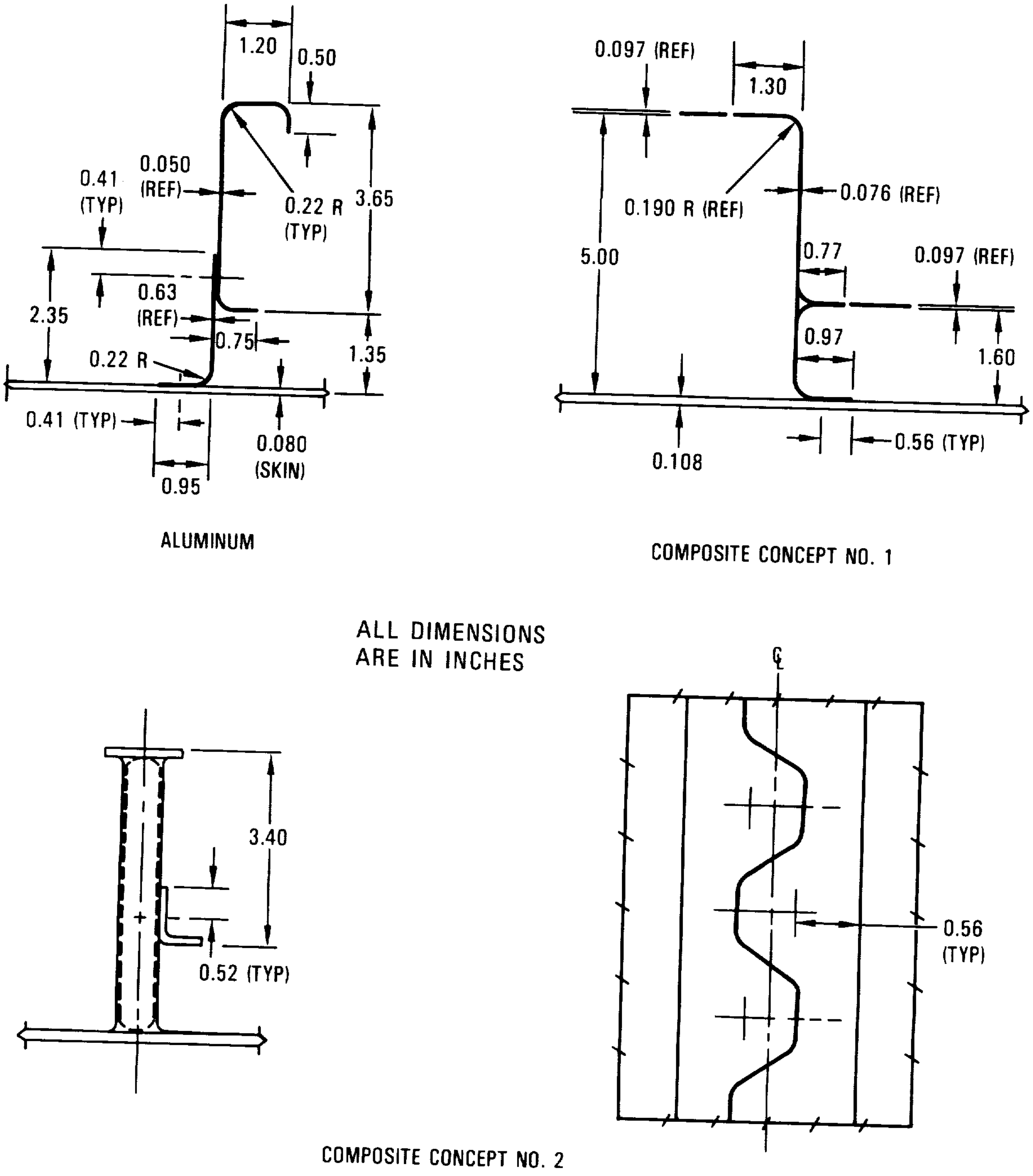

ALUMINUM

COMPOSITE CONCEPT NO. 1

ALL DIMENSIONS
ARE IN INCHES

COMPOSITE CONCEPT NO. 2

Figure 10. - Frame panel elements.

The ability to tailor the strength and stiffness characteristics of composites to the static and dynamic load paths offers potential for reducing the interior noise. However, this tailoring is complicated by the complex loads and stiffness requirements for a pressurized shell which imposed limits on the available design options.

The approach for designing the fuselage shell for optimum noise transmission involved the use of a skin layup with fibers oriented in the circumferential direction (90 degrees) and at ±45 degrees to this direction. This layup is favorable for carrying the circumferential pressurization loads. The axial loads would be carried mostly by the stringers. One or two axial (0-degree) plys may be used at the neutral axis of the skin to pick up more of the axial load.

The above fiber orientation should increase both the coincidence frequency of the panels and the noise transmission loss in the mass-controlled region. The ring frequency would be increased over that obtained with aluminum skin, although two ring frequencies could be introduced, one for the skin and another for the skin/frame combination. The concentration of uniaxial fibers in the frame caps was expected to increase the frequencies of the low-frequency frame modes. The fiber orientation in the skin was expected to do the same for the low-frequency, cylindrical shell (skin) modes.

The floating-frame concept, in which the frames are attached only to the stringers, also appeared very attractive for the upper fuselage. This design configuration, used on a number of current transport aircraft, would result in very long panels (very high aspect ratios) that were expected to reduce the acoustic radiation, especially, with the fiber orientation selected for the skin.

In the side walls, the frames need to be attached to the skin for carrying the shear loads. These attachments would reflect travelling waves in the skin, forming standing waves in the panel, which would radiate sound into the cabin. In the area below the floor the frames would be tied to the skin. This area was considered less important for noise transmission because of the added transmission loss provided by the floor.

Using the approach described above, two 5.5-foot-diameter cylinders, one aluminum and one composite, were designed. The aluminum cylinder shown in Figure 11 has bulb angle stiffeners spaced approximately eight inches apart. The skin is 0.040 inches thick all the way around. The fuselage barrel section would be made of four skin/stringer assemblies; top, bottom, right side, and left side. The frames are 2-inch deep channels spaced 15 inches apart, and would be made in two pieces spliced at the top and bottom of the fuselage. A channel-shaped floor beam and a pair of I-section floor posts are also included at each frame location. All pieces would be mechanically fastened.

The aluminum cylinder was representative of the structure of the Metroliner fuselage. The Metroliner was selected because test data was

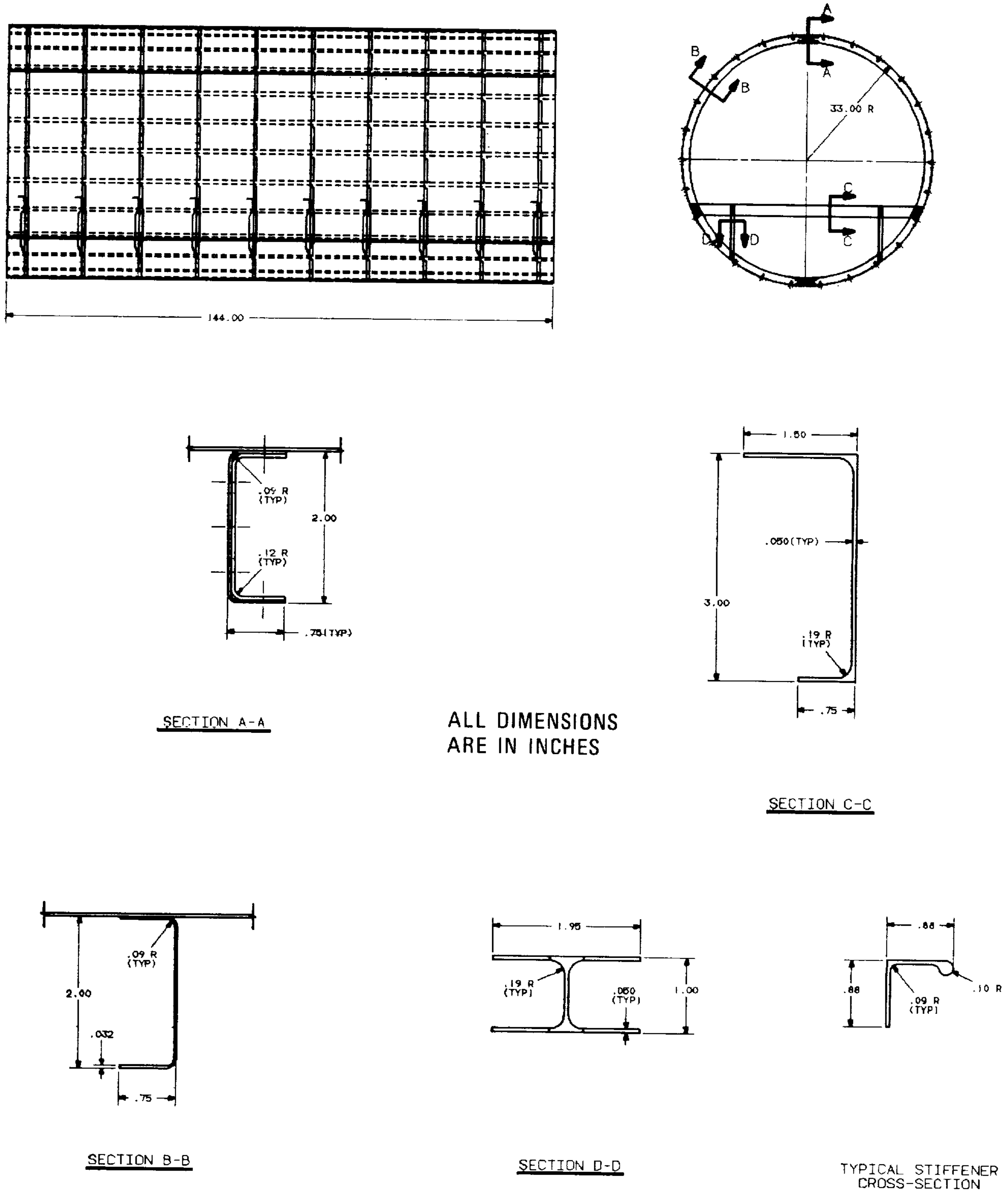

Figure 11. - Baseline aluminum acoustic cylinder design.

available which could be used to validate the new analysis program. Thus, the criteria for the design of these cylinders were derived from the Metroliner design criteria. Because these shells were to be used to compare the acoustic transmission of composite structure with that of aluminum structure, the most important aspect of the design was that both cylinders have similar stiffnesses; the exact values of those stiffnesses being of secondary importance. The design criteria selected are shown in Table 5.

The composite cylinder design, shown in Figure 12, differs from the aluminum design most notably in the skin and stringers. Z-stiffeners would be used instead of bulb angles and the stiffeners would be bonded, not riveted, to the skin. The skin would be wound in one piece, thus eliminating the need for skin splices. The stringer and frame spacings were not changed in the composite design; neither were the basic sizes and shapes of the frames, floor beams, and floor posts.

A weight comparison for the two designs is shown in Table 6. These weight savings differ in detail from those for the widebody ATX-350I because the physical size differences cause different failure modes to occur.

The composite cylinder design was later revised to facilitate fabrication by filament winding for the demonstration article. The material selected to make the cylinder was Fiberite T500/934-6K towpreg with a ply sequence of $(\pm 45/\pm 32/90/\mp 32/\mp 45)$.

The design concept for the basic structure is shown in Figure 13. A J-section frame, Figure 14, was selected to provide a peel-resistant attachment to the skin. The frame spacing was kept at 15 inches to maintain correspondence with the metal counterpart structure.

The hat-section stringer, Figure 15, was selected because it offered good resistance to damage, and tooling was already available. It was found that the requirements could be met with 22 stringers, as compared with 26 for a J or blade-stiffened design.

The frame and stringers were tied together with a clip and all elements of the fuselage structure were rivet-bonded together. A paste adhesive, Dexter EA-9304.2, was used and bonding pressure was applied by means of NAS1921 and NAS1919 monel fasteners, which remained in place.

The addition of the floor and floor support structure, shown in Figure 16, completed the demonstration test article. The floor consisted of 0.5-inch plywood; supporting beams and posts were made from aluminum extrusions. The floor and floor supports were included in the demonstration article because their connections to the shell provided constraints that affect the acoustic vibration modes of the shell. The materials used for the floor and its supports do not affect those vibration modes, so relatively inexpensive materials were selected. Similiarly an aluminum clip (Figure 17)

TABLE 5. - DESIGN CRITERIA FOR NOISE ATTENUATION DEMONSTRATION TEST SPECIMENS

Bending Moment	1095000 in. lb
Shear Load Capability	10150 lb
Et	565000 lb/in.
Gt	160000 lb/in.
Internal Pressure	7 lb/sq in.

Note: $Et = (Et)_{skin} + \frac{(EA)_{Stiff}}{b}$ where b is stiffener spacing

CRITERIA

- Non-buckling to at Least 50% of design limit load.
- Maintain 15 inch frame spacing.

TABLE 6. - ACOUSTIC CYLINDER WEIGHTS

	BASELINE ALUMINUM (LB)	COMPOSITE (LB)
Skin	121.6	101.1
Stringers	35.0	27.0
Frames	21.8	15.2
Splice	1.5	0.9
Passenger Floor Beams	16.4	12.0
Floor Posts	6.3	2.5
Fasteners	4.1	7.3
Padups	0.0	1.3
Total	206.7	167.3
Overall Savings (%)	--	19.1

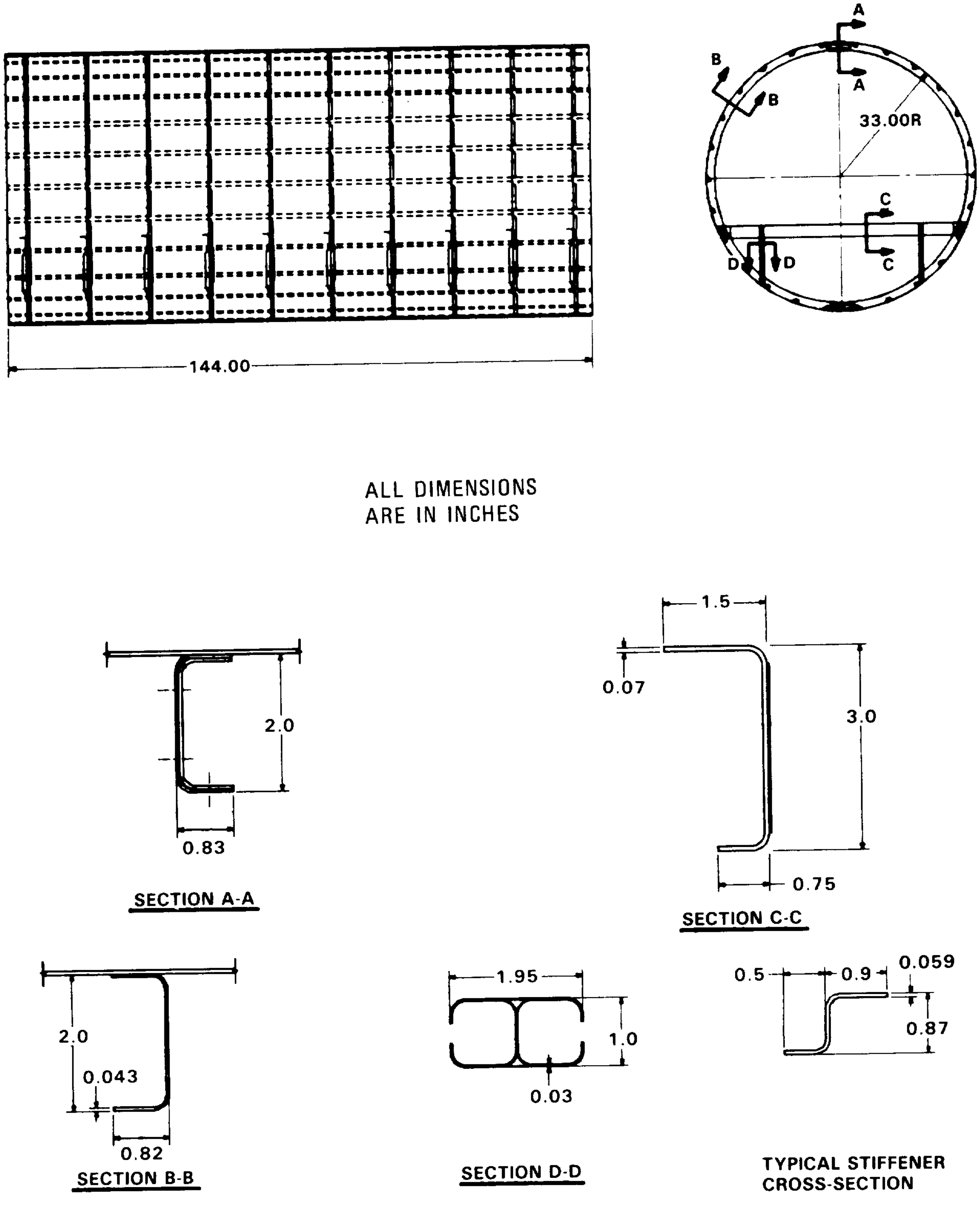

SECTION A-A

SECTION C-C

SECTION B-B

SECTION D-D

TYPICAL STIFFENER CROSS-SECTION

Figure 12. - Baseline composite acoustic cylinder design.

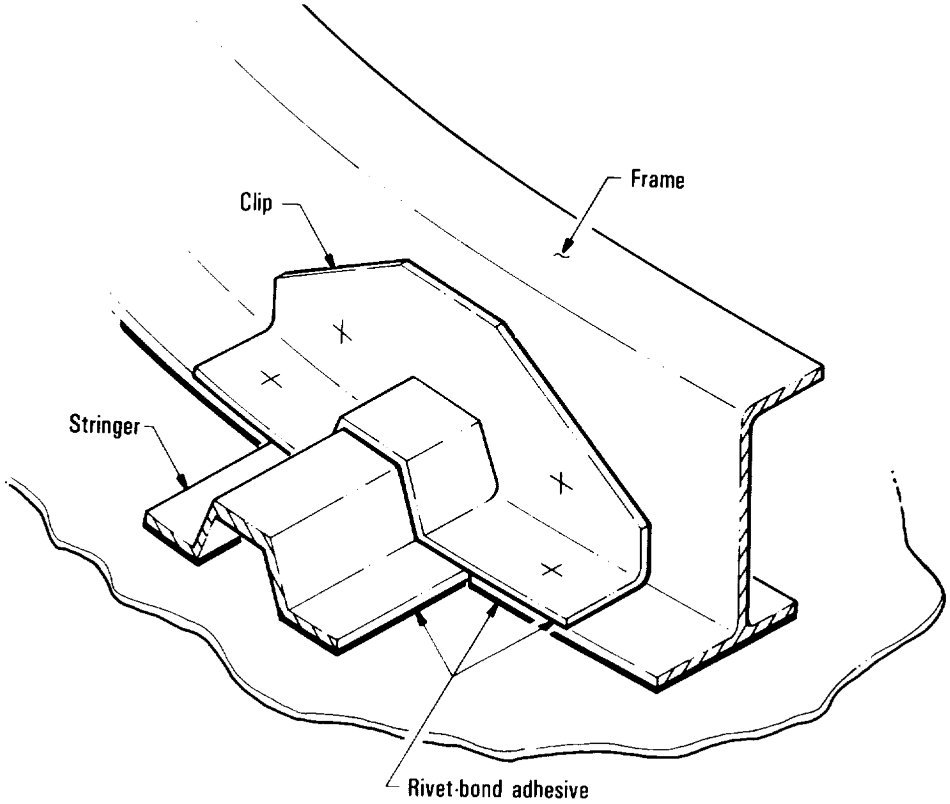

Figure 13. - Structural configuration acoustic test cylinder.

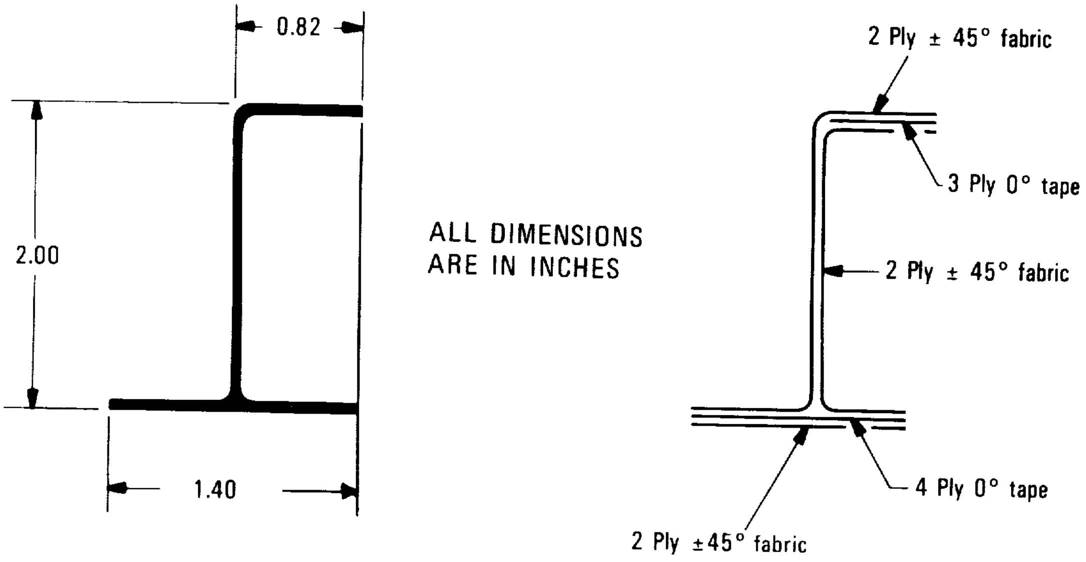

Figure 14. - Frame configuration.

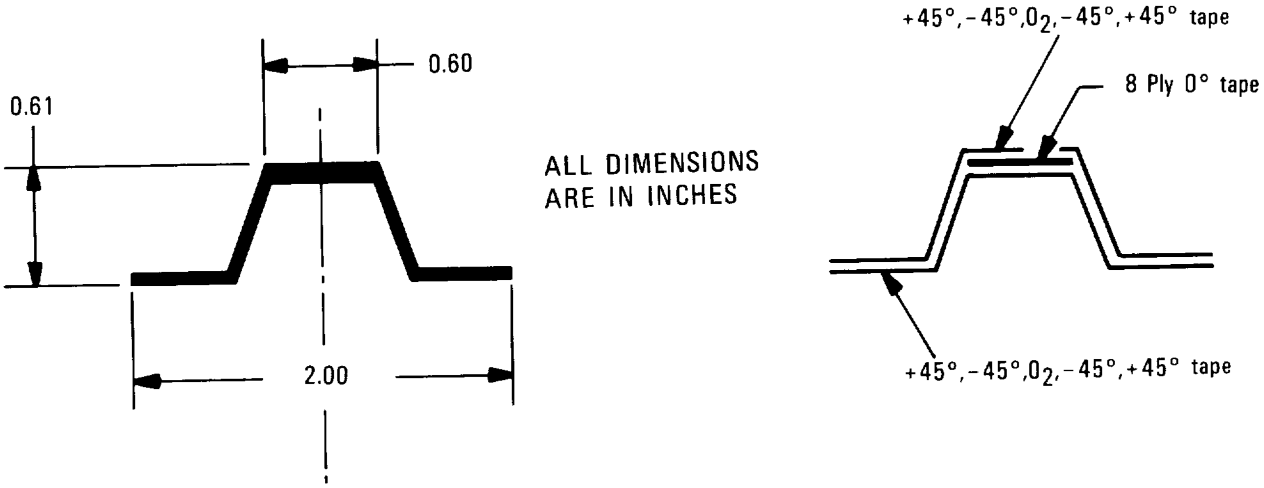

Figure 15. - Stringer configuration.

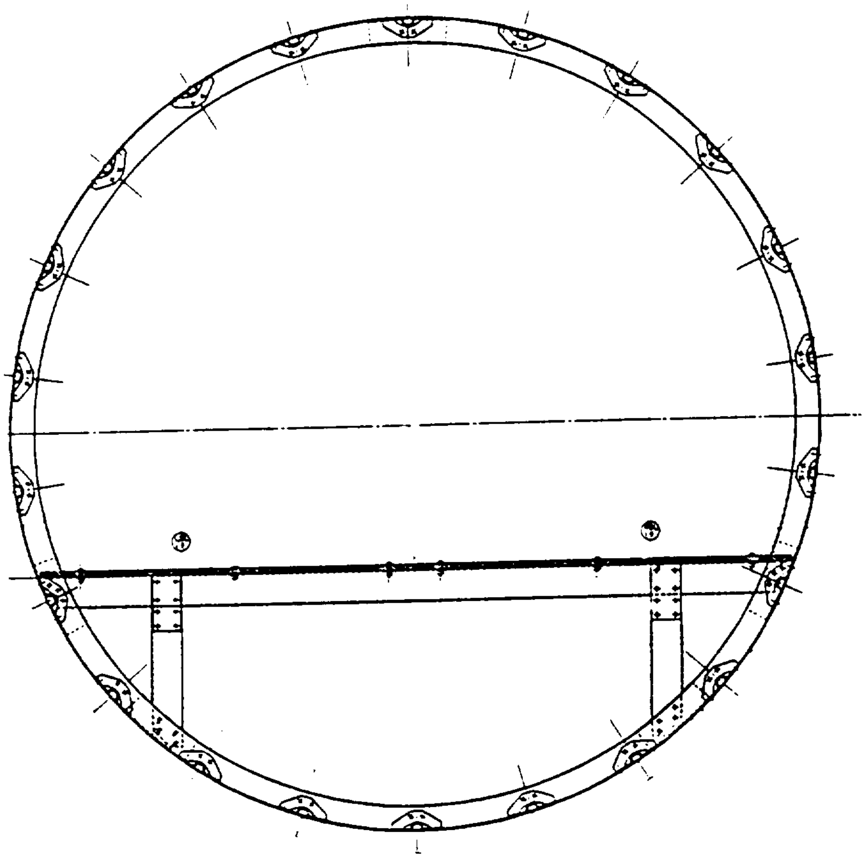

Figure 16. - Section showing floor support structure.

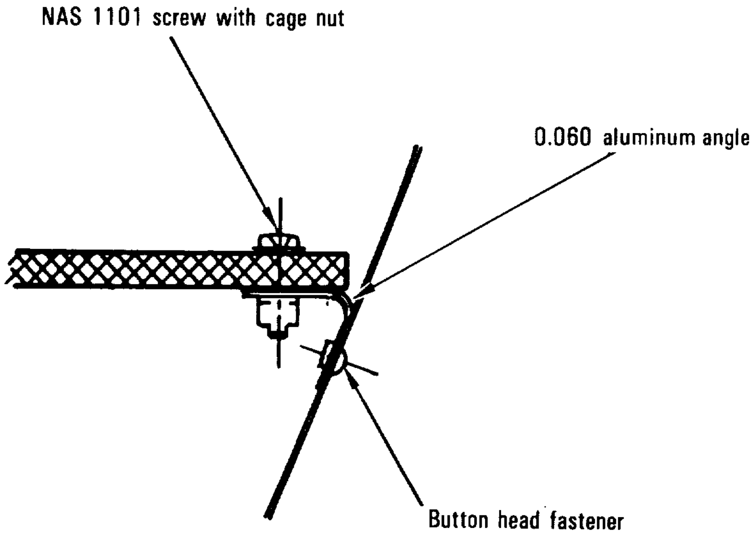

Figure 17. - Floor-to-shell connection.

was chosen to form the tie between the floor and the shell because it was the least expensive way to simulate the restraint provided by that floor-to-shell connection. The resulting fuselage assembly (with the floor removed for clarity) is shown in Figure 18.

2. ANALYSIS DEVELOPMENT

2.1 Impact Dynamics Analysis Development

A literature survey was performed to assess the applicability of advanced composite design and behavior data to transport aircraft. The findings were:

- Advanced composite materials in compressive loading generally exhibited substantially less energy absorption capability than aluminum alloys. However, hybrid designs which utilize different composite material combinations are able to increase the energy absorption capability. In addition, energy absorption of advanced composite materials is affected by the changes in ply orientation.

- Test data were almost nonexistent for large composite structures.

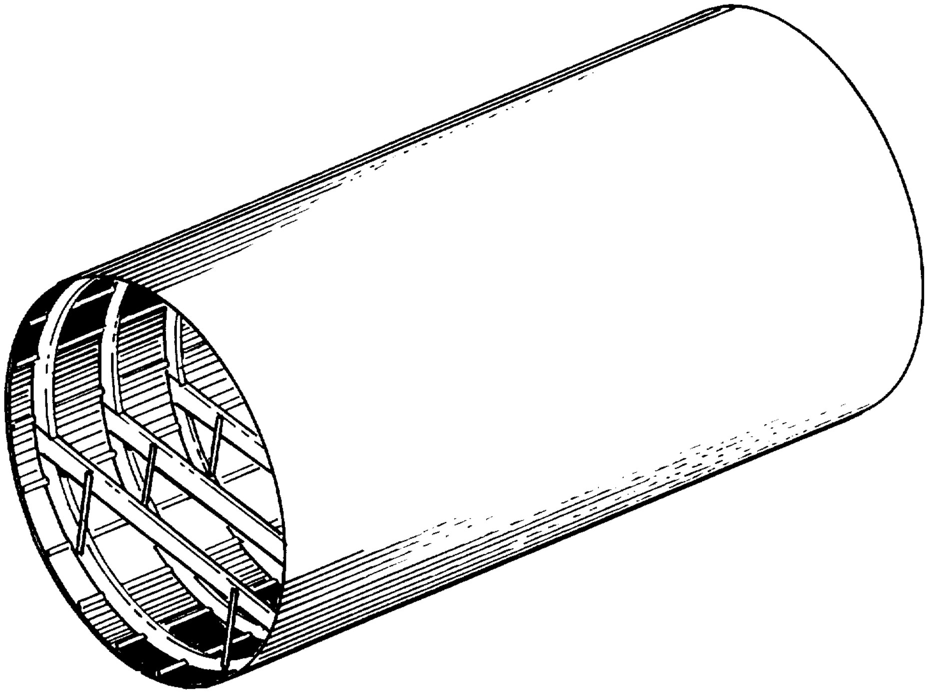

Figure 18. - View of cylinder showing floor support structure.

- Helicopter and general aviation aircraft subfloors are generally 6 to 12 inches in depth. They are well suited for the use of relatively short columns, tubes and beams insofar as crush requirements are involved. However, transport airplane fuselages are much wider and the depth from passenger floor to ground contact point is substantial. Thus, the design for energy absorption presents significantly different considerations. Data developed for transport airplanes must be obtained from designs that are more compatible with the space and size associated with fuselages. It may be necessary to consider the cargo subfloor as a region for added energy absorption and provide compatible strength in the passenger floor and supporting structure.

As discussed in Section 1.2.1, the lower region of the fuselage underside was selected as the focal point for the initial design effort. Thus, the methodology development was supportive of designs that were being used or could be applicable to this region. Element types considered were stiffened panels and unstiffened frame segments. Methods are based on work in Reference 6.

Program LD/CURVE was developed to predict the load deflection characteristics of the structural configurations under consideration in this study. It is an interactive program written in FORTRAN language and runs on the Digital Equipment Corp. VAX 11/780 computer and VT-100 terminal.

Two input data modes are built into the program. Data may be input interactively or through an input data file. When in the interactive mode, the program prompts the user for required data as it is needed. When in the data file mode, the input data is read from a data file which must be defined before the program is run. In both modes, the user is always queried after the data are read and before they are used. At this time the user may make any corrections or modifications necessary.

In general, the data required by the program are mechanical properties describing the material from which the specimen is fabricated and geometric properties which describe the specimen configuration. For specimens fabricated from aluminum, semi-empirical data may also be requested. For these cases tabulated data and design charts are supplied.

The program methodology and use is discussed in detail in Appendix A.

2.2 Acoustic Transmission Analysis Development

A major objective of the program was to determine if significant increases in interior (cabin) noise levels occur when composite materials are substituted for aluminum. For designs that are similar; i.e., those having conventional frame and stringer construction but designed on an equivalent strength basis, composite materials will yield the lighter structure. Also, it was thought that a composite fuselage would be inherently more lightly damped. Both factors lead to a conclusion that interior noise from all types of excitations (turbulence, jet noise, or propeller tones) would be increased.

Turbulent boundary layer induced interior noise is of major concern, over the frequency range between 200 and 1,000 Hz, in turbofan aircraft. Initial plans were to determine the severity of TBL induced interior noise in such aircraft through integrated experimental and theoretical studies. Experiments were to include a simulation of TBL pressure fluctuations using a ducted excitation over a composite cylinder stiffened by composite frames and stringers, with an integral stiffened floor. However, NASA has postponed the acoustic experimental work because of a reduction in funds. Predictions of TBL induced interior noise in a composite fuselage cabin must thus rely on analytical methods and software developed under the program. These methods are presented in Appendix B. The following work was completed.

- Development of the theoretical methods required for predicted boundary layer noise transmission for a stiffened composite fuselage cabin with trim.

- Development of "smeared stiffener" and "discrete stiffener" theoretical models of a stiffened composite fuselage with floor.

- Computer coding of an advanced version of the PAIN program (Reference 7) designated PAINML to compute interior noise arising from TBL excitation using a composite structures program to feed modal data to the revised program.

- Computer coding of the "smeared stiffener" composite structures program MRPCOMP.

All of the components to predict and compare TBL induced interior noise for composite and aluminum aircraft were created.

2.2.1 TBL induced interior noise: Comparison of predictions with measurements for a conventional aluminum fuselage.- Computer software developed under this program is complex and extensive. The plan was to validate the software using comparisons of predictions with measurement results from ducted progressive wave tests. In the absence of test data, program debugging, evaluation and validation would be more difficult, since there would be no standard of comparison. The decision was made to validate, in a less than rigorous fashion, by comparing predictions against measurements made of boundary layer induced interior noise occurring in a small business aircraft (an early generation fan jet). The objective which was achieved was to first assure that a high quality prediction could be made for that aircraft. This procedure validates the computer coding and also the analytical model, so that when replacement of the conventional aluminum structure is made with an equivalent composite structure, a valid comparison of the two types of fuselages is obtained.

Figure 19 shows the configuration of the aircraft used in the study. Predictions were made for the space-average sound levels in one-third octave bands that occur in the cabin (cockpit excluded). The fuselage was modeled as a stiffened cylinder with integral floor over the full circular length of the fuselage barrel. The boundary layer was assumed to grow with distance from the nose of the aircraft. TBL excitation levels were estimated using Lowson's results (Reference 8).

Figure 20 shows interior noise levels measured in the aircraft for two forward speeds. These measurements were in the aft end of the cabin. The effect of aircraft speed on boundary layer induced interior noise can be seen to be dramatic. Both curves have imposed on the interior noise from the flow, the fan and turbine tones. The tones can be disregarded in this work. Boundary layer induced noise is typical of other locations in the cabin.

Interest here is confined to the upper curve, since the cruise speed (260 KIAS) and altitude (17,500 ft.) are defined. The true airspeed is 342 knots ($M = 0.53$). Although this is less than optimum (a Mach number of 0.7 - 0.8 would be preferred), it is sufficiently high to be useful. The boundary layer thickness is quite thin however, compared to that expected on a transport aircraft.

The aircraft has certain features that were useful to this study. Its diameter and contruction are similar to that of the composite test article (almost exactly the same diameter) and this allowed for only slight adjustments in predicted properties of the composite test article to achieve an equivalent composite fuselage for the aircraft.

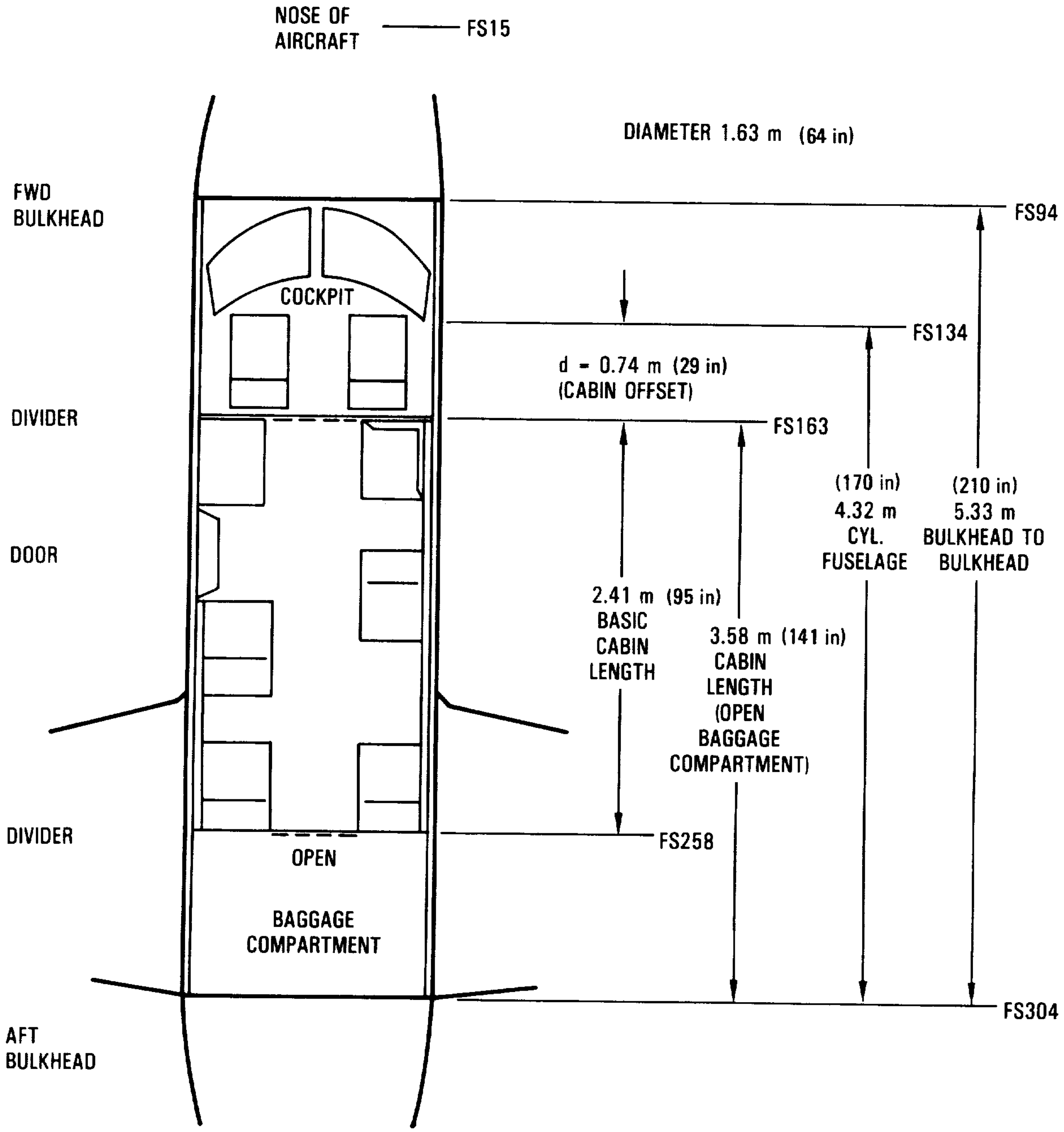

Figure 19. - Aircraft configuration.

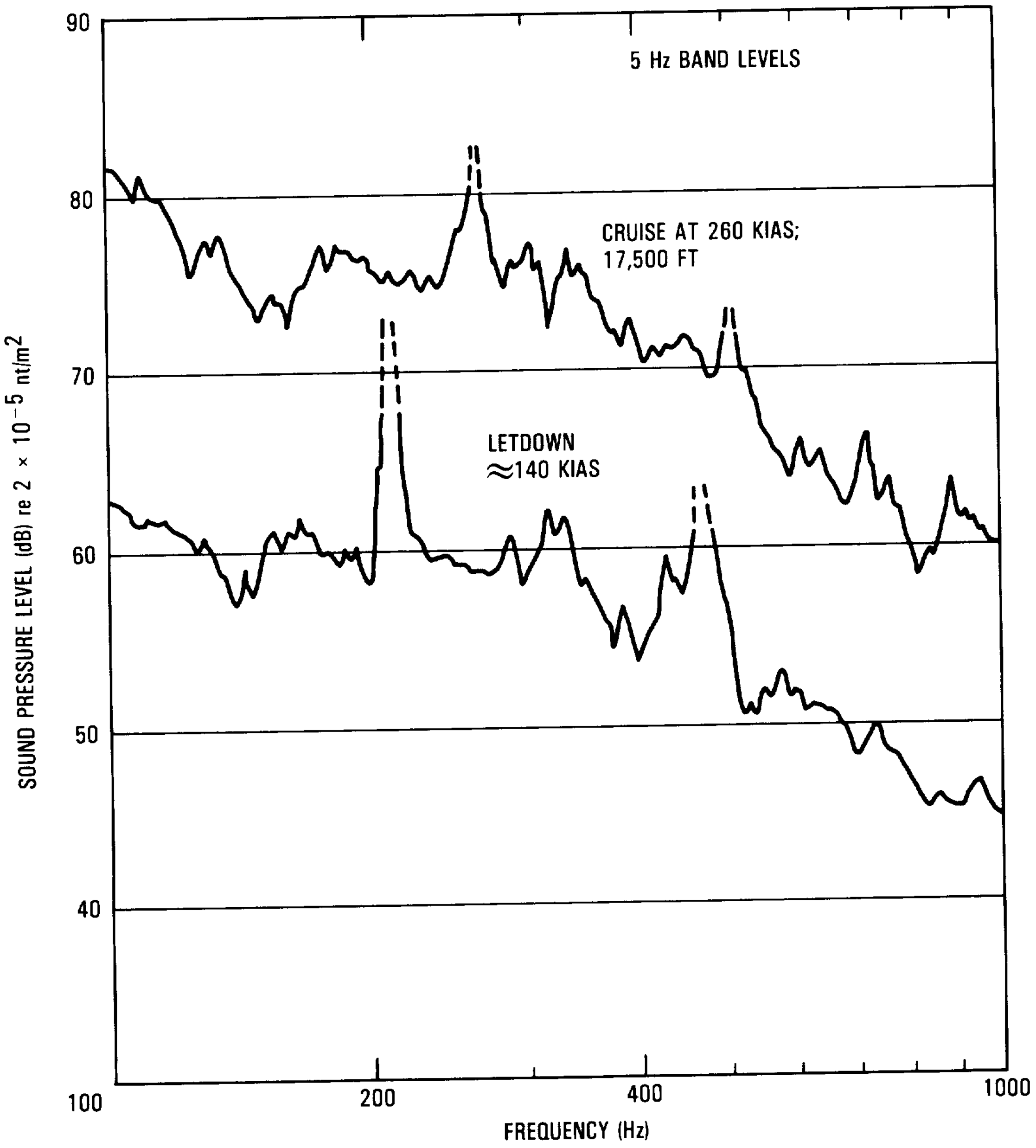

Figure 20. - Interior measurements.

Table 7 gives the properties of the fuselage and trim that were used to create the input data files for the structures program MRPCOMP and the master program PAINML for the aluminum aircraft. The cabin trim consists of four layers: two layers of fiberglass insulation separated by a lead impregnated vinyl septum, finished with a glass covered Nomex (Hexcell) lining. Sea level cabin pressure is maintained.

Figure 21 shows results of comparisons with predictions. The upper curve gives the predicted levels, in one-third octaves, of the pressure fluctuations on the skin of the cabin due to the turbulent boundary layer. The curve labeled "measured TBL induced interior levels" is the same curve as the upper curve of Figure 20, with the 5 Hz band levels having been converted to one-third octave band levels. The tones present in Figure 20 measurements have not been included. The predicted interior levels indicate an incomplete calculation below 160 Hz. This is the result of the type of modal data generated for the fuselage and used in PAINML to make the calculation. The program was written to include only structural modes resonant within or below the band (for computational speed). At 160 Hz and above, the calculation agrees with test data and the modal file is complete to the 800 Hz band. Beyond that a new set of data would be needed and additional calculations performed.

The comparison in Figure 21 is felt to be sufficiently good to validate the prediction. However, no attempt was made to use a hypothesis test on the data to determine the level of bias error, if any, because there was some question as to whether the damping levels assumed for the trim and structure were correct and only approximations of structural properties were attempted, (precise details of frames and stringers were not available). Interest here was only in confirming that the PAINML coding worked properly, and it is accepted as such.

2.2.2 Performance of a composite fuselage.- Figure 22 gives the results of primary interest. In this figure the aluminum shell (skin, frames and stringers) are compared with an equivalent strength design composite (skin, frames and stringers). The stiffened floors were taken as identical, with identical cabin trims. However, the level of damping of the shell of the composite is one order of magnitude lower than that of the aluminum structure at all frequencies. For instance, the structural loss factor of a mode resonant at frequence f_r was taken as $2/f_r$ for the aluminum structure and $0.2/f_r$ for the composite. Table 8 gives the properties of the equivalent strength composite fuselage.

Figure 22 shows that the composite fuselage will actually be slightly better acoustically than the aluminum fuselage, in spite of its lower damping level. This result occurs because the trimmed fuselages are equivalently "damped." This effect is explained later and it is clearly a significant effect. It can be shown that if the damping levels were taken as identical for modes of either fuselage, insignificant changes in the above predictions result. Examination of the calculations leads to the conclusion that even though a composite fuselage may begin as a more "live" structure, trim

TABLE 7. - AIRCRAFT FUSELAGE AND TRIM CHARACTERISTICS*

Fuselage diameter, D	1.626 m
Fuselage cylinder length, L	4.32 m ($L/D=2.658$)
Cabin length, L_c	3.58 m ($L_c/D=2.202$)
Cabin width	1.50 m
Cabin height	1.32 m
Floor angle, θ_o	44°
Skin thickness, range, t_s	0.81 mm - 102 mm
Frame spacing, l_f	0.332 m (avg)
Cross sectional area of rings, A_R	9.03×10^{-5} m^2
Stringer spacing, l_s	0.213 m
Cross sectional area of stringers, A_s	7.09×10^{-5} m^2
Equivalent shell thickness, $t_e=t_s+A_R/l_f+A_s/l_s$	1.63 mm
Average surface density, $m= t_e$	4.51 kg/m^2
Frame moment of inertia, I_f	9.2×10^{-8} m^4
Frame bending rigidity, $D_{R\theta}=EI_f/l_f$	2.0×10^4 N.m.
Stringer moment of inertia, I_s	7.4×10^{-9} m^4
Stringer bending rigidity, $D_{xs}=EI_s/l_s$	2.5×10^3 N.m.
Equivalent floor thickness, t_ep	1.51 mm
Floor surface density	4.86 kg/m^2
(including seating)	16.59 kg/m^2
Floor beam spacing, l_y	0.332 m
Cross sectional area, A_y	$1.1 \times 10^{-4} m^2$
Bending rigidity, D_{yp}	8.6×10^4 N.m.
Longitudinal floor beam spacing, l_x	0.376 m
Cross sectional area, A_x	$1.4 \times 10^{-4} m^2$
Bending rigidity, D_{xp}	1.8×10^5 N.m.

Trim surface area = $12.5 m^2$

Layer 1 (against skin): 0.0254 m PF105 Fiberglass insulation

Layer 2 lead vinyl septum: 0.61 kg/m^2, loss factor = 2

Layer 3 0.0508 m PF105 Fiberglass insulation

Layer 4 Nomex (Hexcell) lining with glass facing: 1.1 kg/m^2, loss factor = 0.05

*Note: Program is set up for input and output in SI units

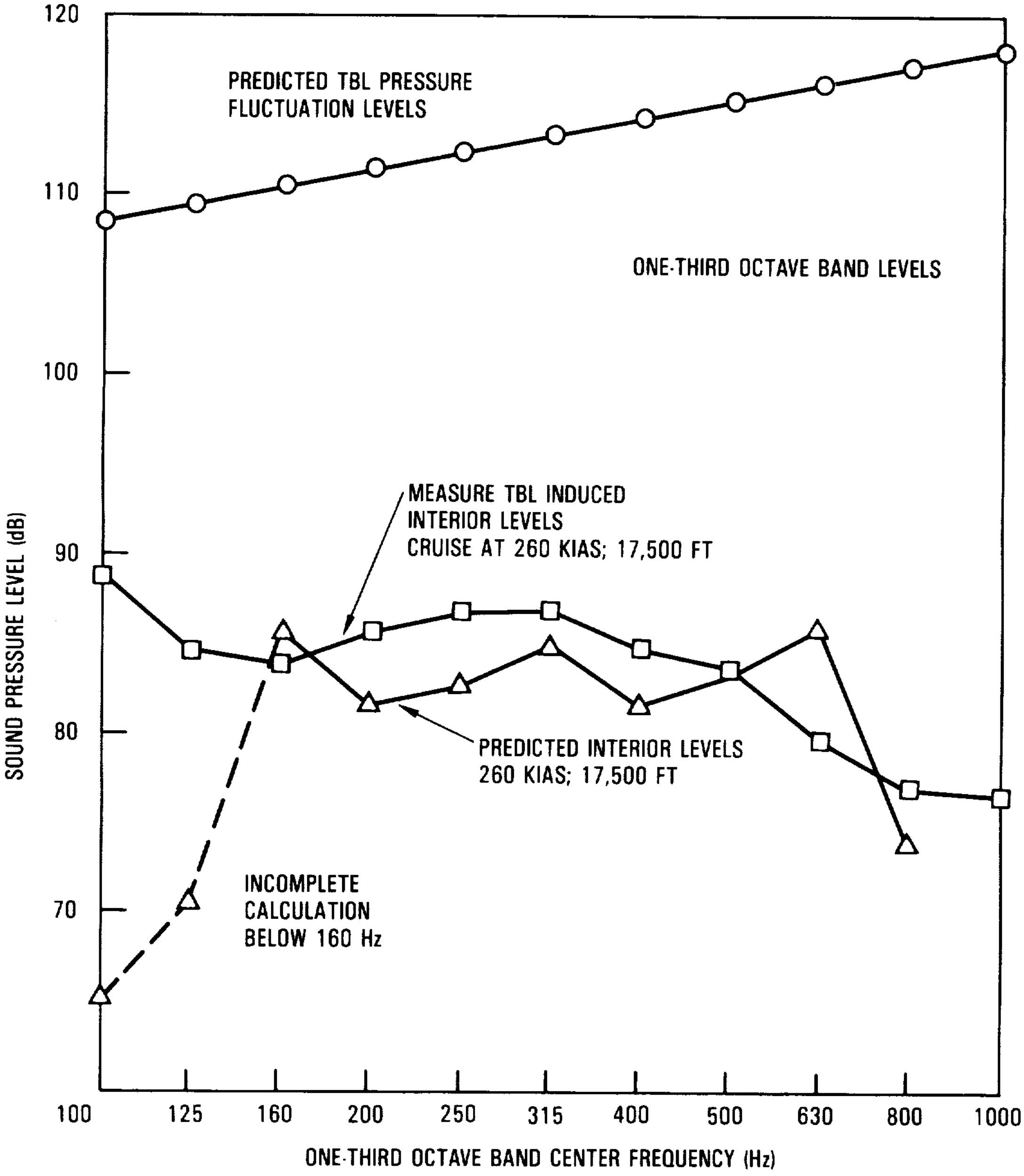

Figure 21. - Comparison of predicted interior noise with measured interior noise (aluminum fuselage).

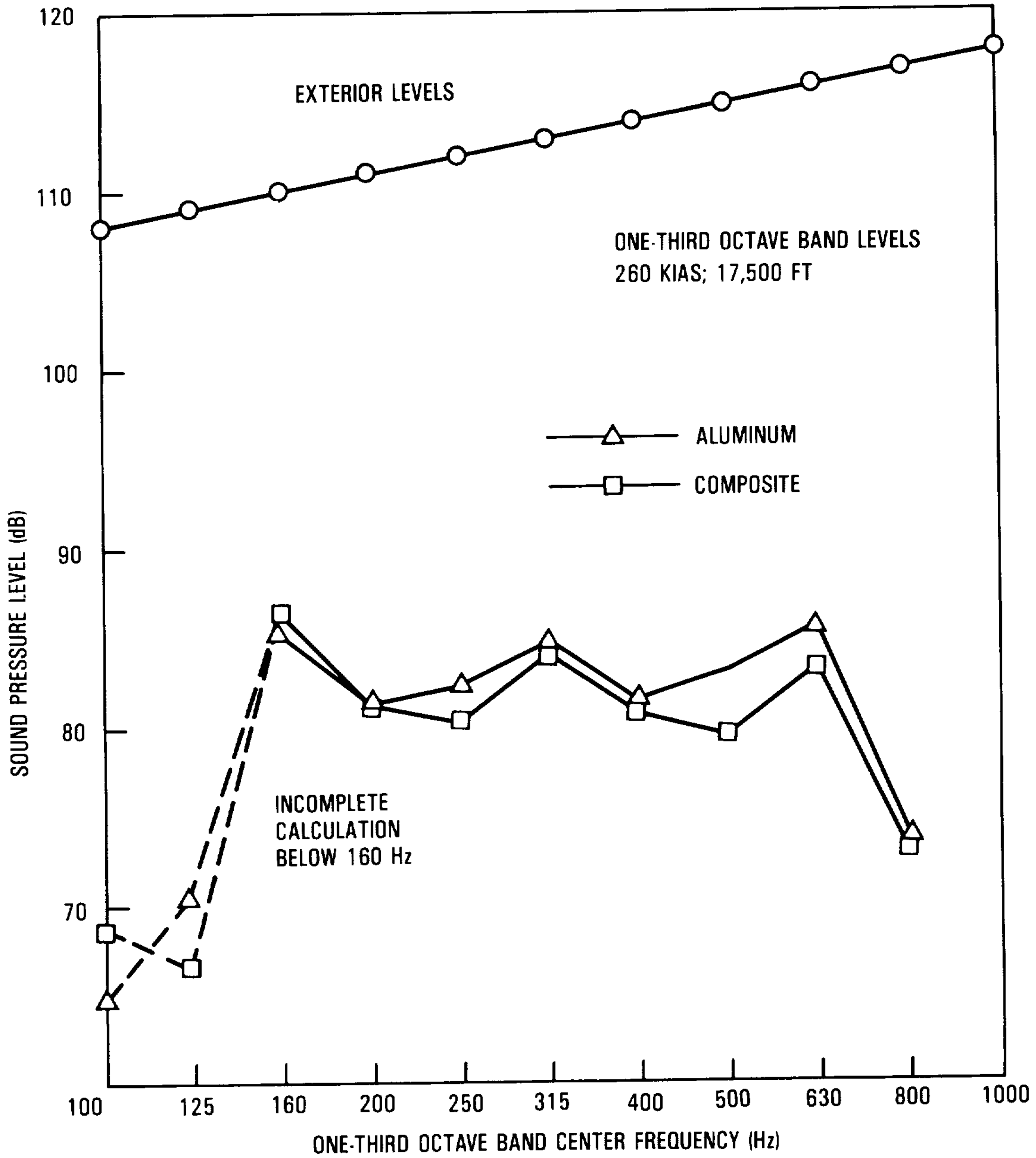

Figure 22. - Predicted interior noise levels composite and aluminum fuselages (equivalent strength designs).

TABLE 8. - COMPOSITE FUSELAGE SHELL
(APPROXIMATE EQUIVALENT STRENGTH WITH IDENTICAL FLOOR)*

Composite Skin:	
In-plane stiffnesses	Bending stiffnesses
$A_{11} = 8.754 \times 10^7$ N.m.	$D_{11} = 16.9$ N.m.
$A_{12} = 3.706 \times 10^7$ N.m.	$D_{12} = 7.93$ N.m.
$A_{22} = 7.054 \times 10^7$ N.m.	$D_{22} = 11.2$ N.m.
$A_{66} = 4.089 \times 10^7$ N.m.	$D_{66} = 8.65$ N.m.
Stiffeners: Equivalent Extensional and Bending Properties	
Composite Frames:	$\frac{EA}{l_f} = 2.37 \times 10^7$ N.m.
	$\frac{EI}{l_f} = 1.98 \times 10^4$ N.m.
Composite Stringers:	$\frac{EA}{l_s} = 3.67 \times 10^7$ N.m.
	$\frac{EI}{l_s} = 8.32 \times 10^3$ N.m.
Sidewall mass/area = 3.70 kg/m^2	

*Note: Program is set up for input and output in SI units.

installation will embed that "liveness" in more significant dynamical effects (for TBL noise transmission). There may actually be a slight reduction in interior noise levels, largely due to a reduction in the modal density of the structure caused by its higher strength to weight ratio.

2.2.3 Analysis of the baseline cylinders.- The aluminum and composite baseline cylinders shown in Figures 11 and 12 were analyzed for a laboratory test environment which was designed to partially simulate an inflight excitation. It was proposed that this simulation could be accomplished by bathing the exterior of the cylinder with carbon dioxide.

Carbon dioxide is heavier than air and its speed of sound is slower than that for air. An acoustic pressure wave traveling through carbon dioxide will propagate at approximately 80 percent of the speed of sound in air. This arrangement would provide a mismatch between the interior and exterior environment and affect the efficiency with which sound is transmitted through the structure. A significant difference between the laboratory and flight environments is the difference in correlation length between turbulent hydrodynamic pressures and acoustic pressures. Correlation length is a measure of how quickly a given pressure disturbance decays as it propagates along a surface. Inflight turbulent pressures decay very quickly and are replaced by similar but uncorrelated pressure fluctuations. On the other hand, acoustic pressure fields have long correlation lengths and show very little decay as they propagate along a surface. In an attempt to reduce the circumferential correlation for the proposed laboratory test, circumferential baffles and multiple acoustic sources were planned. In the axial direction the laboratory acoustic excitation would travel at the speed of sound and would have the long correlation lengths associated with acoustic pressure fields.

The acoustic analysis has the capability to predict noise reductions for several external pressure fields as shown in Figure 19. The initial application for the prediction methodology was to predict the acoustic transmission properties of the baseline cylinders subjected to a laboratory simulated boundary layer excitation described above. The baseline cylinders were designed to the same strength and stiffness requirements with the result that the composite cylinder has a higher strength to weight ratio. A comparison of the predicted structural and acoustic modes is given in Table 9. The cavity modes are identical since they are determined by the interior geometry of cylinder and floor. The program can handle as many as 400 structural and 400 cavity modes. It is important to know how many modes occur in each frequency band of interest. Predictions of the noise reductions for the baseline cylinders subjected to the simulated boundary layer excitation are shown in Table 10 and Figure 23 for a 1.25 kg/m^2 trim panel. The results are surprising since the composite cylinder is lighter in weight but provided a higher noise reduction in the 315 Hz to 800 Hz frequency bands. In Table 10 it can be seen that the composite structure has far fewer structural modes in these frequency bands. It is reasonable to expect that there would be less interior noise if there are fewer structural modes to transmit the energy inthe exterior excitation field. It should be noted that these results apply to small diameter cylinders with an aspect ratio of approximately 2.2. Variation of the trim panel surface density from 0.01 to 3.25 kg/m^2 produced the results shown in Figures 24 and 25 for the aluminum and composite cylinders. Comparisons between the predicted noise reductions for both cylinders show the same trend for all trim panel surface densities. It is premature to extend these results to a full scale aircraft in flight but the results are nonetheless encouraging.

The effect of bathing the exterior of the cylinder with carbon dioxide instead of air is shown in Figure 26. This comparison shows very little difference between using carbon dioxide instead of air for the exterior excitation field. If these results can be substantiated by a more thorough analysis, then the laboratory test could be conducted with air and thus simplify validation.

TABLE 9. - STRUCTURAL AND CAVITY MODES FOR BASELINE CYLINDERS

Progressive wave over test specimen, N=8 ducts around periphery
Cabin length = Fuselage length = 3.6575 meters

Modal information

Frequency (Hz)	Composite Structure		Aluminum Structure		Cavity	
	No. of Modes in Band	First Mode in Band	No. of Modes in Band	First Mode in Band	No. of Modes in Band	First Mode in Band
	0		0		1	
50.0	0	0	0	0	1	2
63.0	0	0	0	0	0	0
80.0	0	0	1	1	0	0
100.0	1	1	4	2	1	3
125.0	4	2	6	6	3	4
160.0	4	6	4	12	3	7
200.0	4	10	8	16	7	10
250.0	7	14	9	24	10	17
315.0	10	21	15	33	23	27
400.0	12	31	27	48	41	50
500.0	22	43	29	75	77	91
630.0	31	65	50	104	93	168
800.0	51	96	78	154	92	261
1000.0	58	147	40	232	48	353
1250.0	32	205	60	272	0	0
1600.0	53	237	38	332	0	0
2000.0	43	290	21	370	0	0
2500.0	32	333	10	391	0	0
3150.0	23	365	0	0	0	0
4000.0	9	388	0	0	0	0
5000.0	4	397	0	0	0	0

TABLE 10. - PREDICTED NOISE REDUCTIONS FOR BASELINE CYLINDERS

Progressive wave over test specimen, N=8 ducts around periphery, CO_2 exterior

Cabin length = Fuselage length = 3.6575 meters

Trim: 6.35 cm, 2.54 cm insulation, 3.81 cm airgap, 1.25 kg/m^2 panel

Reduction = 20*log(P(EXT)/P(INT))

Composite Cylinder				Aluminum Cylinder			
1/3 Band	Octave Freq	P(INT)**2/ P(EXT)**2	Noise Reduction	1/3 Band	Octave Freq	P(INT)**2/ P(EXT)**2	Noise Reduction
1	50.0	0.0000E+00	0.00	1	50.0	0.0000E+00	0.00
2	63.0	0.0000E+00	0.00	2	63.0	0.0000E+00	0.00
3	80.0	0.0000E+00	0.00	3	30.0	0.0000E+00	0.00
4	100.0	1.1447E-05	49.41	4	100.0	4.6810E-05	43.30
5	125.0	9.0773E-07	60.42	5	125.0	5.0180E-06	52.99
6	160.0	9.5555E-06	50.20	6	160.0	4.6801E-06	53.30
7	200.0	5.2769E-06	52.78	7	200.0	1.4967E-04	38.25
8	250.0	2.5087E-05	46.01	8	250.0	6.7720E-06	51.69
9	315.0	2.2726E-06	56.43	9	315.0	1.5027E-05	48.23
10	400.0	1.5849E-06	58.00	10	400.0	1.0909E-05	49.62
11	500.0	2.4028E-06	56.19	11	500.0	7.6482E-06	51.16
12	630.0	1.8398E-06	57.35	12	630.0	4.9556E-06	53.05
13	800.0	1.3535E-06	58.69	13	800.0	1.9050E-06	57.20
14	1000.0	8.0825E-07	60.92	14	1000.0	1.1239E-07	69.49
15	1250.0	8.3268E-09	80.80	15	1250.0	5.0243E-09	82.99
16	1600.0	8.4853E-10	90.71	16	1600.0	1.0997E-98	89.59
17	2000.0	1.4892E-10	98.27	17	2000.0	9.6378E-11	100.16
18	2500.0	8.5884E-12	110.66	18	2500.0	2.1690E-12	116.64
19	3150.0	6.6049E-13	121.80	19	3150.0	0.0000E+00	******
20	4000.0	1.6110E-15	147.93	20	4000.0	0.0000E+00	******
21	5000.0	2.2547E-17	166.47	21	5000.0	0.0000E+00	******

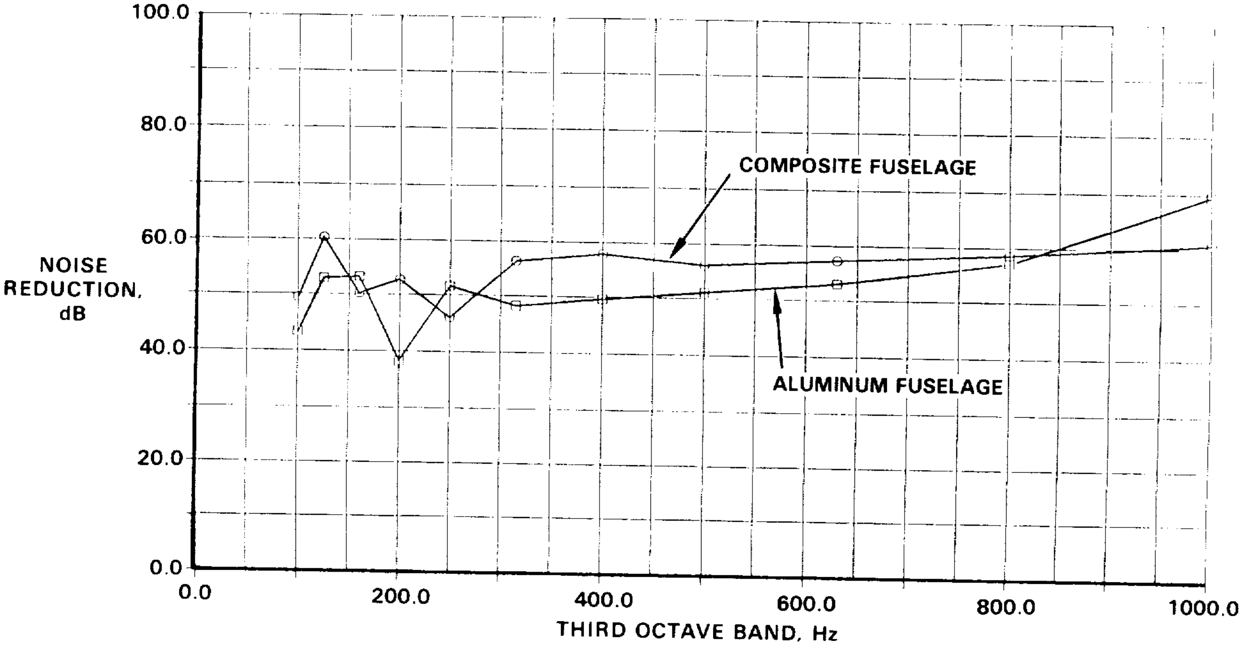

Figure 23. - Aluminum and composite cylinder noise reductions with $1.25\ kg/m^2$ trim and carbon dioxide exterior.

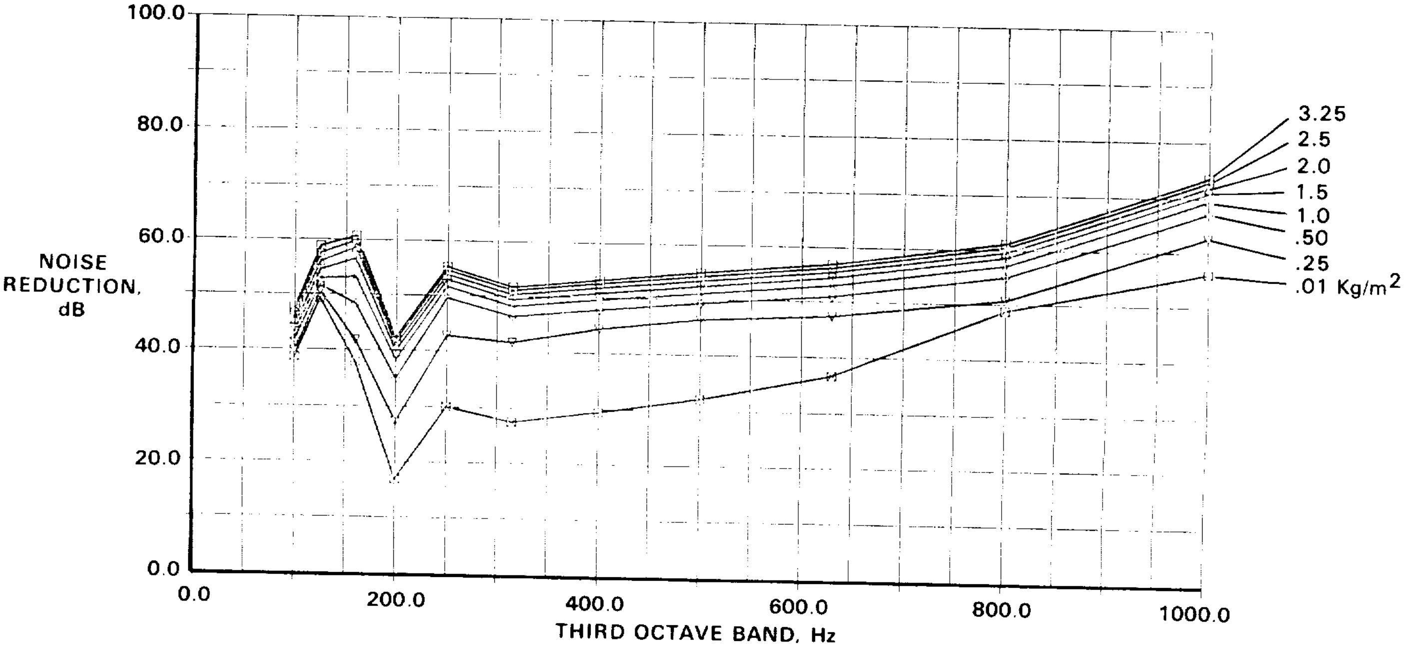

Figure 24. - Aluminum cylinder noise reductions with variable trim and carbon dioxide exterior.

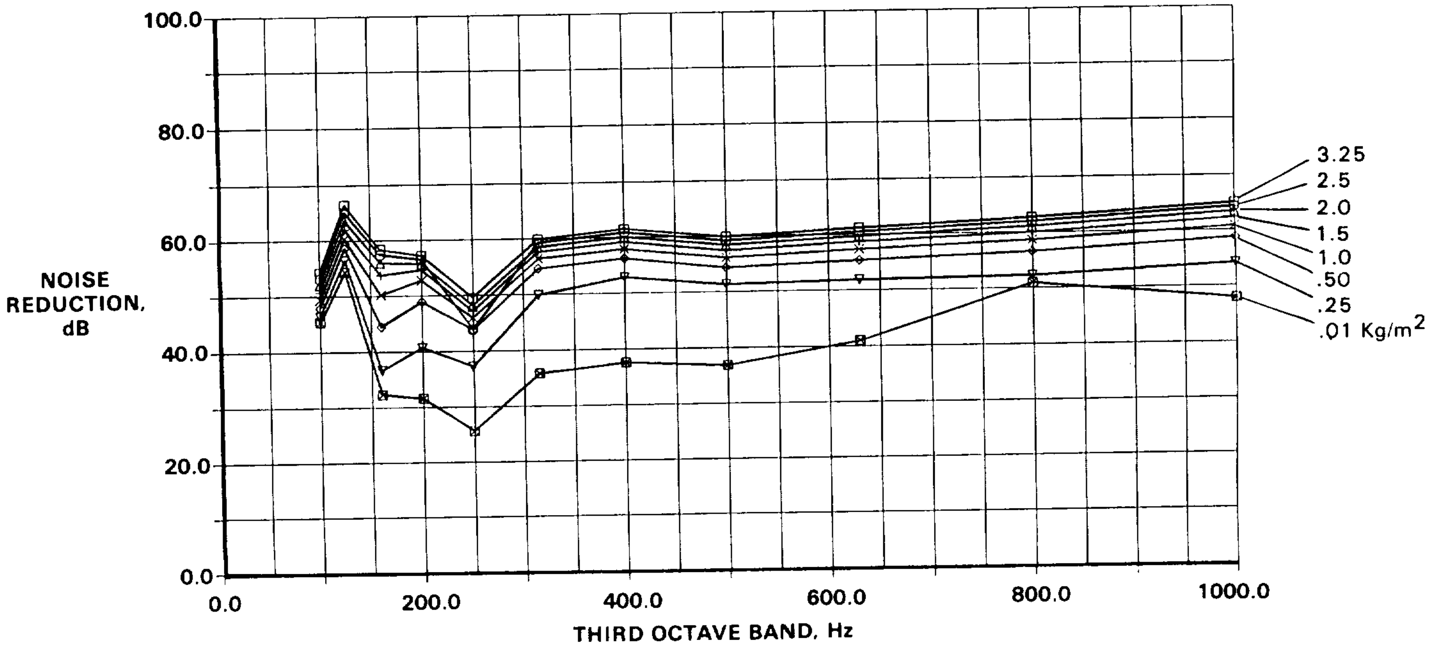

Figure 25. - Composite cylinder noise reductions with variable trim and carbon dioxide exterior.

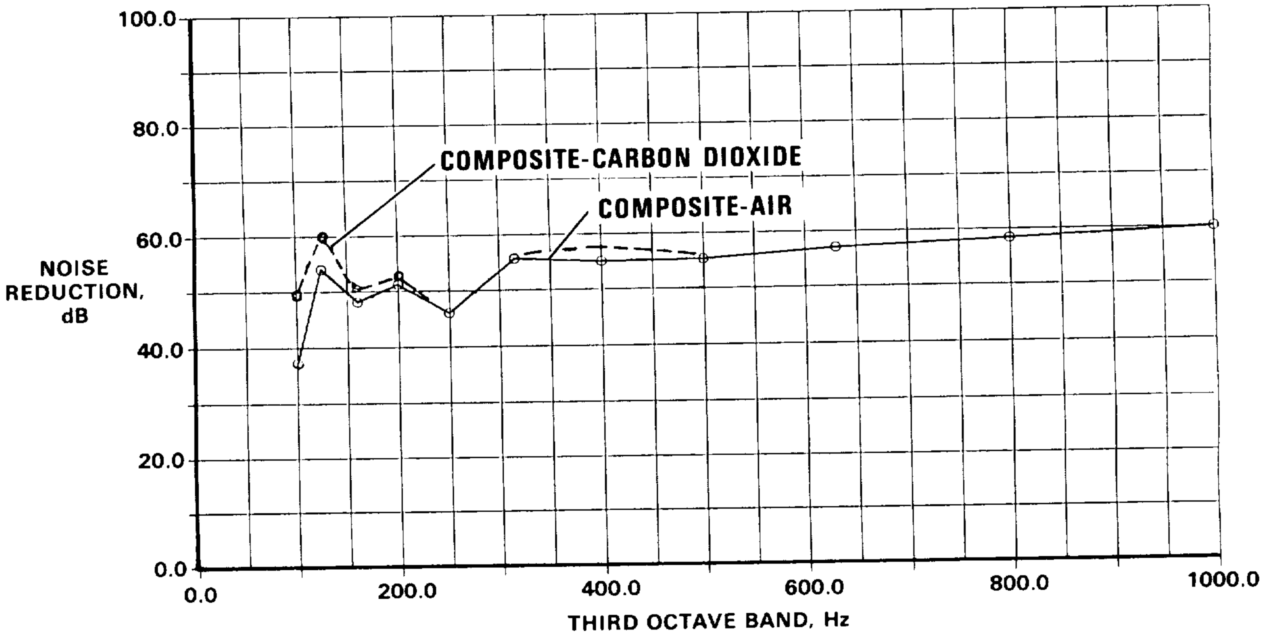

Figure 26. - Composite cylinder noise reductions with 1.25 kg/m^2 trim with and without carbon dioxide exterior.

3. TOOLING AND FABRICATION

3.1 Tooling and Fabrication of Impact Dynamics Specimens

The composite test elements consisted of blade-stiffened panels, hat-stiffened panels, corrugated panels, a Z-C curved frame/skin assembly and a curved corrugated frame/skin assembly. All elements were made from Hercules AS4/2220-1 graphite/epoxy material.

The hat-stiffened panels and the Z-C frame/skin assemblies were fabricated using aluminum tooling. The blade-stiffened panels, the corrugated panels and corrugated frames were fabricated using graphite tooling.

The hat-stiffened panel tooling concept is shown in Figure 27. It consisted of an aluminum base plate, solid aluminum mandrels and a formed rubber caulplate. The skin was laid up on the baseplate. The aluminum mandrels were then placed at the stiffener locations. Preplied, preformed hat laminates were placed over these mandrels. The rubber caul plate was placed over the assembly which was then bagged and cured. Two completed hat-stiffened panels with aluminum extruded T-caps are shown in Figure 28.

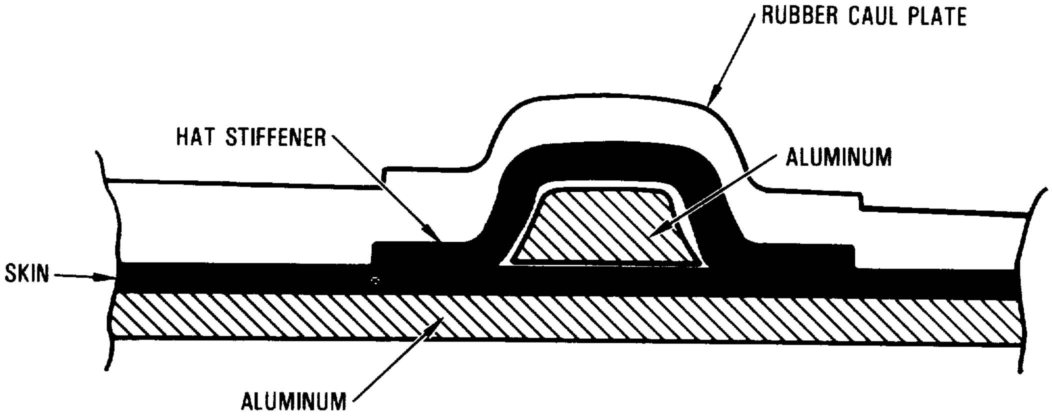

Figure 27. - Hat-stiffened panel tooling.

ORIGINAL PAGE IS
OF POOR QUALITY

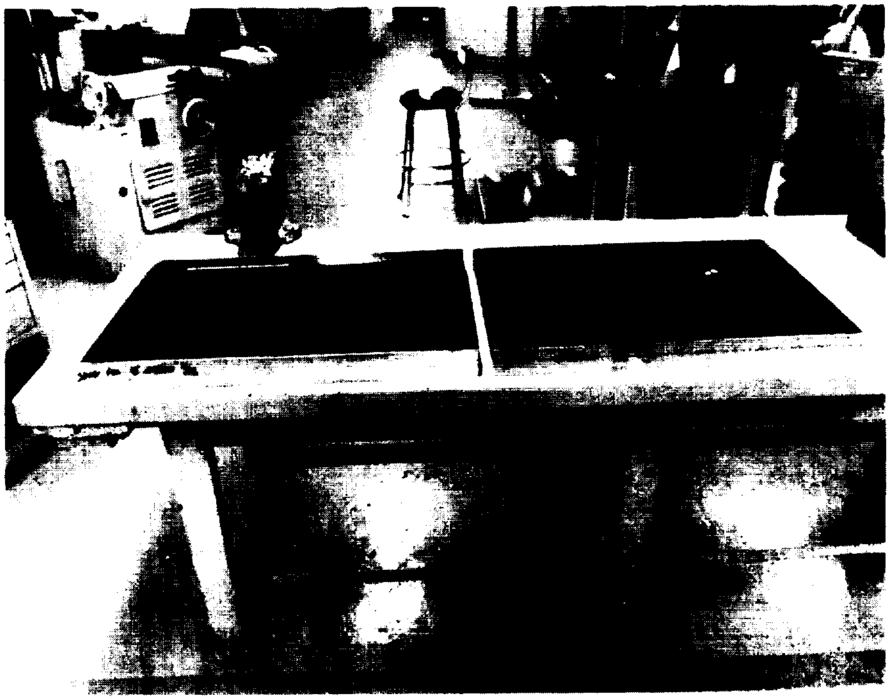

Figure 28. - Cured hat-stiffened panels.

Metal tooling was also used to fabricate the Z-C frames and skin. This tooling concept is shown in Figure 29. Thin layers of rubber were used in the tool to ensure compaction of the intermediate flange. The expansion of the aluminum tool core and the seating of the heavy aluminum caul provided excellent compaction of the remainder of the frame. A completed frame is shown in Figure 30. The skin was laid up and cured on a curved aluminum plate tool. Two frames and a skin were then mechanically attached to provide a complete assembly as shown in Figure 31.

The blade-stiffened panel was fabricated using graphite tooling. A combination of graphite and rubber was used to ensure that the blades could be properly located and co-cured. A graphite/epoxy tooling material (Fiber Resin 8618/1506) was selected. This material is capable of withstanding 350°F and can be cured at 250°F.

The tooling concept is shown in Figure 32. Graphite prepreg fabric was laid up in a plastic master mold and cured. The completed tool is shown in Figure 33. Thin strips of silicone rubber were used to provide the pressure to compact the upstanding legs of the blades. The composite skin was laid up on the graphite tool baseplate. Preplied, preformed angles were laid in place to form the blades as the remainder of the tool was assembled. The assembled tool was then bagged and the part was cured. Excellent parts were achieved.

ORIGINAL PAGE
BLACK AND WHITE PHOTOGRAPH

ORIGINAL PAGE IS
OF POOR QUALITY

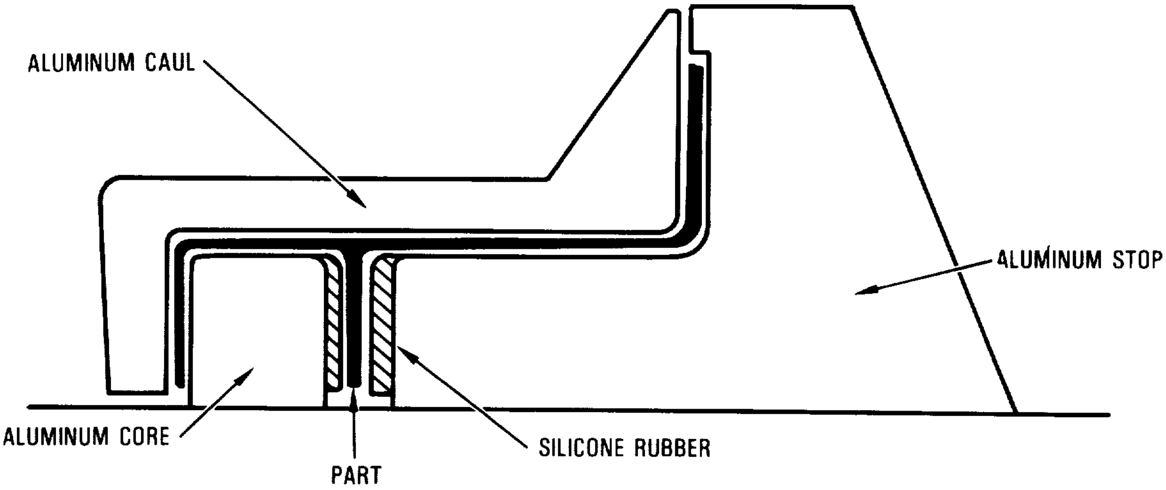

Figure 29. - Z-C frame tooling.

Figure 30. - Completed Z-C frame.

ORIGINAL PAGE
BLACK AND WHITE PHOTOGRAPH

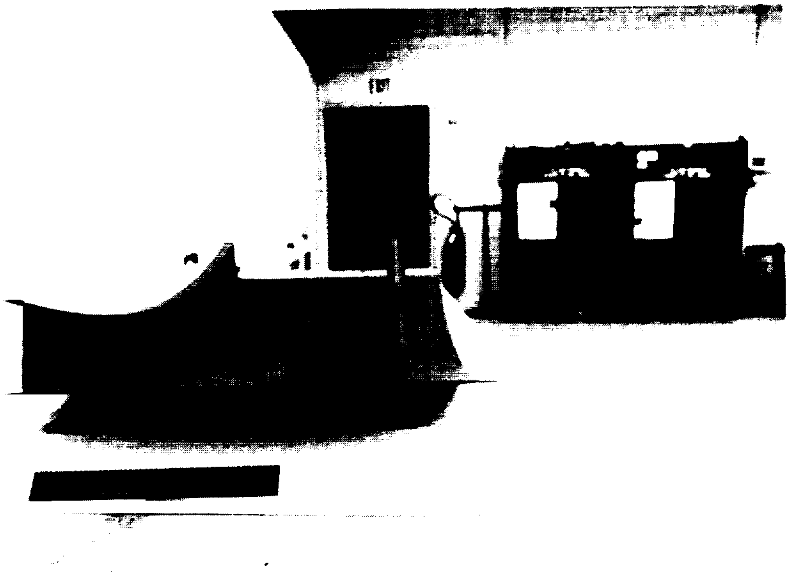

Figure 31. - Z-C frames and skin assembly.

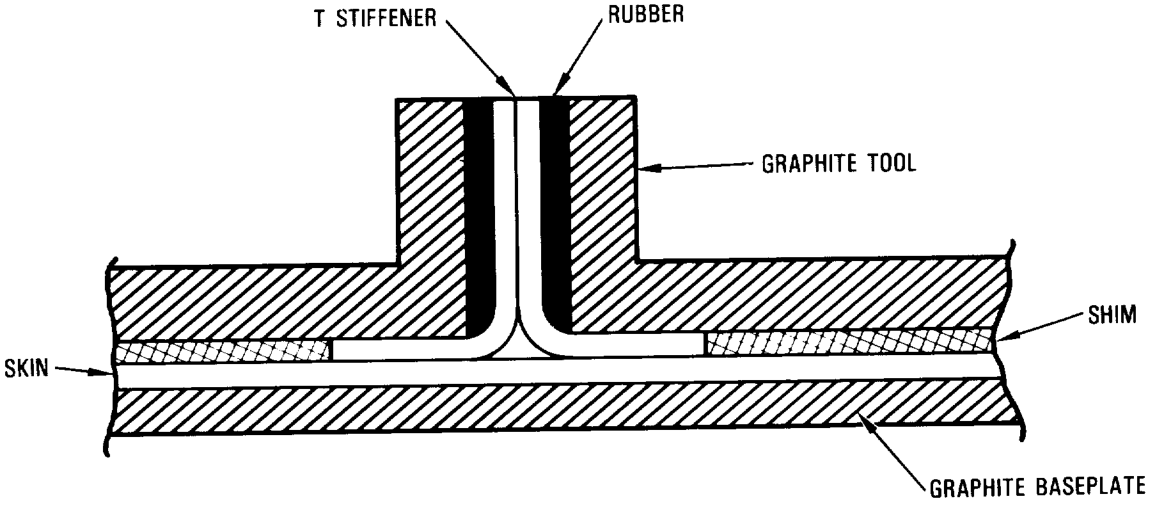

Figure 32. - Blade stiffened panel tooling.

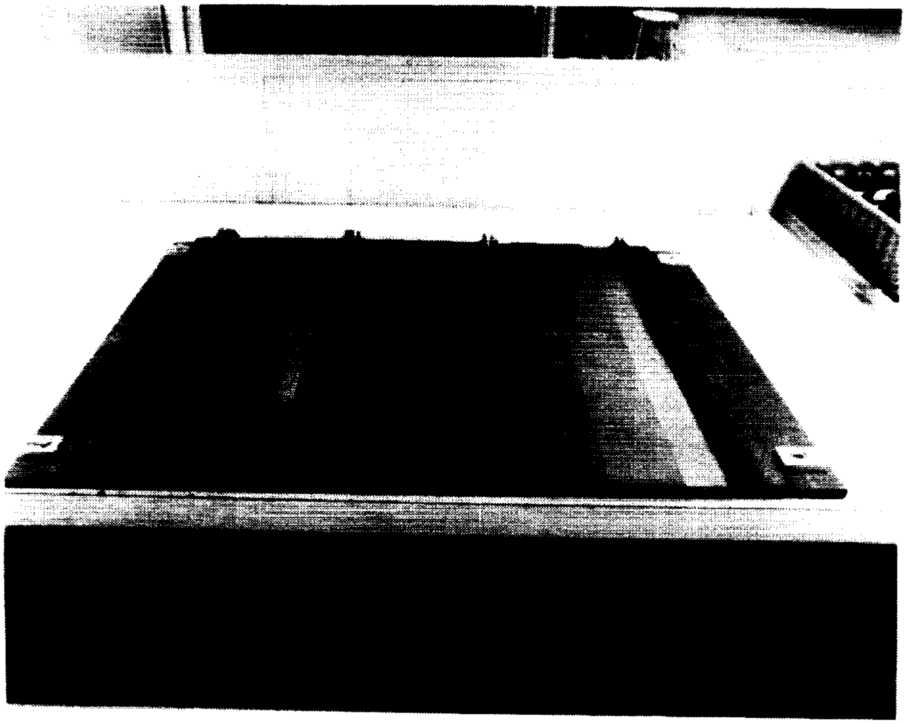

Figure 33. - Blade-stiffened panel curing tool.

The corrugation stiffened panel was an excellent candidate for graphite tooling because of the thermal expansion compatibility between the tool and the part. First, a master mold had to be fabricated; castable ceramic tooling material was selected for this mold. The material is Thermodel Castable 120. It was selected because its thermal expansion is compatible with the graphite epoxy tooling material, it was inexpensive at $1.25/lb., it was easy to mix and pour because the particle sizes ranged from 0.25 inch to 5 microns and it cured at room temperature in 24 hours.

The Thermodel Castable 120 turned out to have several problems. It was very brittle and had to be handled with extreme care when cured. It also reacts with aluminum so the master mold was manufactured using a silicone rubber. Ceramics are porous, so a surface treatment had to be found which would act as a release agent. Airtech Internationals Airseal 476 sealer was found to provide a satisfactory surface. Figure 36 shows the graphite/epoxy tooling material being laid into the ceramic mold.

The other half of the tool consisted of a formed silicone rubber caul-plate. The graphite and rubber tools are shown in Figure 35. The tooling was finally placed in a steel frame with silicone rubber strips to provide for compaction of the flanges.

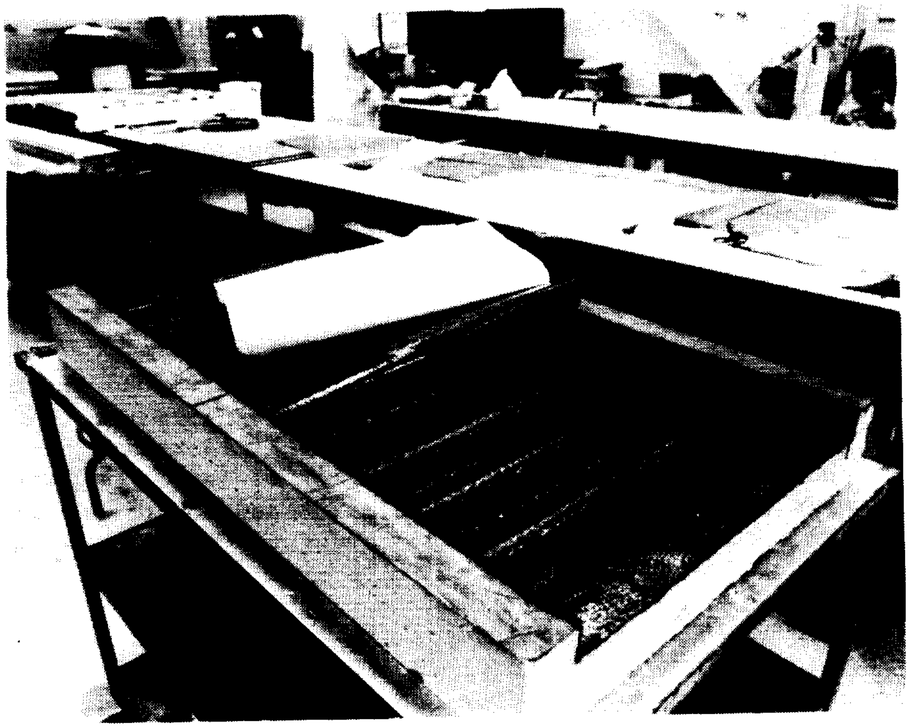

Figure 34. - Prepreg laid into ceramic for sine-wave panel tool.

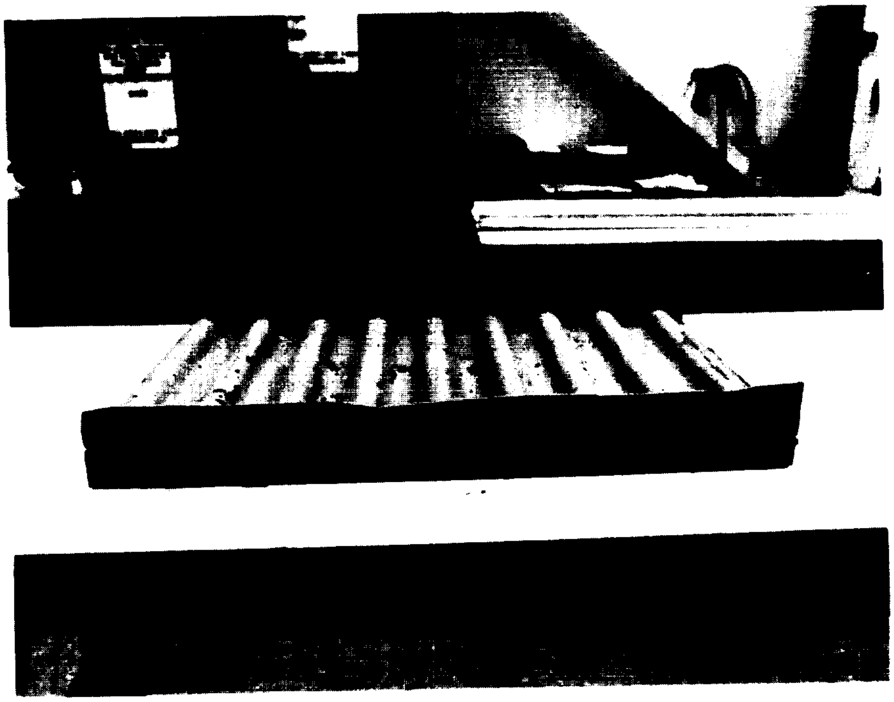

Figure 35. - Composite/rubber tooling for corrugated stiffened panel.

The material for the web of corrugated panels had to be folded and cut to form part of the flanges with a minimum of wrinkling. A cutting and splicing method was developed empirically. Figure 36 shows the cutting and folding sequence. Continuous cuts were made at the inflection points of each corrugation (cut A). For the convex section of the fold a triangular cut (cut B) was made. For the concave section of the fold a half moon cut (cut C) was made. A minimum of 0.15 in overlap from the web to the flange was maintained. The folded configuration is shown in the lower part of Figure 36. Vellum cutting templates were generated with CADAM. Additional plies were added to complete the flanges.

Vacuum bagging into three-dimensional corners and compound curves presented a bridging and potential bag break problem. To alleviate this problem, hollow aluminum 1/4 inch diameter beads were used to fill the cavities prior to bagging. The beads evenly distributed the pressure forces and provided a semi-flat medium for the bag. The beads were light and conducted heat well thus providing good components. A completed corrugated panel is shown in Figure 37.

The curved corrugated frame tooling was fabricated in the same manner as that for the corrugated panel. The completed composite tooling is shown in Figure 38. The corrugations for the frame were trapezoidal instead of curved. The cutting and overlapping of the web to form the flanges was thus able to be accomplished with straight cuts from point D as shown in Figure 39.

Aluminum beads were not needed to cure the frames. The smaller flange width on the frame allowed the frames to be just vacuum bagged and cured. A 0.06 inch graphite epoxy skin was cured on the curved aluminum tool used to cure the skin for the Z-C frame/skin assembly. Two curved corrugated frames were mechanically attached to the skin. The final assembly is shown in Figure 40.

3.2 Tooling and Fabrication of Acoustic Cylinder

The aluminum mandrel for filament-winding the shell was fabricated by the Westinghouse Electric Corporation, Bethel Park, Pennsylvania. The mandrel is shown in Figure 41. The mandrel outer shell was welded to headers, which were in turn welded to the tubular aluminum center shaft. Scribe lines were incorporated in the surface to produce minute resin ridges on the inside of the filament-wound shell to serve as locators for the stringers during assembly.

The frames and frame clips were made by the Xerkon Company, Minneapolis. The tooling concept for frames is shown in Figure 42. The frames were made in three sections, which were joined during assembly. One tool made all sections. Modified segments of the frame sections were used to make splice plates for joining the frame sections. The frame tool was used by Xerkon in their Autocomp™ molding process. This process uses fluid pressure on an enveloping membrane surrounding the tool, which is integrally heated. Pressure is applied in a small autoclave-type vessel in which the tool is placed.

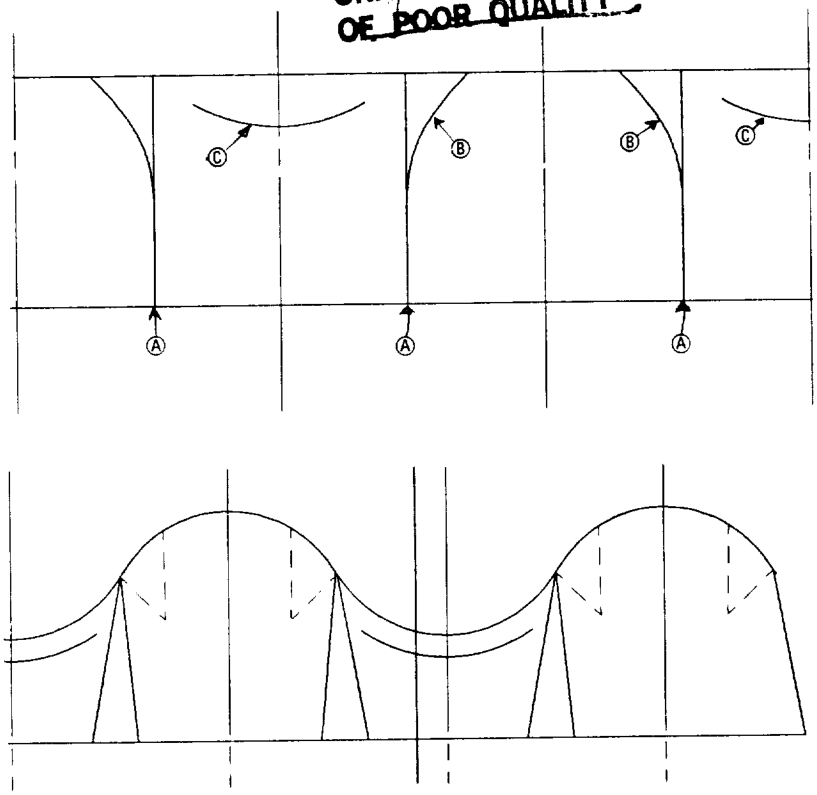

Figure 36. - Cutting of flanges for straight sine wave.

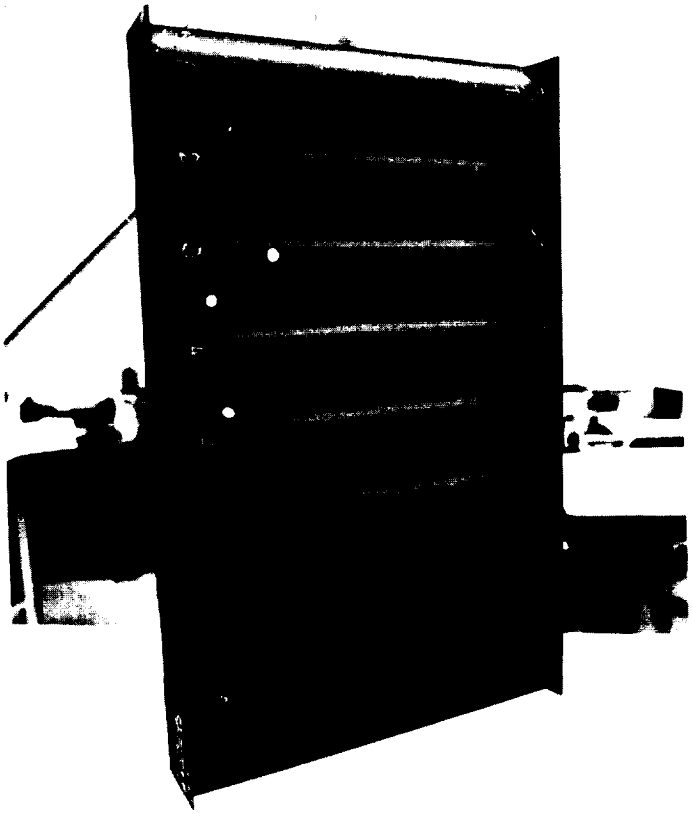

Figure 37. - Corrugated stiffened composite panel.

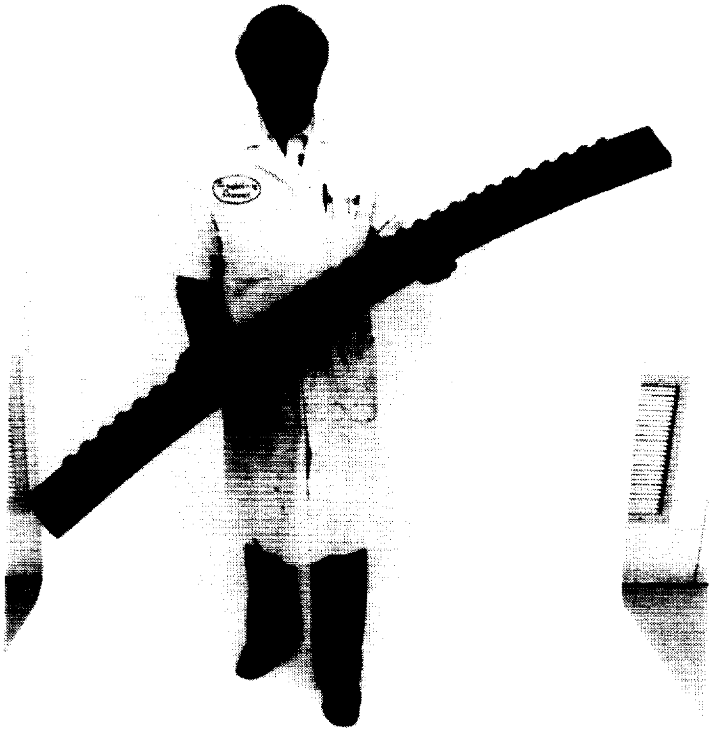

Figure 38. - Composite tool for corrugated frame.

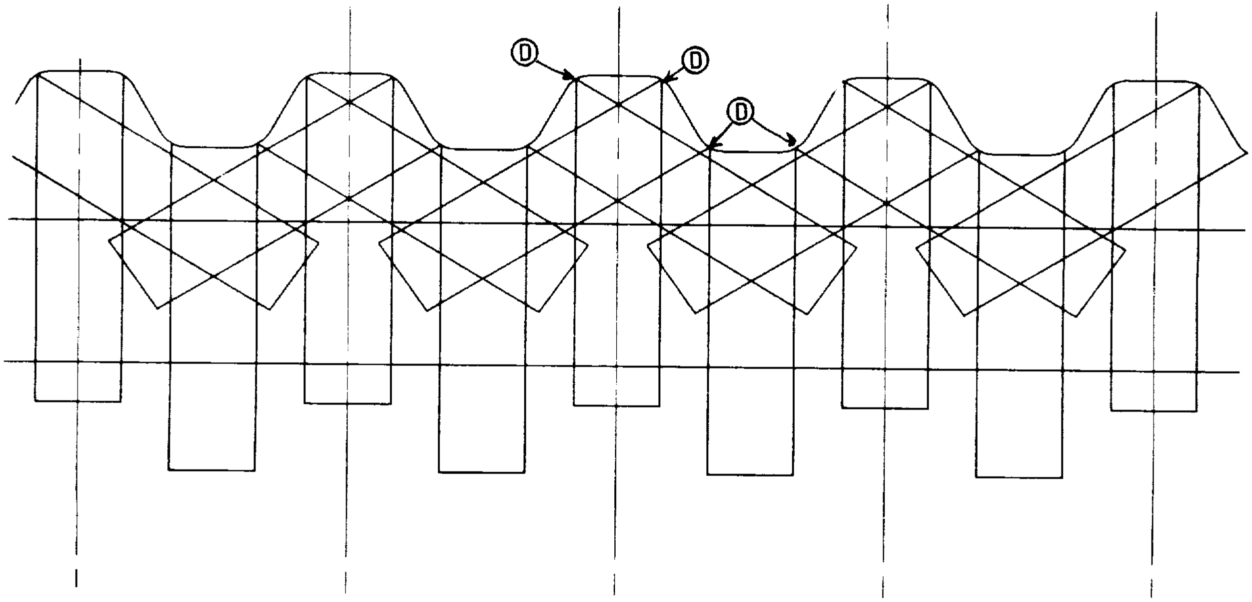

Figure 39. - Cutting of flanges for curved corrugated stiffener.

ORIGINAL PAGE
BLACK AND WHITE PHOTOGRAPH

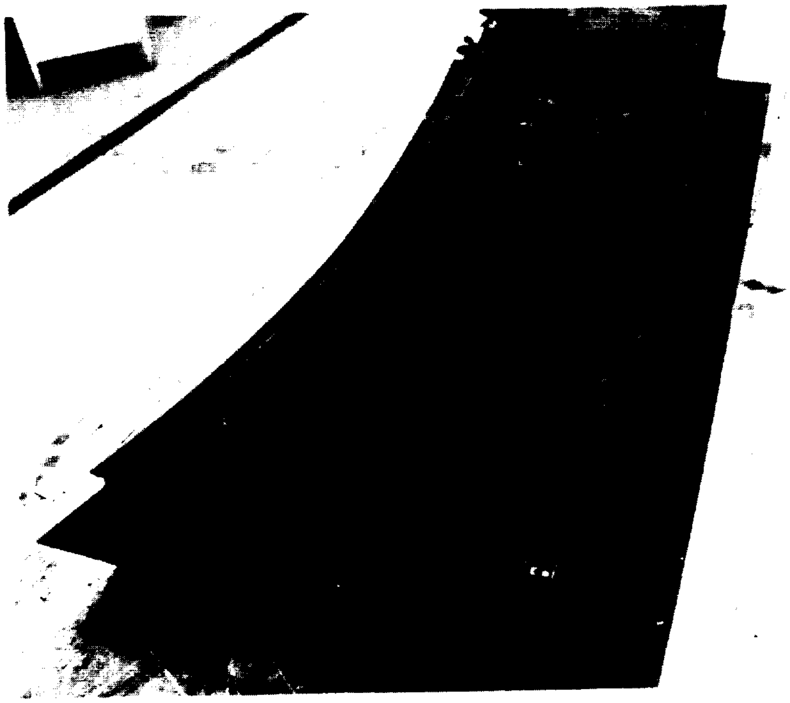

Figure 40. - Composite corrugated frame/skin test panel.

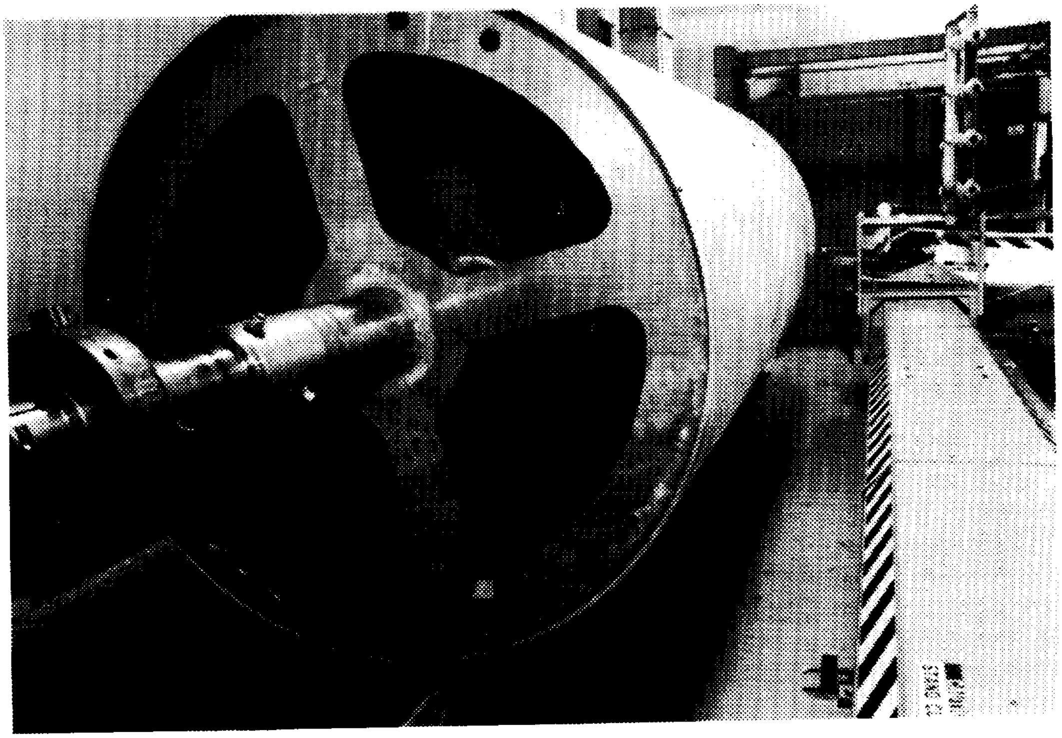

Figure 41. - Mandrel mounted in filament winder.

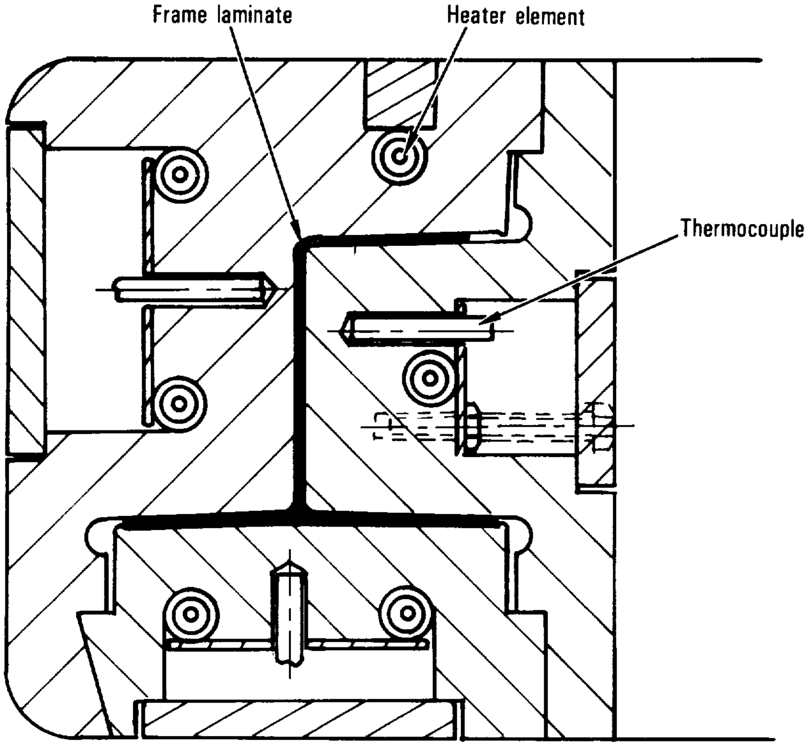

Figure 42. - Cross section of frame tool.

The Autocomp™ process offers the advantage of short cure cycles, and the ability to vary ply orientation from point to point, such as around the the frame. For example, the ±45° orientation in the frame web was maintained continuously around the frames. The process also lends itself to economy of material usage. The short cure cycle results, in part, from internally heating the tool. The clips were made by the same process.

The tool for molding the hat-section stringers is shown in Figure 43. This tool was available from a previous program. It accommodates multiple stringers in a single tool loading.

3.2.1 <u>Shell fabrication</u>.- The filament-winding mandrel is shown in the winder in Figure 41, prior to the addition of the overwind receptacles. Release agent was applied to the mandrel and the shell was wound with Fiberite T500-6K/934 towpreg. Eight spools of tow fed through the payout head to form the band of tow laid down on the mandrel. The first ±45° wind pattern is shown in progress in Figure 44. The reflection from the aluminum mandrel through the single-ply layers shows the gaps experienced with the 6K tow spread to provide a nominal 7.4 mil ply thickness.

~~ORIGINAL PAGE IS~~
~~OF POOR QUALITY~~

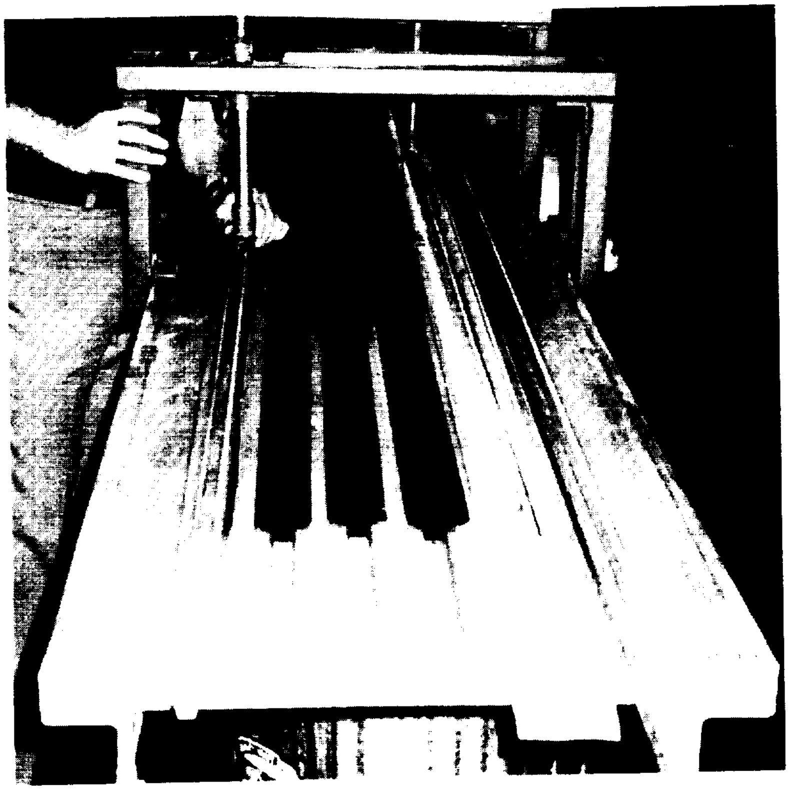

Figure 43. - Stringer tool.

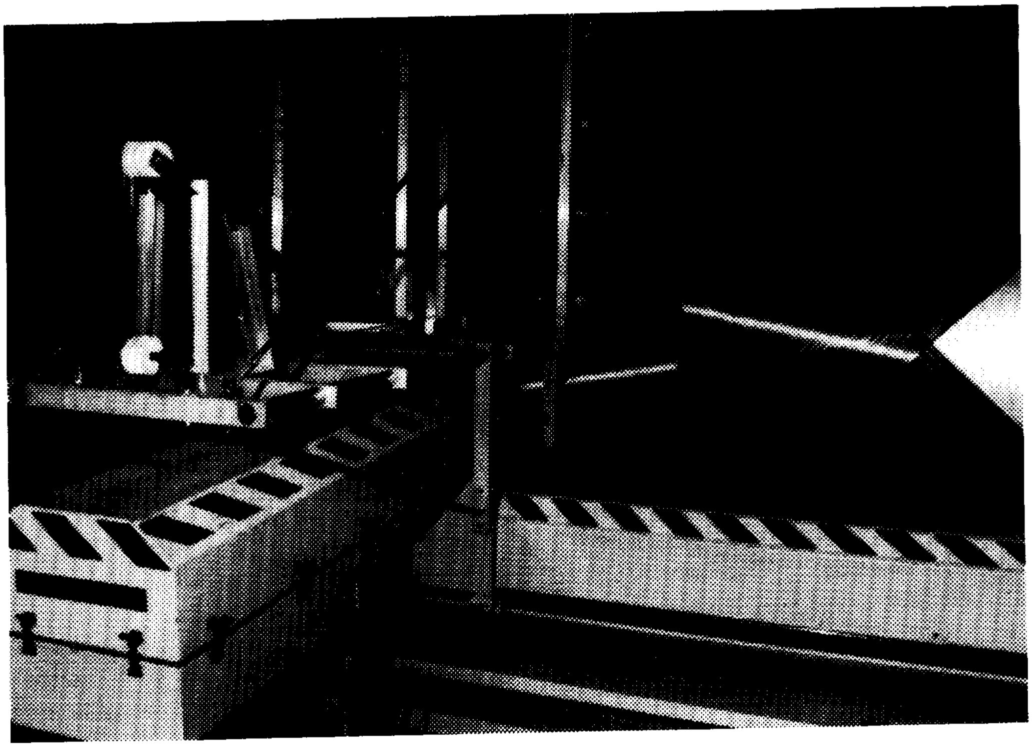

Figure 44. - Winding of first ± 45-degree plies in progress.

ORIGINAL PAGE
BLACK AND WHITE PHOTOGRAPH

Since previous experience, primarily with 12K tow, had shown that the tows leveled well when cured under a caul sheet, it was expected that most of the gaps would disappear during cure. Photomicrographs, made of cross sections of trim material confirmed that most cross sections were free of gaps.

The sequence of additional winds included a ±32-degree wind, a 90 degree (hoop) wind, a second ±32 degree wind, and a second ±45-degree wind for a total of 9 plies. Figure 45 shows the completed winding.

Following completion of the filament winding, the overwind was trimmed to the edge of the mandrel. The trimmed shell is shown in Figure 46. The 150-inch mandrel provided for 3 inches of additional trim at each end after cure.

In preparation for curing, release film was applied and aluminum caul sheets were installed, as shown in Figure 47. Breather material was applied, followed by the vacuum bag. The bag was sealed to the edges of the mandrel and a vacuum was drawn.

The bagged shell was trucked to the Lockheed Charleston (South Carolina) plant overnight and cured the next day. The cured shell was debagged and the breather and caul sheets were removed. The thermal contraction of the aluminum mandrel left the shell free to move. The shell was slid along the mandrel and trimmed on each end. The shell was inspected ultrasonically for voids and porosity while still on the mandrel. No discrepancies were found.

At this stage of fabrication the unsupported shell was flexible and awkward to handle. No handling fixtures were provided for mandrel extraction. The most practical approach was to hoist the mandrel vertically. This was accomplished satisfactorily. Then the shell was moved to the assembly position and placed, still in a vertical posture, on a stand. Figure 48 shows the shell being placed on the support stand which had a center opening to facilitate operator entry for assembly work.

The J-section frames were procured from the Xerkon Company, who made them by their Autocomp™ process. Preforms made of T300 fiber were infused with 3501-6 resin and cured in an integrally heated tool under 85 psi pressure. Maximum temperature in the cure cycle was 400°F.

The overall quality of the parts was excellent. They did exhibit some discrepancies, which were determined to be acceptable. The principal discrepancy was in the thicknesses of the base flanges of the frames. (Resin contents were later found to vary in a sampled cross section from 30 to 46 percent.) The thickness variation was due to a tool discrepancy which could have been corrected. The associated delay was judged to be unwarranted, since the thickness variation could be tolerated.

The assembly requirement was for 220 clips. The clips were also procured from Xerkon, using the Autocomp™ process. They were made from AS4 preforms infused with 3501-6 resin. The tool made three clips per cycle.

ORIGINAL PAGE IS
OF POOR QUALITY

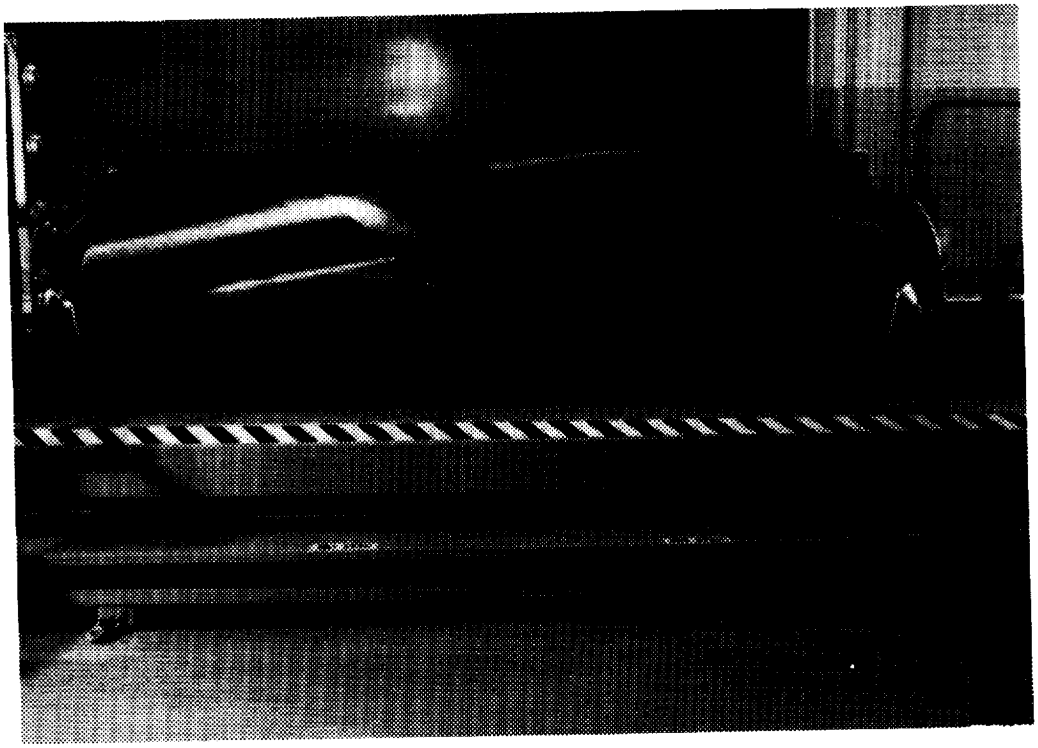

Figure 45. - The winding complete.

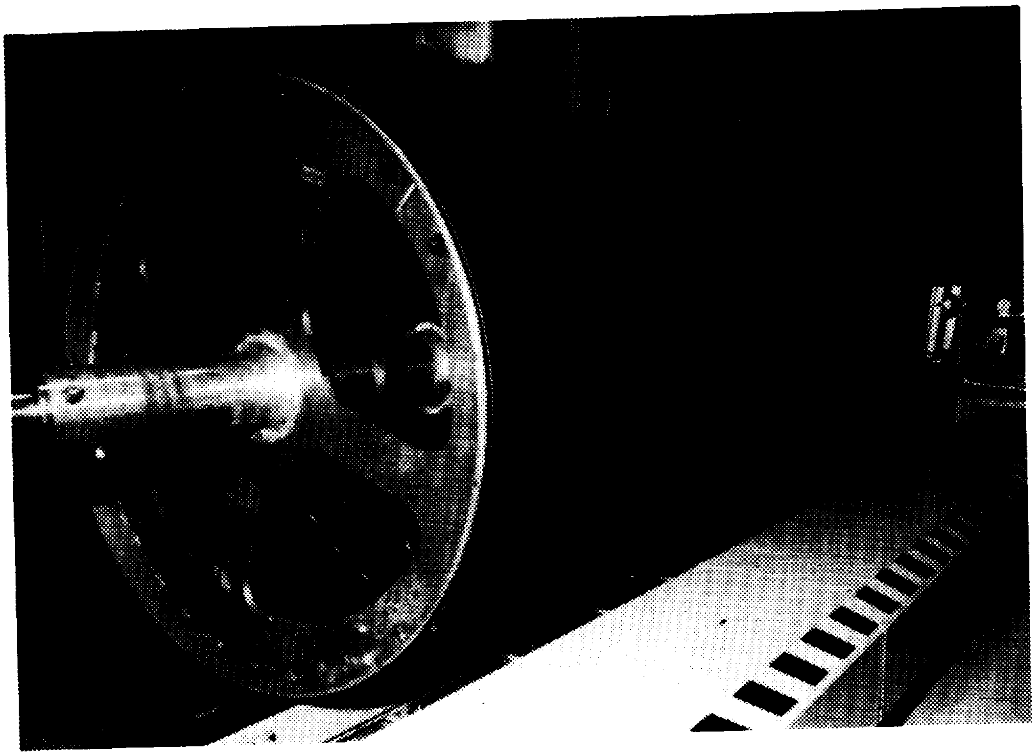

Figure 46. - Wound shell trimmed for bagging.

ORIGINAL PAGE
BLACK AND WHITE PHOTOGRAPH

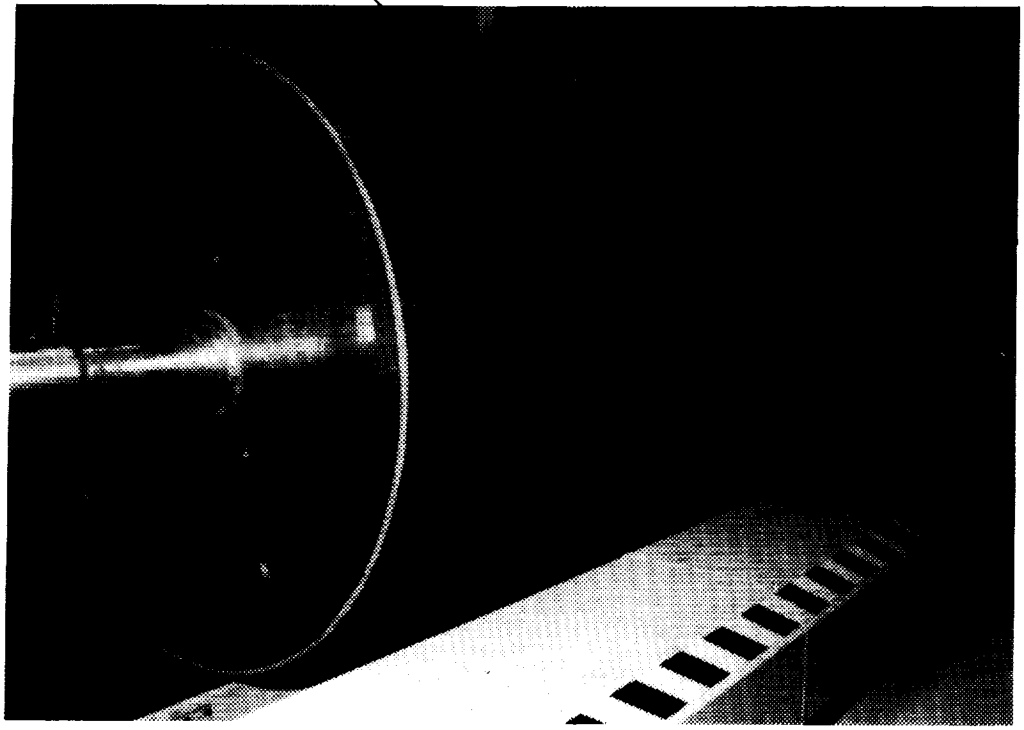

Figure 47. - Caul sheets in place.

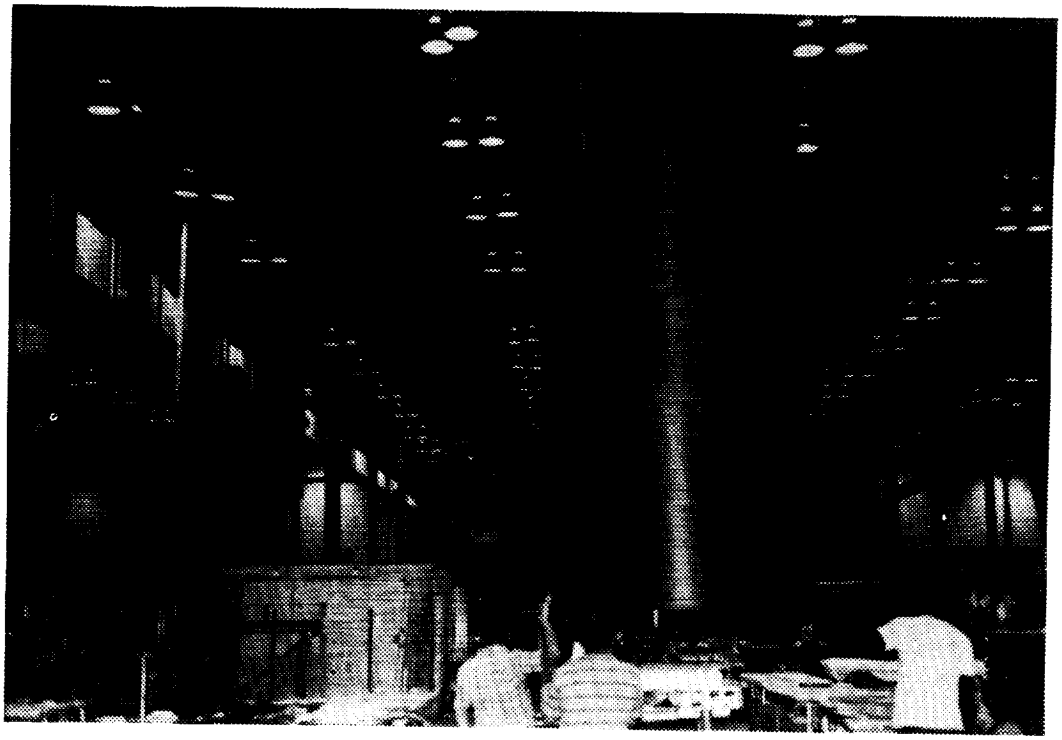

Figure 48. - The shell being moved into position for support structure assembly.

The stringers were made by conventional, hand layup methods using an existing tool. Since the tool provided for multiple stringers, only three tool loads were required to make the 22 stringers. The stringers were made of AS4/3501-6 tape prepreg.

3.2.2 Assembly.- The support structure was assembled with the shell entirely by "rivet-bonding" with Hysol EA 9304.2 epoxy paste adhesive containing 5 percent glass microballoons. Bonding pressure was applied by NAS1921 and NAS1919 monel rivets, which were left in the assembly.

First, the stringers were positioned at locations established by molded-in markings on the inner surface of the shell. The locating lines were molded in the shell by scribe lines in the filament-winding mandrel. The stringer bonds were cured in an autoclave which was used as an oven since the available oven was not high enough for the 12-foot shell standing upright.

The frames were assembled from three segments and three splice plates. The frames were preassembled on a template, as shown in Figure 49. The holes for splice plates were drilled and the frames disassembled for application of adhesive. The frames were reassembled in the shell and located by a spacer shown in Figure 50. Following frame installation, the assembly was turned to a horizontal position and placed in a cradle. Acceptability of the stringer and frame bonds was confirmed by ultrasonic evaluation.

A simulated floor was required in the fuselage section for acoustic tests. Since there was no need for a composite floor substructure, an extruded aluminum channel was used. The installed substructure is shown in Figure 51. A 0.5-inch plywood floor was bolted to the substructure. Aluminum sheet metal angles were used to join the plywood floor panels to the shell.

The completed fuselage section is shown in Figure 52. The assembly was shipped to NASA Langley Research Center for test.

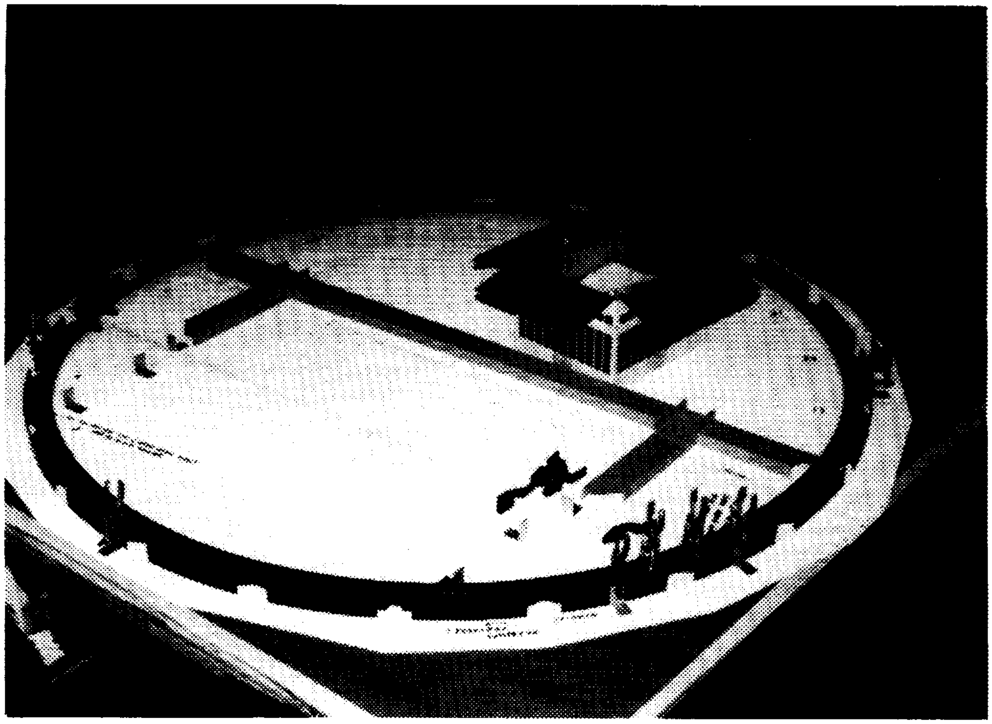

Figure 49. - The frames being preassembled and drilled prior to installation.

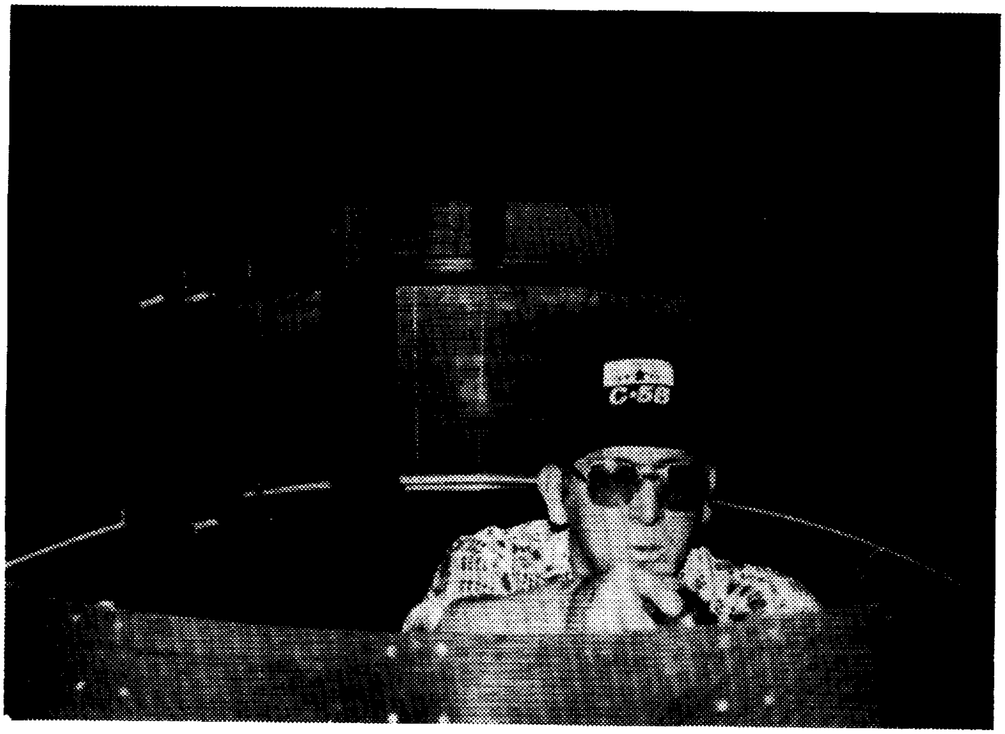

Figure 50. - The frames installed with the aid of a spacer.

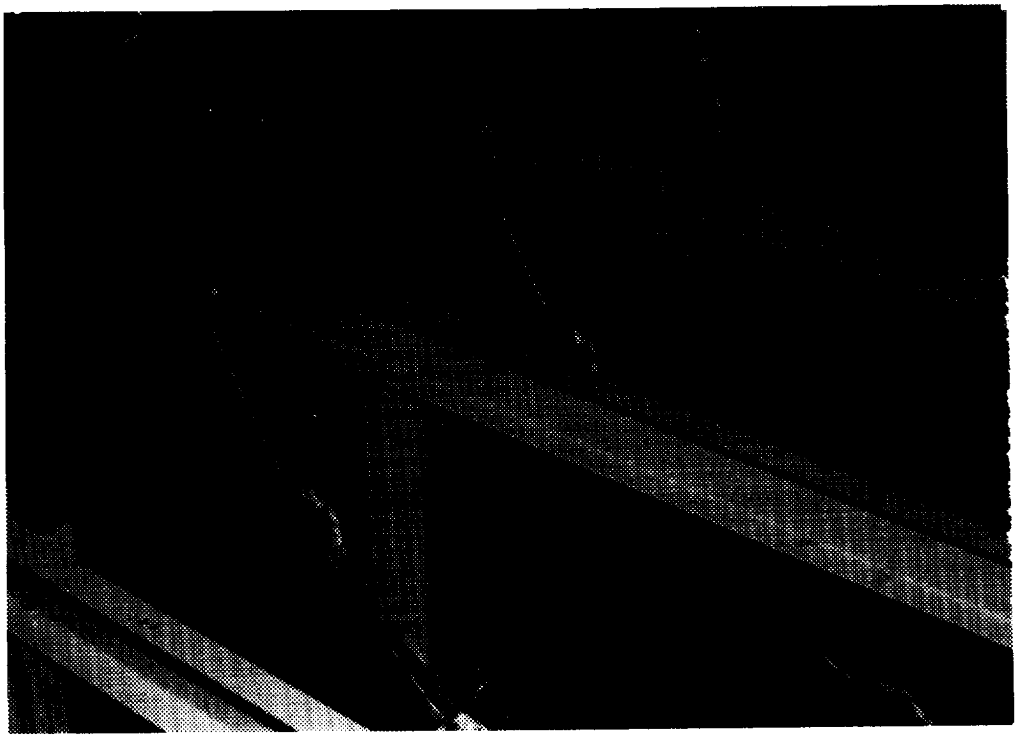

Figure 51. - Aluminum substructure to support a plywood floor.

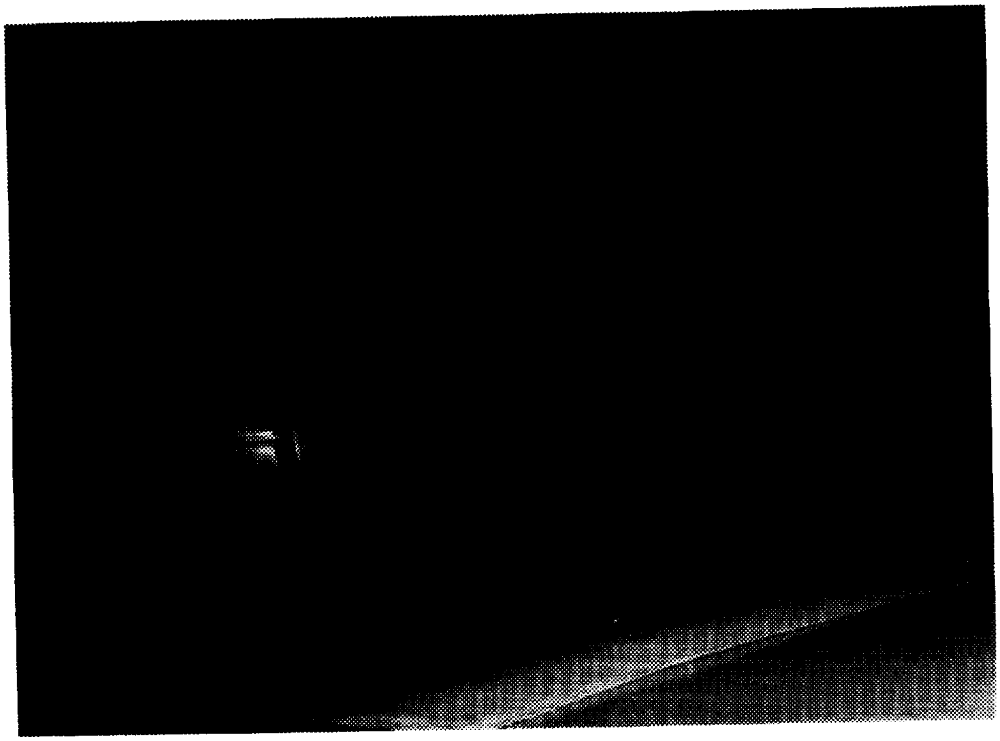

Figure 52. - Completed fuselage section.

4. TECHNOLOGY DEMONSTRATION

The use of composite design configurations in conjunction with, or in lieu of, current metal designs for dynamic impact conditions requires the following:

- a definition of design requirements
- a quantification of current design capability
- provisions for equivalent capability to current designs

Design requirements for transport category aircraft are specified either in regulations and/or special conditions. One such requirement is defined in paragraph 25.561 of Reference 5. While future changes to the regulations are always a possibility, the design for composites will still be governed by the same conditions as metals.

The quantification of metal design behavior under crash conditions has improved significantly in recent years as a result of NASA/FAA sponsored research which has included section drop tests, full-scale impact tests and analytical methodology development. The definition of current metal design crash performance is measured quantitatively in terms of peak load, deflection, specific failure load and energy absorption, and load uniformity ratio as depicted in Figure 53. With the quantification of the performance of metal designs by tests and/or analyses, the basis for composite designs can be established. For example, analytical studies of fuselage structure below the cargo floor, show that the load-deflection of a frame and stiffened panel under an impact load can behave as shown in Figure 54. Structural components fabricated of composite material, located in the same region and subjected to the same loading and direction, need to exhibit similar characteristics.

The results of this study provide substantial inputs to determine the adequacy of the composite design concepts for meeting impact dynamic requirements. Tests of both metal and composite structural element designs under similar loading conditions allows for a comparison of their crash performance behavior. The performance is quantified in terms of peak failure load, average force, and energy absorption efficiency (load uniformity ratio, specific energy absorption). Both stiffened panel and frame segment response data were obtained and comparisons between metal and composite designs were made.

4.1 Panel Static Tests

Cargo sub-floor panels were statically crushed in a test fixture and subjected to a crushing deflection, which is defined as a deflection parallel to the direction of the applied compression load. The crushing deflections were applied at rates between 0.4 in/min to 0.67 in/min. The results of the individual tests are described below.

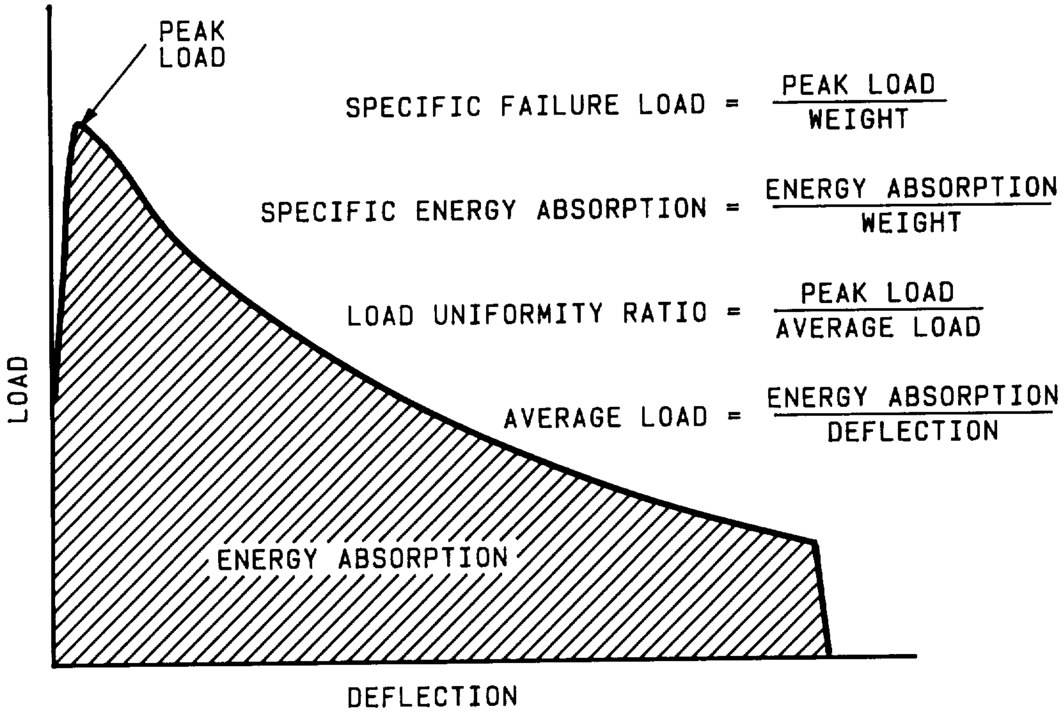

Figure 53. - Load deflection and energy absorption parameters

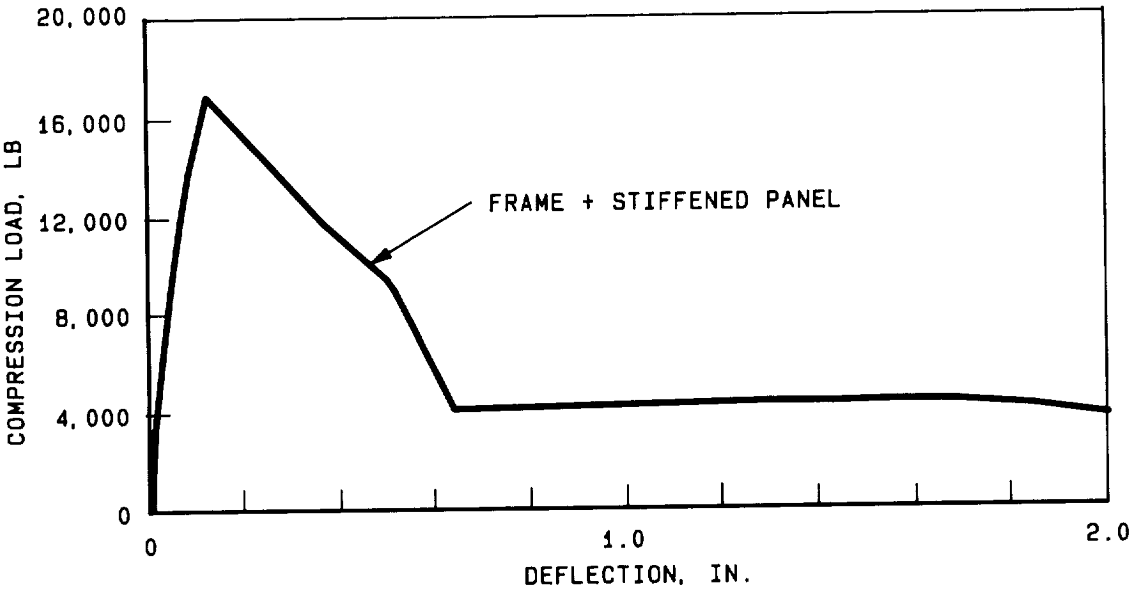

Figure 54. - Predicted load-deflection curve for below cargo floor structure.

4.1.1 Blade-stiffened metal panel.- The applied compression load reached a maximum of 15,680 pounds and then dropped at a fairly constant rate. After 360 seconds, the loading rate was increased to 0.55 in/min for 200 seconds. The compression load continued to drop to approximately 7200 pounds. Then the four blade stiffeners failed in tension and the compression load dropped abruptly to 1900 pounds. The load then remained relatively constant until the test was halted after 550 seconds. The deflected shape of the panel following the failure of the stiffeners can be seen in Figure 55. When the test was halted the specimen had crushed slightly over 2 inches. The load versus deflection curve is shown in Figure 56.

4.1.2 Hat-stiffened composite panel.- The applied compression load reached a maximum of 14,820 pounds at a crushing deflection of 0.12 inch. The load then dropped rapidly to approximately 1000 pounds at about 0.5 inch crushing deflection. The load then continued to decrease slowly until the test was terminated at a crushing deflection of about 2.5 inches.

The failed panel is shown in Figure 57. The left-hand stiffener separated from the skin at the top of the panel when the mechanical fasteners connecting the panel to the attachment flanges pulled through. The center and the right-hand stiffeners both failed in a similar manner, except failure initiated at the bottom. In all cases some of the hat stiffener flange material remained attached to the skin. The stiffeners separated from the skin to approximately the midspan and remained straight while the web bent about the midspan. The load versus crushing deflection is shown in Figure 58.

Strain gage data indicate that the panel starts to bend when the skin strain reaches 0.0005 in./in. and that the skin deformed in bending after stiffener separation occurred.

4.1.3 Blade-stiffened composite panel.- The applied compression load reached a maximum of 14,460 pounds, dropped sharply to approximately 1500 pounds them decreased slowly to less than 500 pounds. The test was terminated at about 2.5 inches of crushing deflection. The failed panel is shown in Figure 59. The failure mode was the same as for the hat-stiffened composite panel. Load versus crushing deflection is shown in Figure 60.

~~ORIGINAL PAGE IS~~
OF ~~POOR QUALITY~~

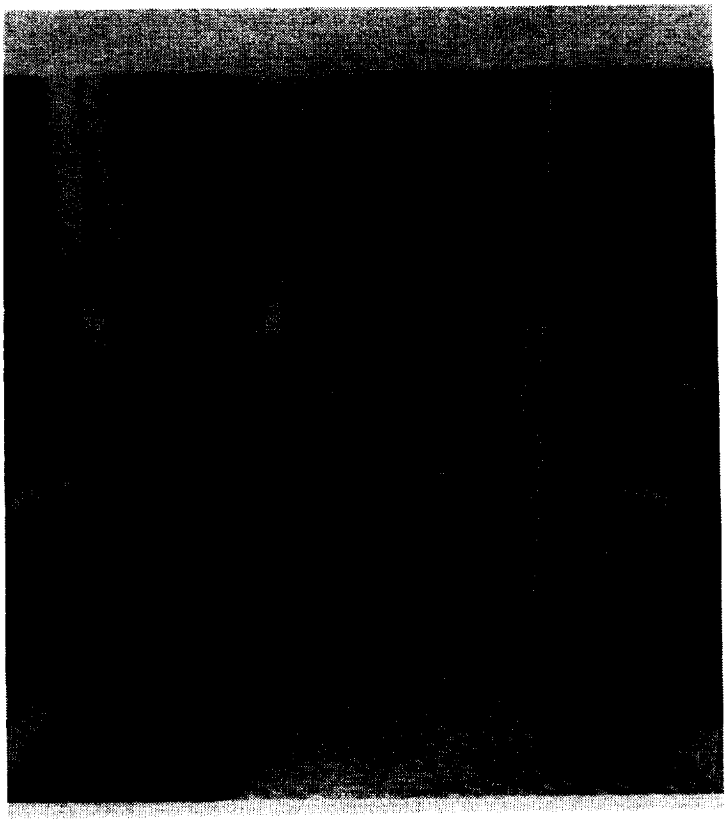

Figure 55. - Deflected shape of test specimen prior to failure of stiffeners, blade-stiffened metal panel.

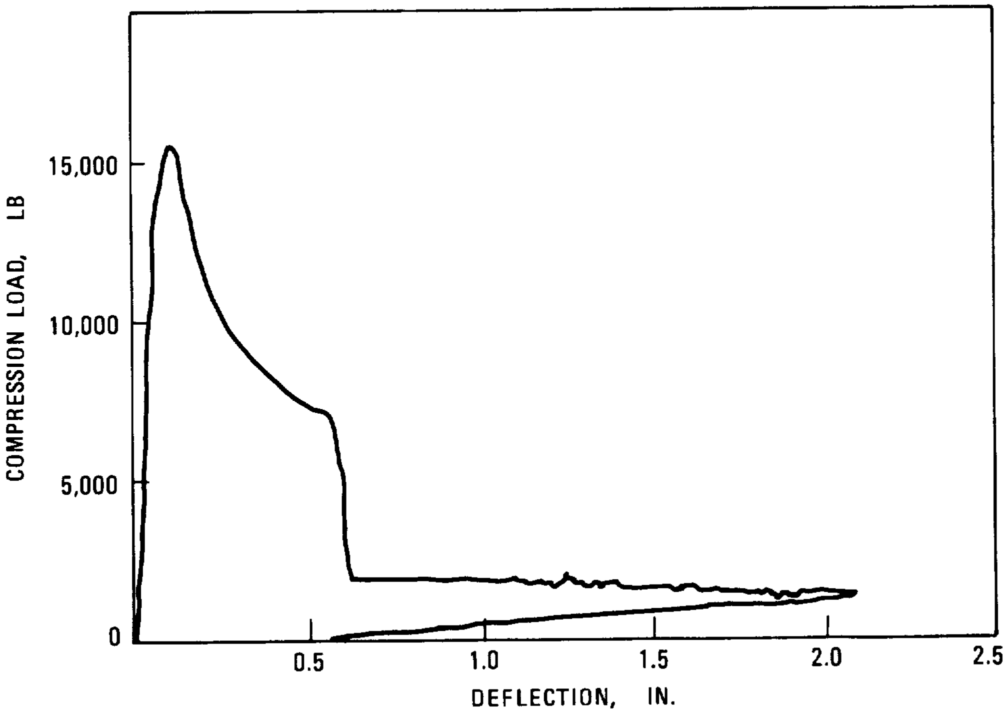

Figure 56. - Measured load versus deflection, blade-stiffened metal panel.

ORIGINAL PAGE
BLACK AND WHITE PHOTOGRAPH

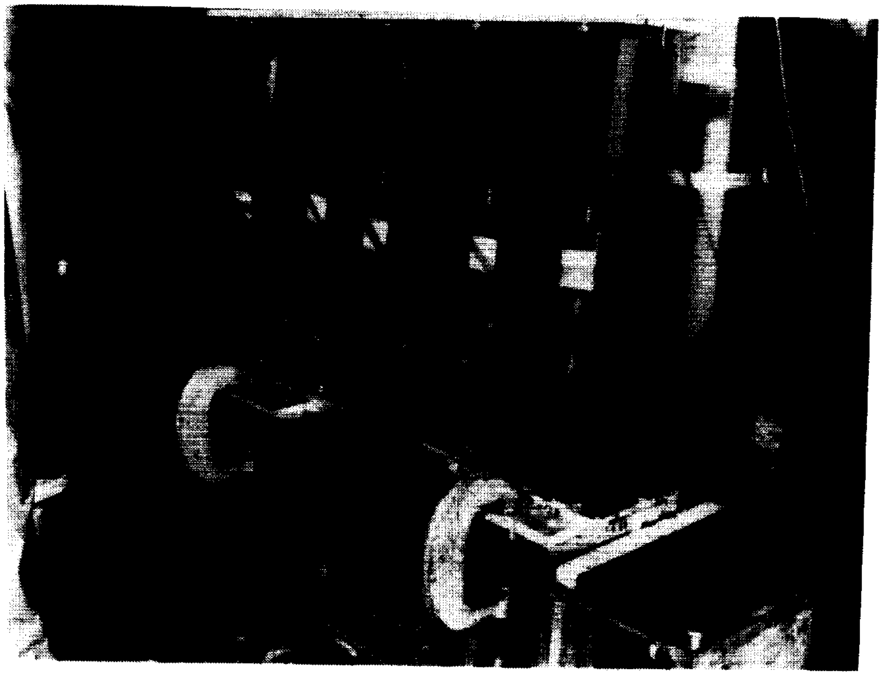

Figure 57. - Failed panel from stiffener side, hat-stiffened composite panel.

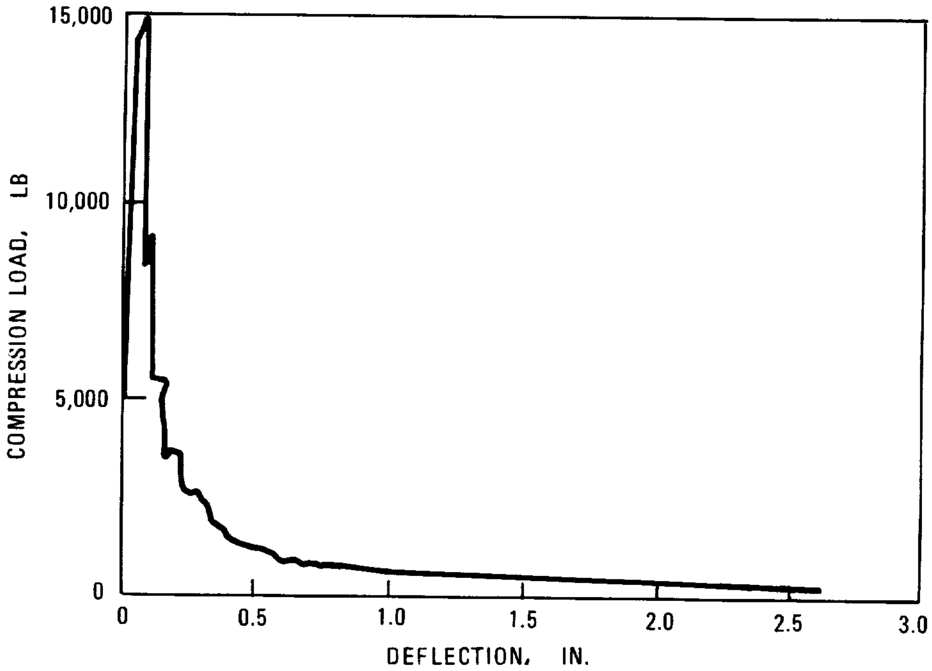

Figure 58. - Measured load versus deflection, hat-stiffened composite panel.

ORIGINAL PAGE IS
OF POOR QUALITY

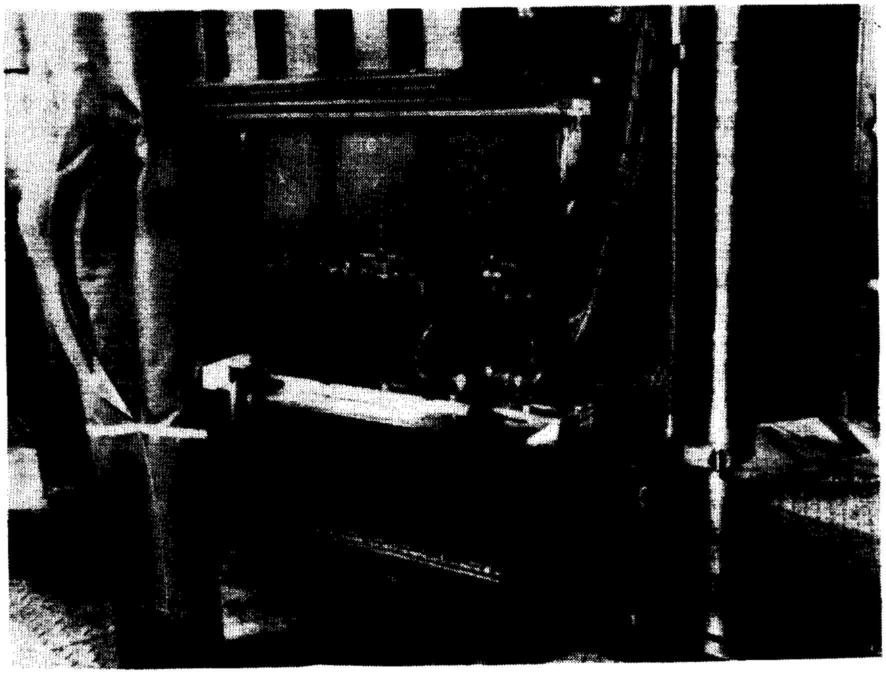

Figure 59. - Failed panel from stiffener side, blade-stiffened composite panel.

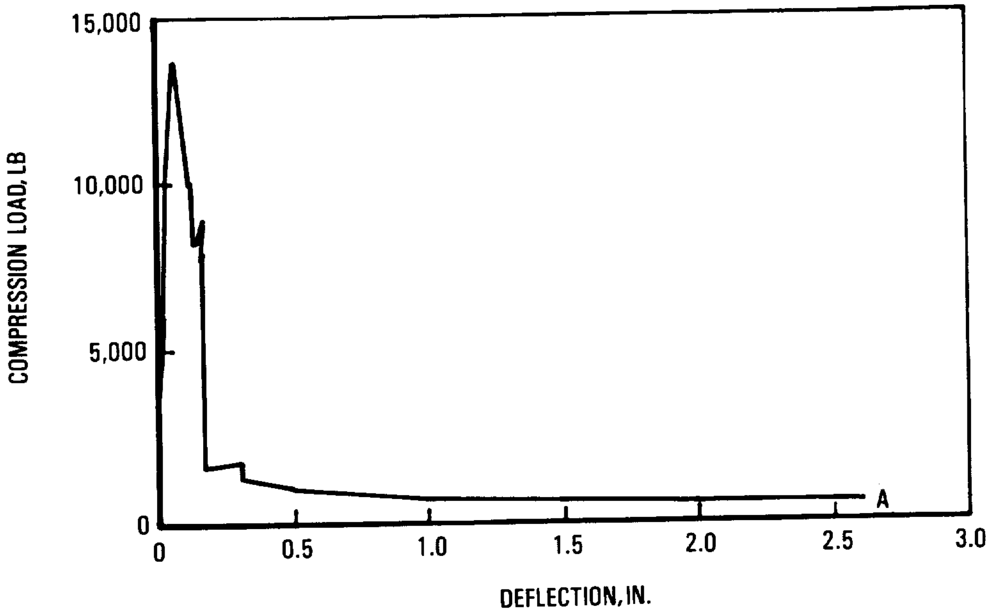

Figure 60. - Measured load versus deflection, blade-stiffened composite panel.

ORIGINAL PAGE
BLACK AND WHITE PHOTOGRAPH

4.1.4 Corrugated composite panel - The applied compression load increased at a relatively constant rate to a maximum of 29,150 pounds when the panel abruptly fractured across its total width and the load dropped to approximately 2000 pounds. The fracture occurred along a line approximtely one third of the distance between the loading heads. Following failure, the load remained relatively constant as the crushing deflection increased. The outer two or three corrugations on one side of the panel buckled while the fibers along the fracture line of the remaining corrugations were driven together in a brooming failure mode. The failed panel is shown in Figure 61. At the time the test was halted, the panel had crushed slightly over 2.7 inches. The load-deflection curve is shown in Figure 62.

4.1.5 Summary of panel static test results.- A comparison of the load-deflection and energy absorption of the four panels is shown in Table 11. The peak failure loads range from 13,650 to 15,680 pounds for the stiffened panels and as high as 29,150 pounds for the corrugated composite panel. The peak

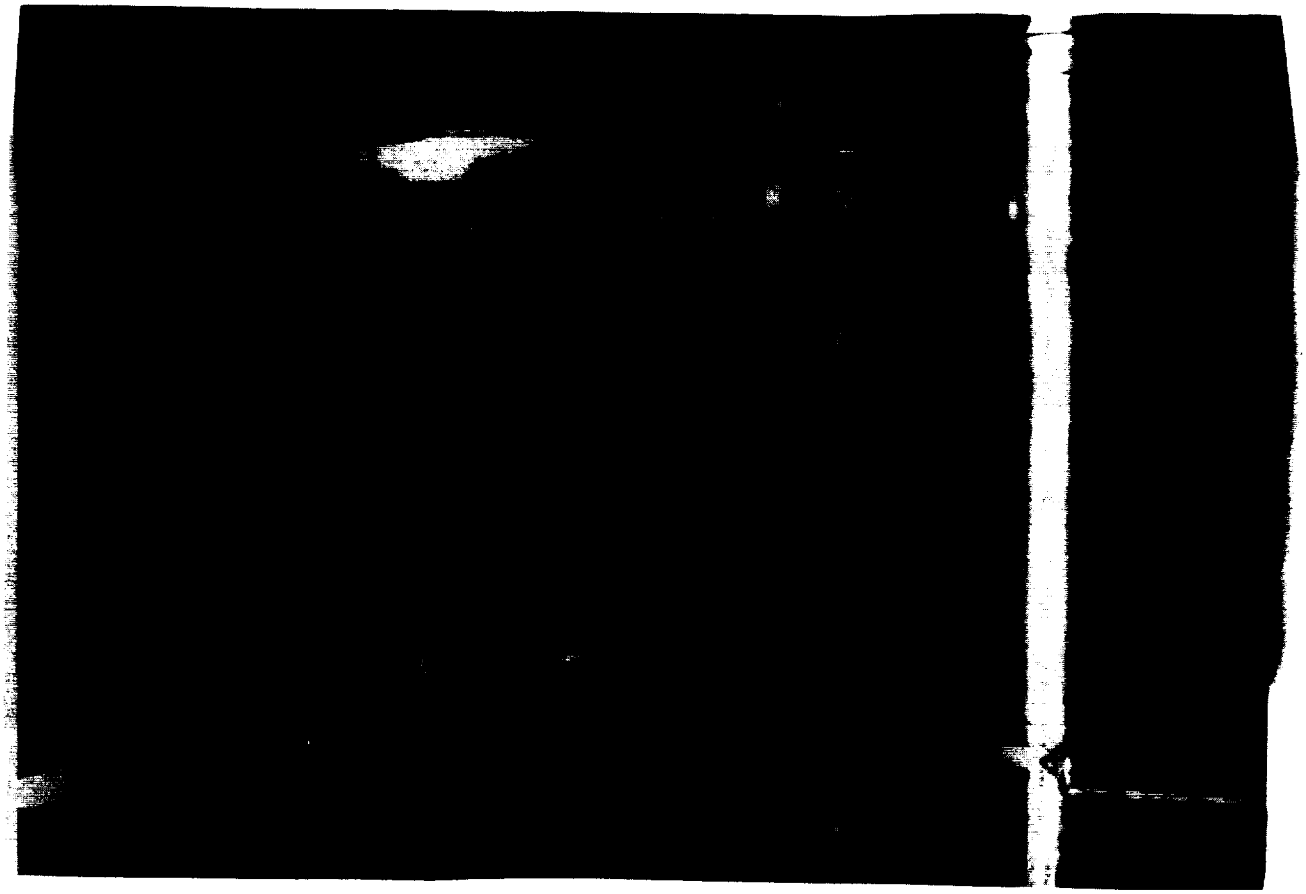

Figure 61. - Corrugated composite panel, failed specimen.

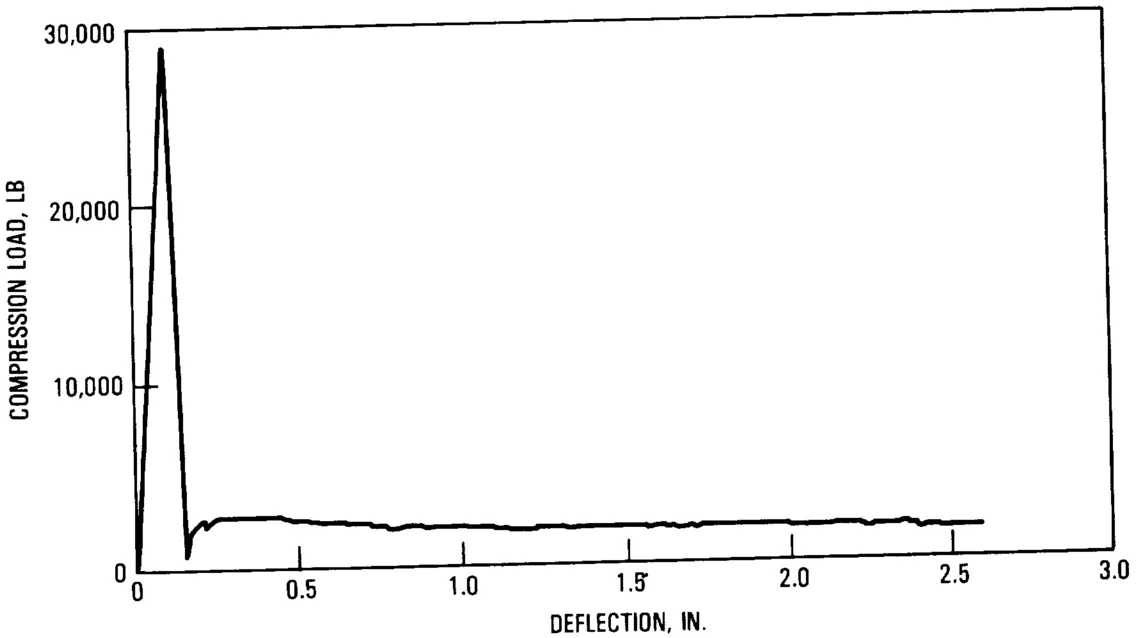

Figure 62. - Load versus deflection, corrugated composite panel.

TABLE 11. - COMPARISON OF STIFFENED PANEL TEST RESULTS

Stiffened Panel Configuration	Weight (lb.)	Peak Failure Load (lb.)	Deflection at Peak Failure Load (in.)	Energy @ Peak Load (in.-lb.)	Absorption @ 2 in. Deflection (in.-lb.)
Blade Stiffened Metal Panel	6.96	15680	0.10	1000	8300
Hat Stiffened Composite Panel	6.23	14820	0.10	500	3250
Blade Stiffened Composite Panel	5.92	13650	0.10	800	3100
Corrugated Composite Panel	2.17	29150	0.10	2600	6850

load levels for all four configurations occurred at relatively low crushing deflections (0.100 inch). The blade-stiffened metal panel exhibited the most energy absorption capability -- significantly more than the two stiffened composite configurations.

4.1.6 Analysis versus test.- The metal test panel was analyzed using the program LDCURVE which is described in Appendix A. The program estimates the width of the skin which remains effective in reacting the compression load after skin buckling. For an effective skin width of 3.6 inches, the resultant load deflection curves are shown in Figure 63 for a range of expotential factors. These factors govern the shape of the load deflection curve after peak load is achieved.

The predicted failure load determined by analysis is 21,000 pounds which is higher than the 15,680 pounds measured in the test. Two empirical parameters are used in determining this load. The first is associated with the edge constraints at the attachment of the test specimen to the test fixture. The second is an effective width parameter.

To generalize the LDCURVE program as much as possible, an edge fixity coefficient of 3 is built into the program. In most column analyses, a coefficient of 1 is used to represent a pinned end edge constraint while a

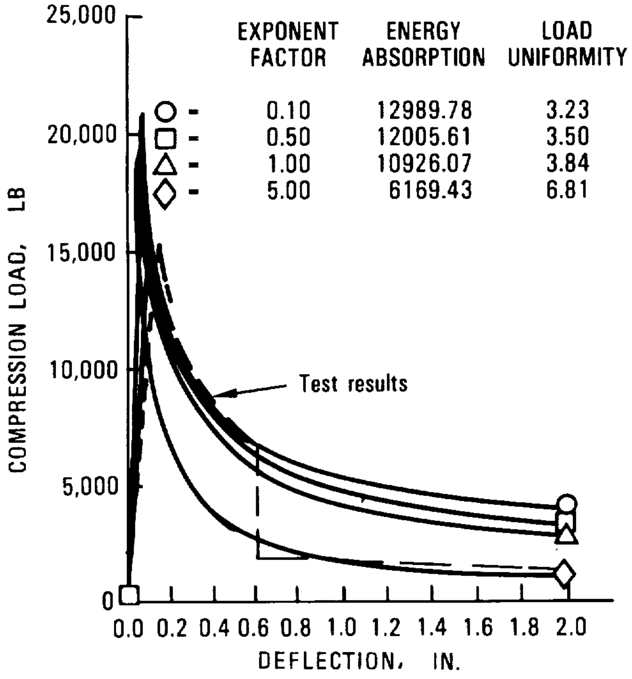

Figure 63. - Pre-tested predicted load deflection curve versus measured load deflection curve, blade-stiffened metal panel.

coefficient of 4 is used to represent a fixed end constraint. To demonstrate the sensitivity of the predicted load to the edge constraint coefficient, the specimen was analysed using an edge fixity coefficient of 1. The predicted failure load level was reduced only slightly to 20,000 pounds. Therefore, the predicted load level did not appear to be sensitive to this coefficient.

In the analysis, a linear relation exists between the effective skin width estimate and the failure load. For the test specimen, this relationship is illustrated in Figure 64. Entering the curve shown in the figure with the test failure load (15,680 pounds), an effective skin width of 1.9 inches is read. Thus, the test results imply that a skin width of 1.9 inches wide acts with each stiffener instead of an effective skin area 3.6 inches wide as predicted by the built-in effective width function. Thus, the effective skin width parameter is a significant factor and the analytical results are sensitive to its accurate prediction.

The stiffened panel was re-evaluated using an effective width of 1.9 inches. The resulting load deflection curves for a range of exponential factors are shown in Figure 65 along with the load deflection curve obtained in the test.

The energy absorption and the load uniformity ratio for each of the analytical load deflection curves shown in Figure 65 (3.6 inch effective skin width) and Figure 67 (1.9 inch effective skin width) are compared to experimental data in Table 12.

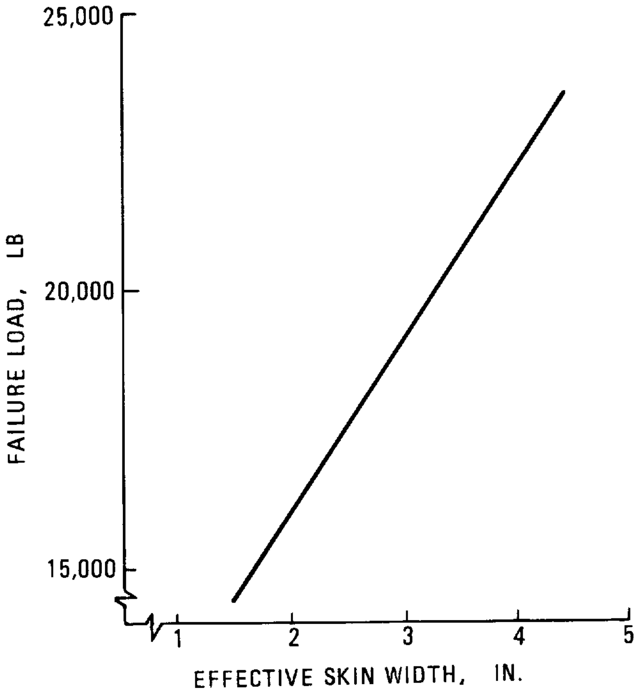

Figure 64. - Predicted failure load versus effective skin width.

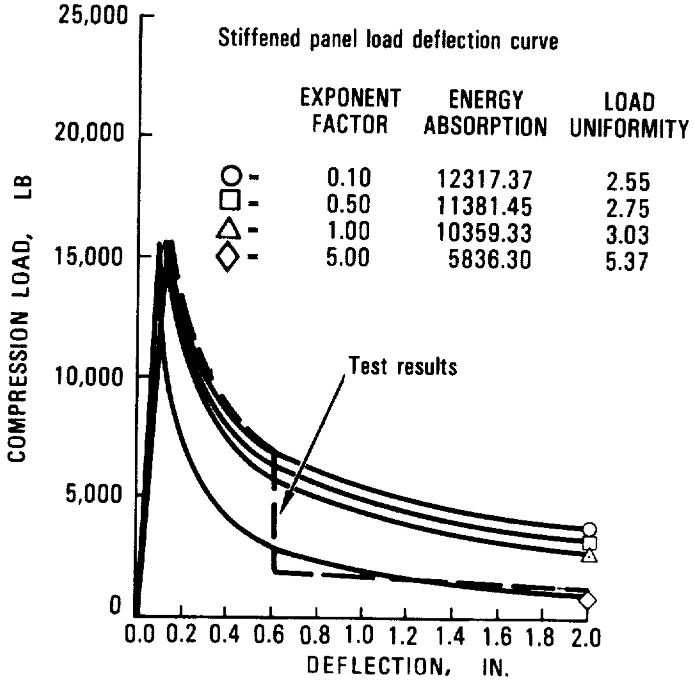

Figure 65. - Modified predicted load deflection curve versus measured load deflection curve, blade-stiffened metal panel.

TABLE 12. - ENERGY ABSORPTION PARAMETER SUMMARY, BLADE-STIFFENED METAL PANEL

Analysis Exponential Factor	Energy Absorption		Load Uniformity	
	Crushing Deflection (in.)			
	0.6	2.0	0.6	2.0
	1.9 (in.) Effective Skin Width			
0.1	5510	12320	1.71	2.55
0.5	5300	11380	1.77	2.75
1.0	5060	10360	1.86	3.03
5.0	3580	5840	2.63	5.37
	3.6 (in.) Effective Skin Width			
0.1	6180	12990	2.04	3.23
0.5	5930	12010	2.13	3.50
1.0	5630	10930	2.24	3.84
5.0	3910	6170	3.22	6.81
Test	5800	8200	1.65	3.90

In the 1.9 inch effective skin width analysis, the experimental results for a crushing deflection of 0.6 inch, show a reasonable match with the analytical results for exponential factors of 0.1 and 0.5. Comparing the experimental results and analytical results for a crushing deflection of two inches demonstrates the effects of the discontinuity in the experimental load deflection curve due to the rupture of the stiffener blades. At large deflections, the analysis substantially over predicts the energy absorption.

The stiffened composite panels failed in a stiffener separation mode not accounted for in the LDCURVE program. Therefore, no attempt was made to calculate load deflection curves for the composite panels.

4.2 Modified Composite Panel Static Tests

The unmodified test panels all exhibited undesirable failure modes and low energy absorption capability. None of the composite panels demonstrated the crushing failure necessary for efficient energy absorption. This section describes the tests of specimens which were modified to initiate crushing. The modifications, based on techniques reported in References 9 and 10, involved using chamfered skins and stiffeners to promote crushing and using brackets to attach chamfered panels to cap structure. Figure 66 shows the applications of these design features to the hat-stiffened panel. Other panels were modified in a similar manner.

4.2.1 Chamfered corrugated composite panels

4.2.1.1 Short panel. - The previously tested corrugated composite panel was salvaged and used to produce two short corrugated panels. One short panel was tested statically and the other was tested dynamically. The salvaged panel was cut as shown in Figure 67. One end of each panel was chamfered and the other potted into a base for stability during the tests.

A crushing deflection was applied at a rate of 0.08 in/min for the first 120 seconds of the test. The deflection rate was increased gradually to 2.4 in/min during the last 30 seconds of the test. The applied compression load increased at a relatively constant rate to a maximum of 7,300 pounds, after which it dropped to 4400 pounds. The load then increased to approximately 6000 pounds and remained relatively constant through the remainder of the test. The failure mode was brooming in which the chamfer initiated failures between the layers of the composite material. The failed panel is shown in Figure 68. When the test was halted, the panel had crushed slightly over 2.4 inches. The load-deflection curve is shown in Figure 69.

4.2.1.2 Long Panel. - The composite corrugated panel, originally intended for dynamic testing, was cut in half and the flanges removed to form two corrugated panels as shown in Figure 70. Both the panels were chamfered

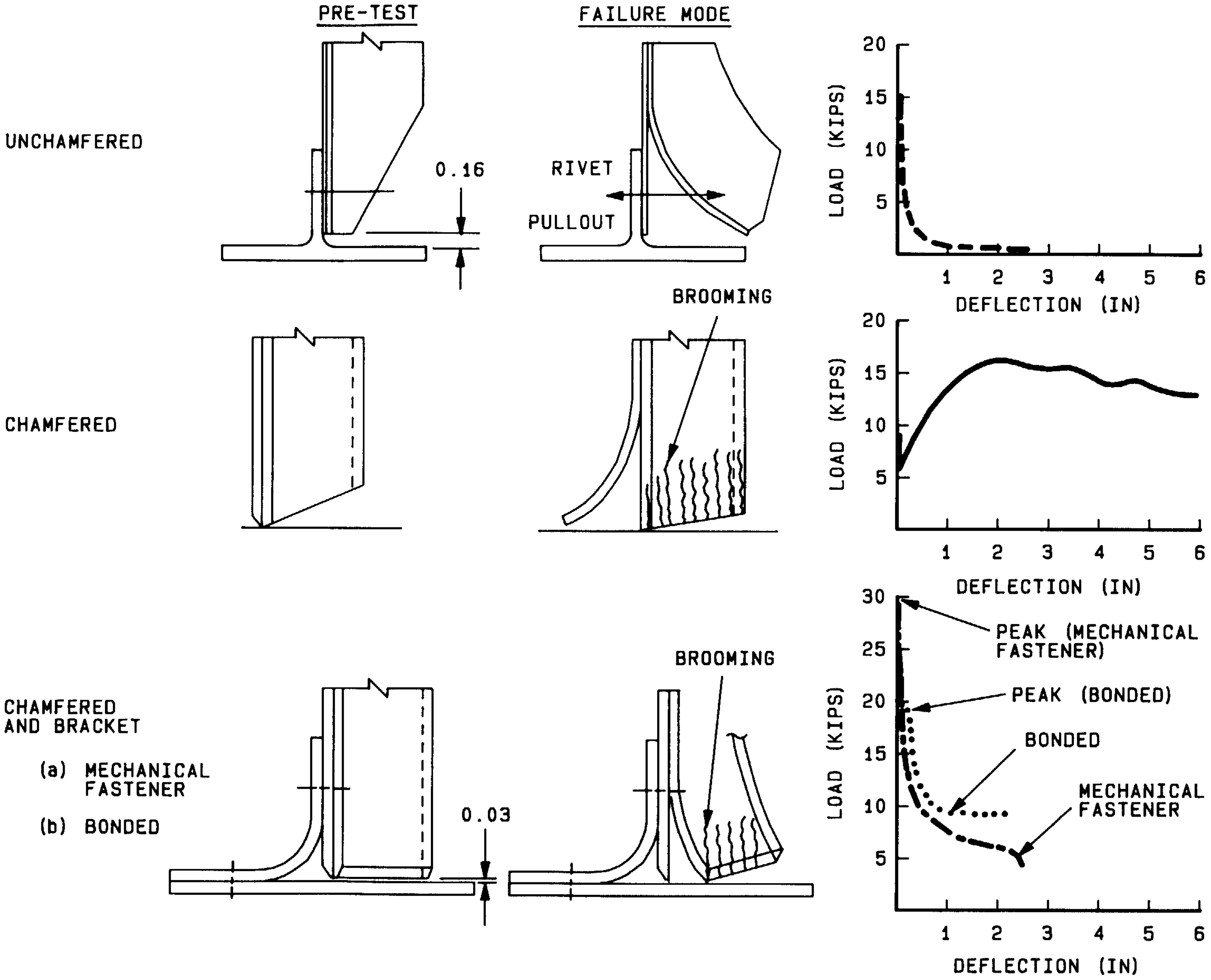

Figure 66. - Hat-stiffened panel test configurations, failure modes and load-deflection curves.

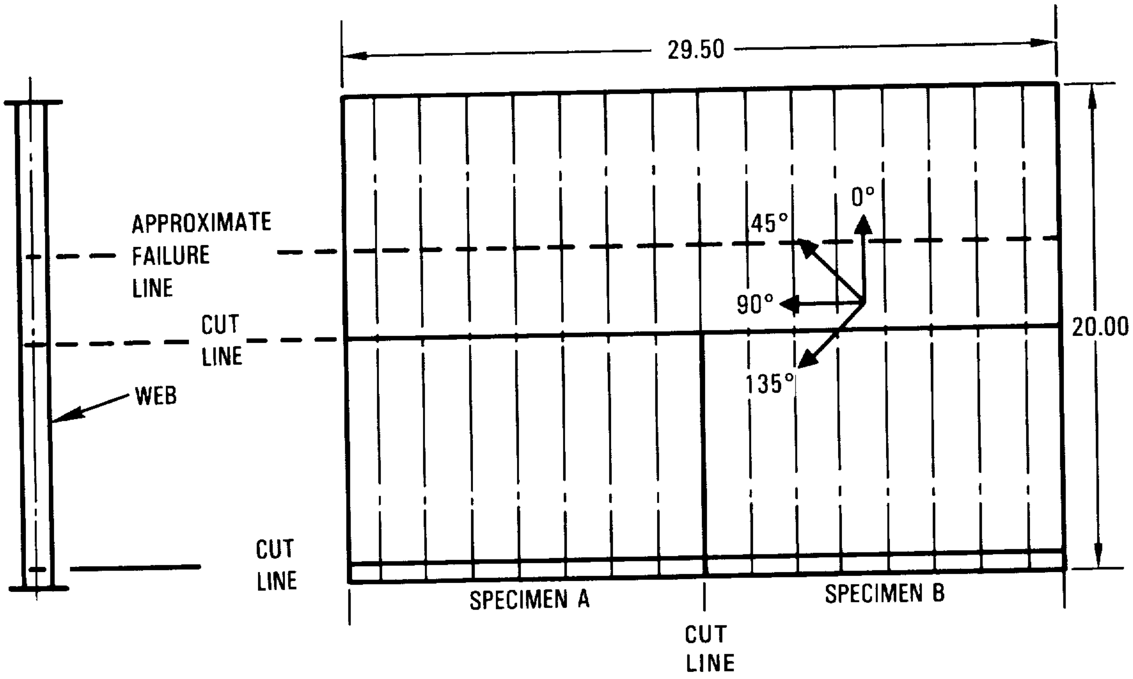

Figure 67. - Short corrugated composite panel salvaged from composite panel concept #2.

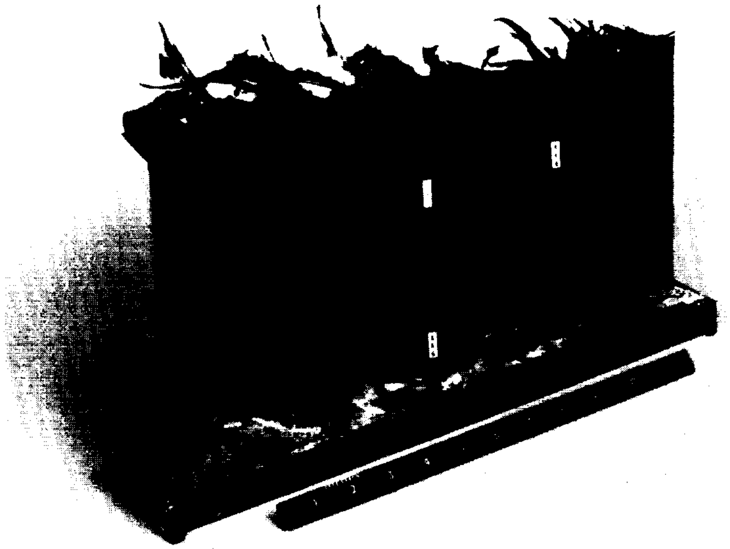

Figure 68. - Short corrugated composite panel, failed specimen.

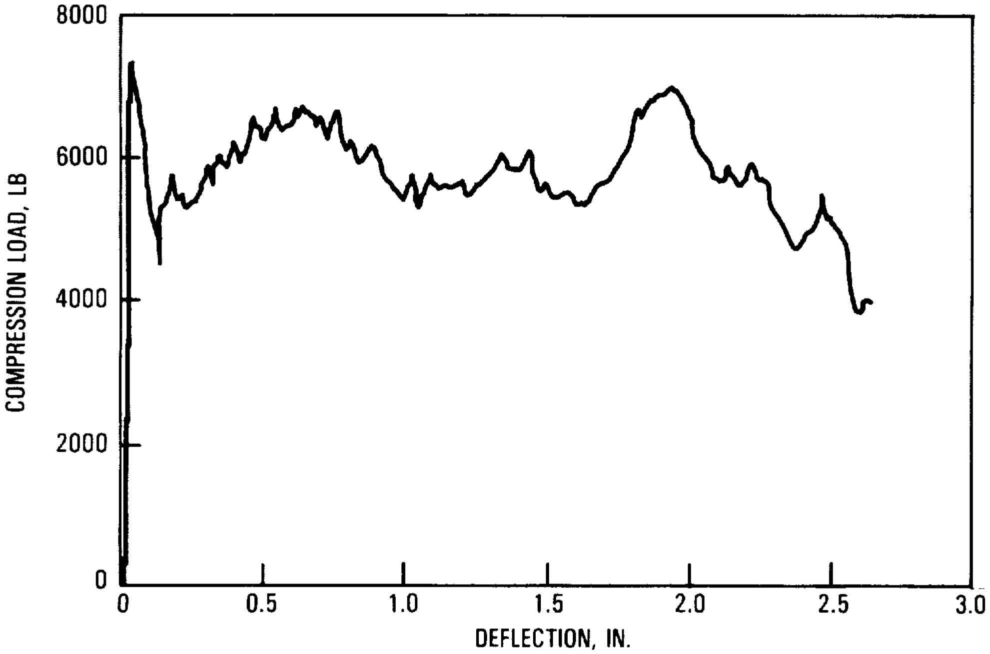

Figure 69. - Load versus deflection, short corrugated composite panel.

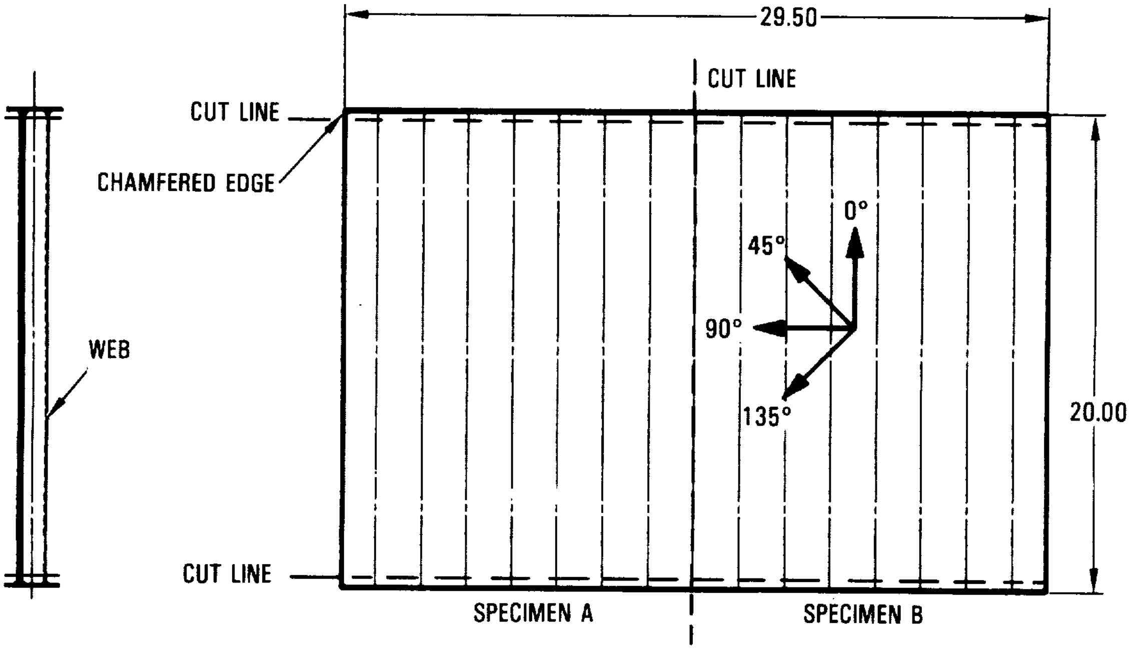

Figure 70. - Long corrugated composite panel design.

on one end and the other end of each was potted into a mounting frame. One of the panels was tested statically and the other was tested dynamically.

A crushing deflection was applied at a rate of 0.08 in/min for the first 120 seconds of the test. The applied deflection rate was increased in two steps to 3.0 in/min during the last 90 seconds of the test. The applied compression load increased at a relatively constant rate to a maximum of 7297 pounds. The load then dropped to approximately 4800 pounds, then increased to approximately 6000 pounds and then varied around 5300 pounds for the remainder of the test. The failure mode was similar to that of the short corrugated panel. The failed panel is shown in Figure 71. When the test was halted, the panel had crushed approximately 6 inches. The load versus deflection curve is shown in Figure 72.

4.2.2 Chamfered hat-stiffened composite panel. - The hat-stiffened composite panel originally intended for dynamic testing was modified by removing the attachment flanges along the loading ends as shown in Figure 73. The top end of the panel was chamfered and the other end potted into a mounting frame.

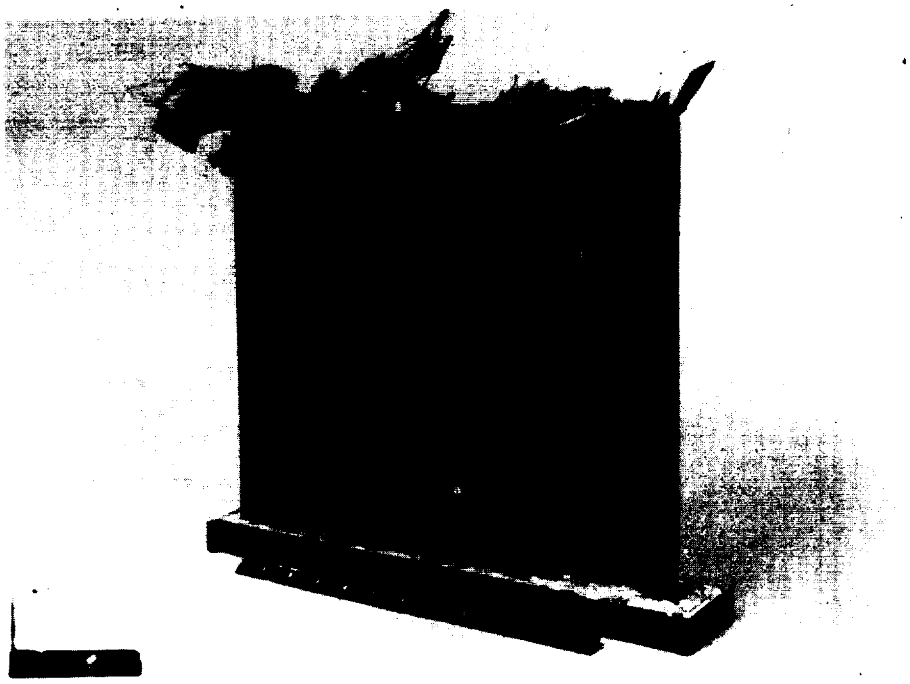

Figure 71. - Long corrugated composite panel, failed specimen.

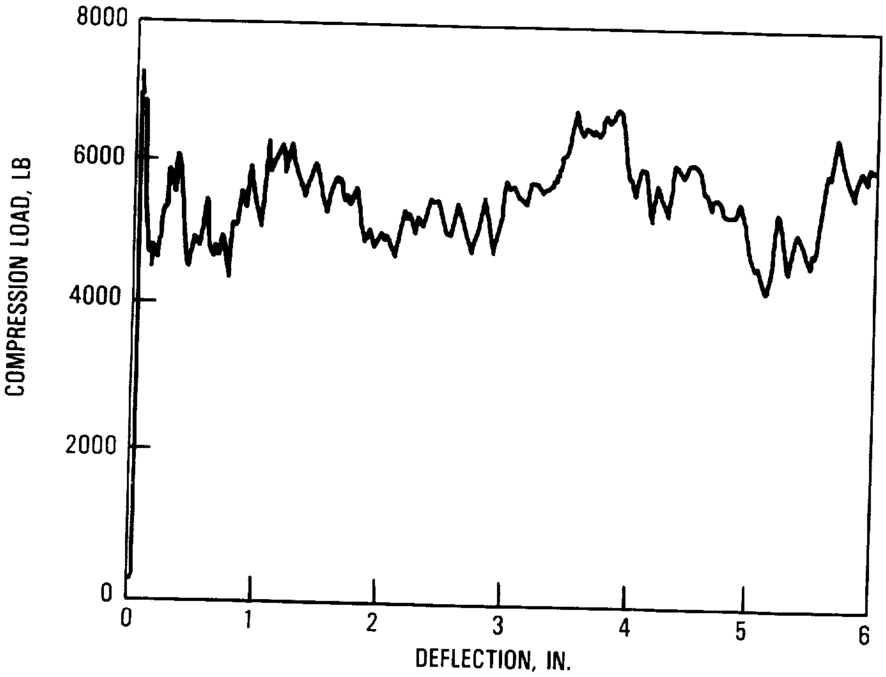

Figure 72. - Load versus deflection, long corrugated composite panel.

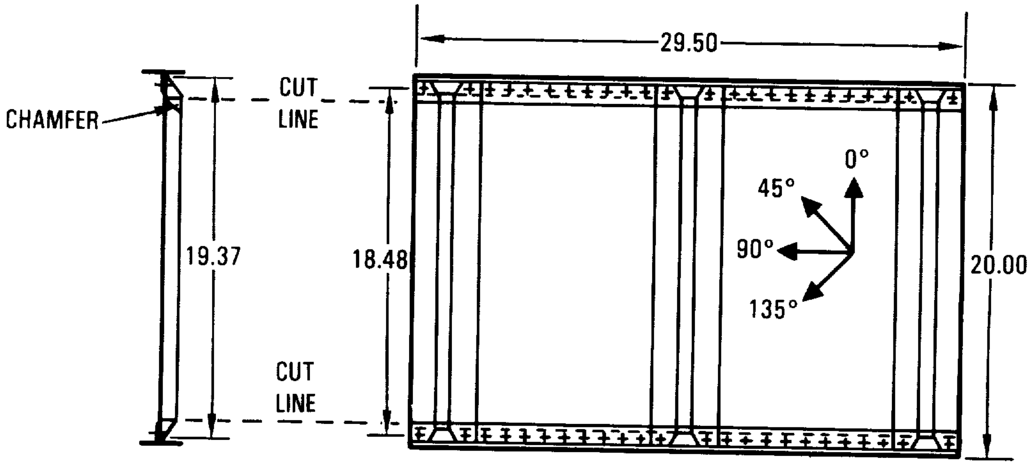

Figure 73. - Hat-stiffened chamfered composite panel cut lines.

A crushing deflection was applied at a rate of 0.03 in/min for the first 120 seconds of the test. The loading rate was increased in two steps to 3.1 in/min during the last 80 seconds of the test. The total test time was approximately 430 seconds. The applied compression load increased at a relatively constant rate to approximately 850 pounds at 90 seconds. The load dropped, then increased and then dropped again as the center and then the end stiffeners began to peel from the skin. As the deflection increased, the loading head pushed the skin to one side and the stiffeners carried all of the applied load. The load increased to a maximum of 17,150 pounds at 340-seconds and remained relatively constant at around 15,000 pounds for the remainder of the test.

Immediately following the separation of the stiffeners and skin, the chamfered ends of the stiffeners initiated a brooming failure. The failed panel is shown in Figure 74. When the test was halted, the panel had crushed approximately 6 inches. The load-deflection curve is shown in Figure 75.

4.2.3 Chamfered hat-stiffened composite panel with composite bracket attachments. - The validity of the chamfer as a "crush initiation" design concept was demonstrated in the tests of the modified hat-stiffened panel and the modified corrugated panels. Neither of these specimen designs, however, accounted for a practical attachment method. The corrugated column shows potential from an efficiency standpoint, but presents a formidable installation problem.

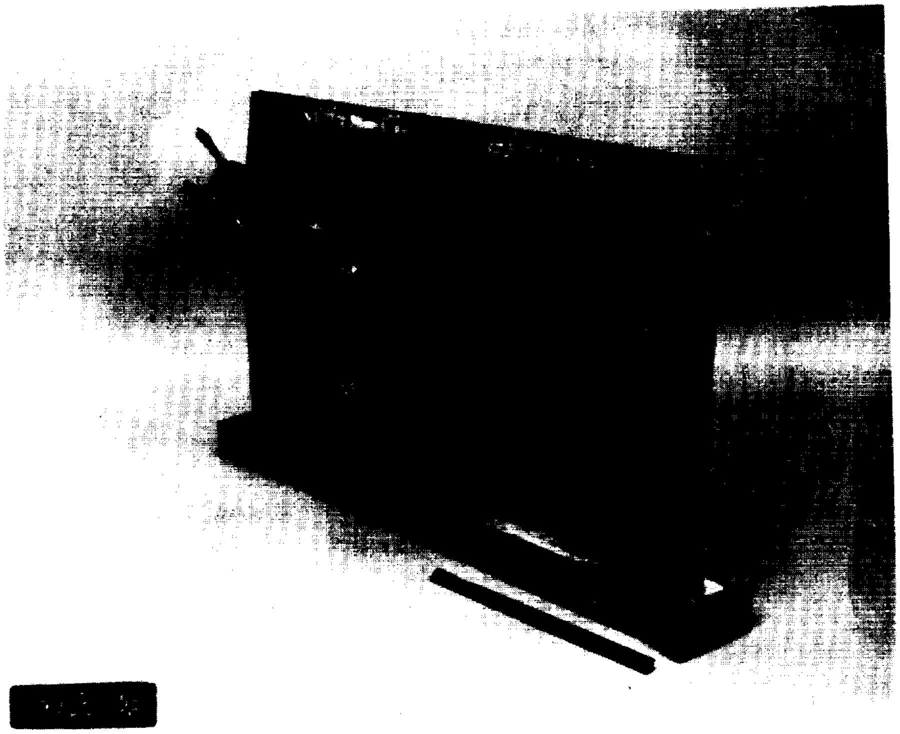

Figure 74. - Chamfered hat-stiffened composite panel failed specimen - stiffener side.

Figure 75. - Load versus deflection, chamfered hat-stiffened composite panel.

The hat-stiffened panel was chosen to demonstrate a practical method of attachment. Angle brackets, fabricated from composite material, were chosen for the attachment design in this study. The brackets were designed to act as a fuse that would fail at a specified load. After failure, the crushing load would be transferred to the chamfered edge of the hat-stiffeners thus initiating the desired failure mode.

Three bracket designs were fabricated, each with a layup of $[45/0/135/0/135/45/90]_S$ for a total of 13 plies. Radii of 0.25, 0.50 and 0.75 inches were used. The test results are presented in Table 13 and the specimens are shown in Figure 76. The 0.25 inch radius was selected for use in test panels.

ORIGINAL PAGE IS
OF POOR QUALITY

TABLE 13. - BRACKET TEST RESULTS

Bracket Specimen	Approx. Failure Load (lb)	Approx. Post-Failure Sustained Load (lb)	Deflection at Failure (in)
1/4 R	215	150	0.16
1/2 R	185	130	0.28
3/4 R	175	125 (increasing)	0.66

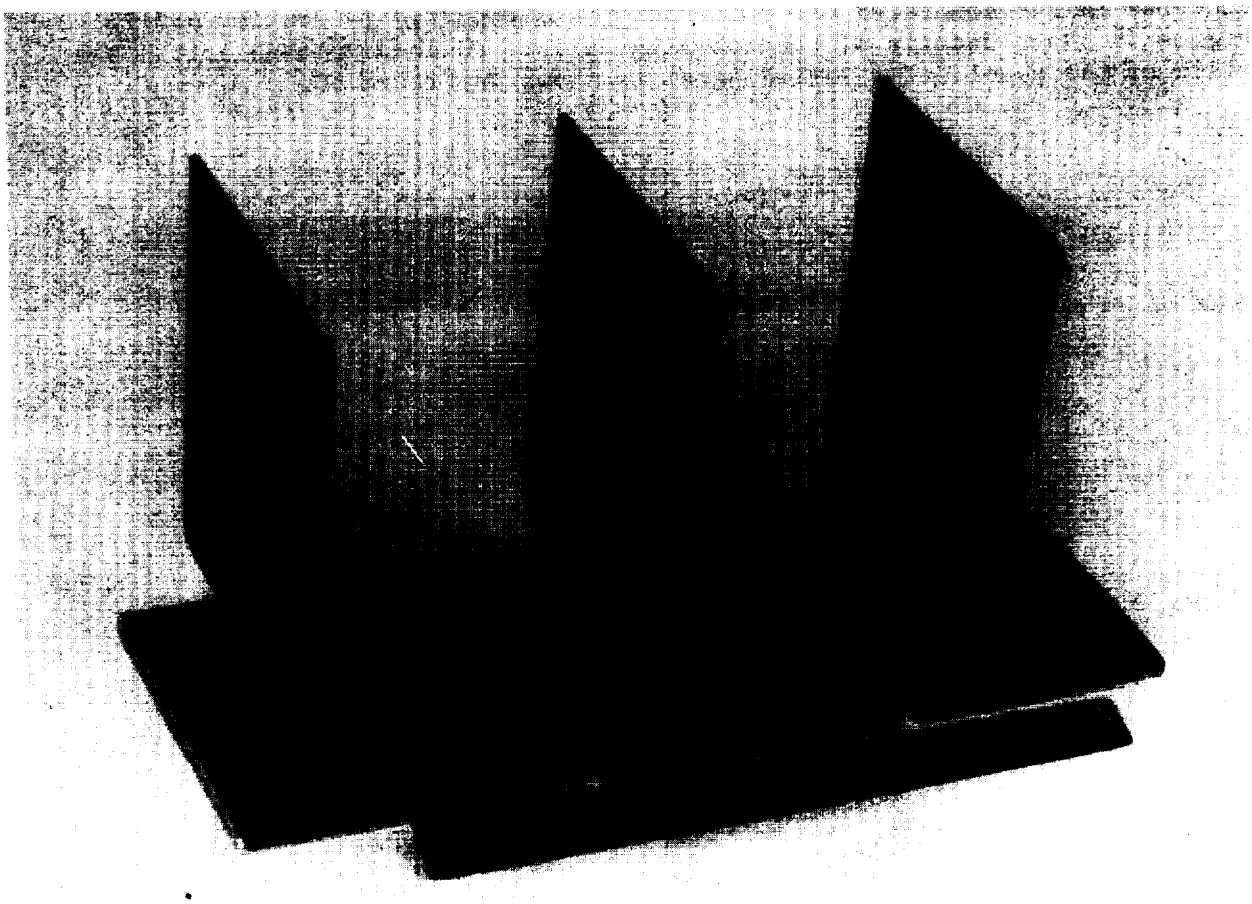

Figure 76. - Bracket test specimens.

ORIGINAL PAGE
BLACK AND WHITE PHOTOGRAPH

The hat-stiffened composite design discussed in section 4.1.2 was modified by chamfering the ends of the hat-stiffeners and skin and by replacing the aluminum T-section attachments with composite angle brackets, Figure 77.

A crushing deflection was applied at a rate of approximately 0.036 in/min for the first 230 seconds of the test and then increased to approximately 3.67 in/min during the last minute. The load reached a maximum of 28,650 pounds at a deflection of 0.11 inches. The load then dropped rapidly to approximately 8000 pounds. Thereafter, it decreased slowly until the test was terminated at a crushing deflection of about 2.5 inches and a load of 6000 pounds. The load deflection curve is shown in Figure 78.

As the panel was loaded, the leg of the composite bracket attached to the skin rotated to allow direct loading of the stiffeners and skin. The brooming failure of the stiffeners was initiated. As the crushing deflection increased the panel buckled but since the brackets held the skin in position, the stiffeners were pulled from the skin and moved to one side as shown in Figure 66. Brooming of the stiffeners continued but to a much lesser extent then had occurred in the chamfered hat-stiffened panel reported in section 4.2.2. Figure 79 shows details of the brooming failure which developed across the width of the panel. The failed panel is shown in Figure 80.

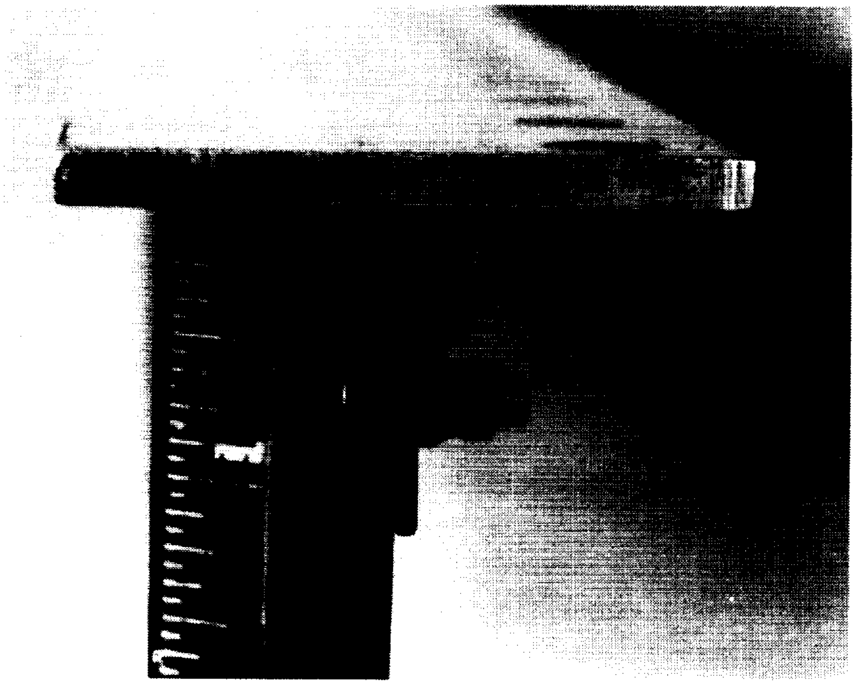

Figure 77. - Composite angle bracket attachment.

~~ORIGINAL PAGE IS~~
~~OF POOR QUALITY~~

ORIGINAL PAGE
BLACK AND WHITE PHOTOGRAPH

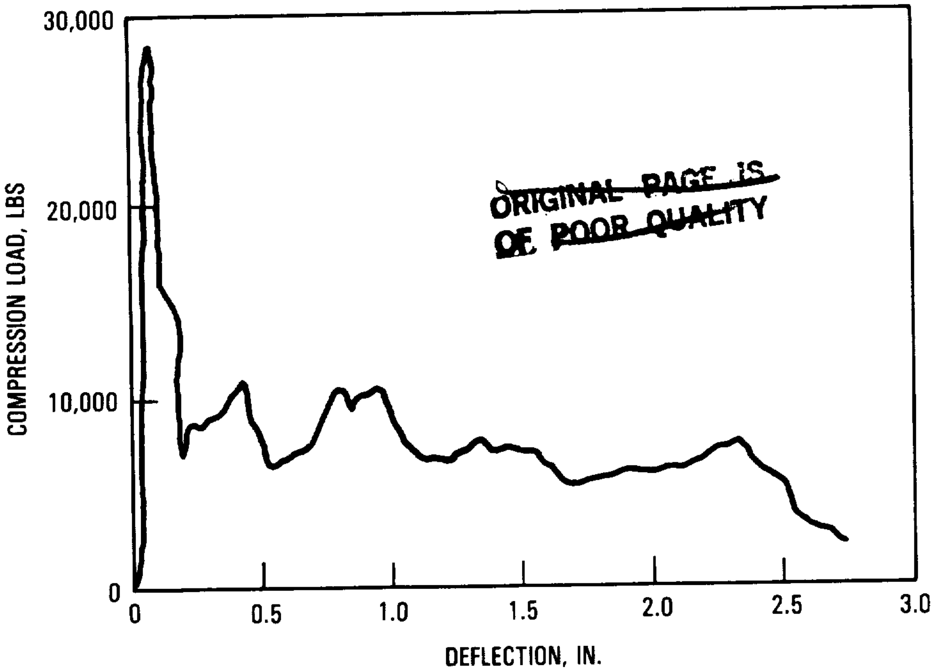

Figure 78. - Hat-stiffened composite panel/composite bracket load versus deflection curve.

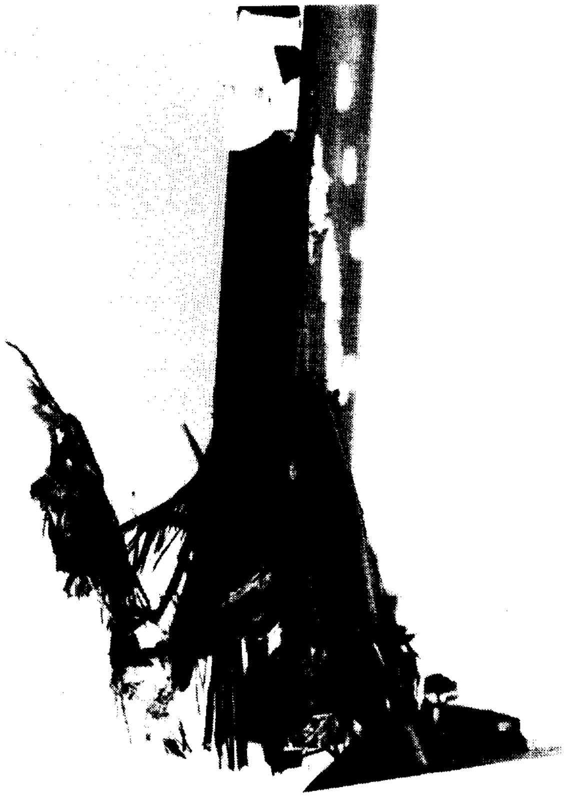

Figure 79. - Hat-stiffened composite panel/composite bracket brooming failure detail.

~~ORIGINAL PAGE IS OF POOR QUALITY~~

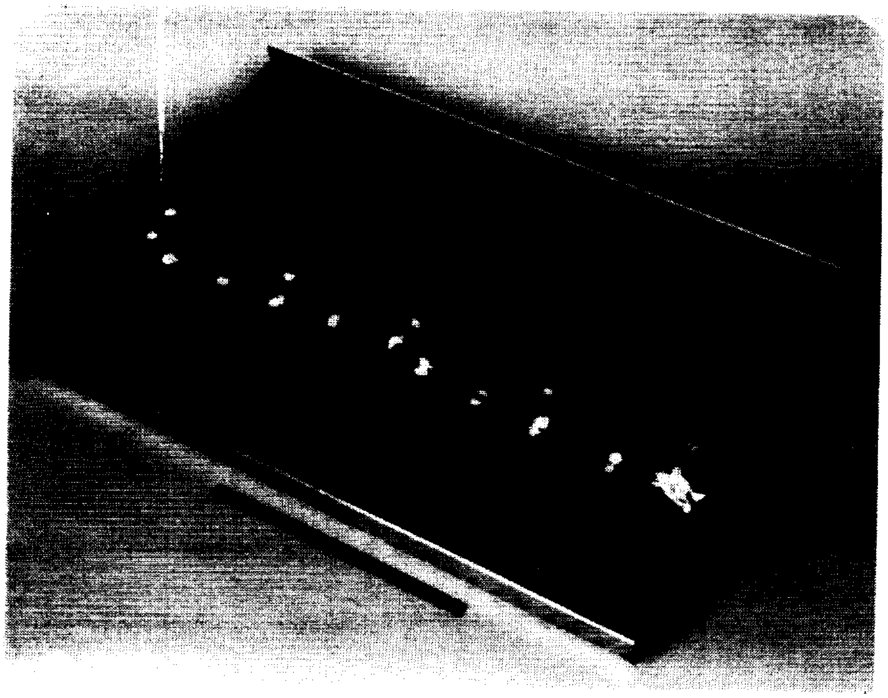

Figure 80. - Hat-stiffenced composite panel/composite bracket post-failure specimen.

4.2.4 Summary of modified composite panel static test results. - The static test results for the modified composite panels described in Sections 4.2.1, 4.2.2 and 4.2.3 are shown in Tables 14 and 15 for crushing deflections of 2.0 inches and 6.0 inches, respectively. The energy absorption for each panel was obtained by integrating the area under the respective load-deflection curves.

All the modified panels showed improved energy absorption. The modified panels without the angle bracket attachment exhibited load uniformity ratios between 1.25 and 1.46. The results for the long and short corrugated panels were comparable. The hat-stiffened panels exhibited higher loads and energy absorption, but because they weigh more the specific energy is substantially lower than for the corrugated panels. The panel with a mechanically fastened angle bracket, while an improvement compared to the unmodified composite hat-stiffened panel (sections 4.1.3 and 4.1.5), nonetheless was not as efficient as the chamfered-only modification.

4.3 Modified Composite Panel Dynamic Tests

4.3.1 Chamfered corrugated panels. - The short and long corrugated panels described in Section 4.2.1 were dynamically tested. The test panels were mounted in a drop test machine as shown in Figure 81.

ORIGINAL PAGE
BLACK AND WHITE PHOTOGRAPH

TABLE 14. STATIC TEST RESULTS, MODIFIED COMPOSITE PANELS AT 2 INCH CRUSHING DEFLECTION

Test Specimen	Specimen Weight (lb)	Maximum Load (lb)	Average Load (lb)	Energy Absorption (in-lb)	Specific Energy Absorption (in-lb/lb)	Load Uniformity Ratio
Blade Stiffened Metal Panel	6.96	15,680	4,150	8,300	1,190	3.80
Short Corrugated Panel	0.40	7,300	5850	11,700	29,100	1.25
Long Corrugated Panel	0.75	7,297	5300	10,600	14,100	1.38
Hat Stiffened Panel	4.50	17,150	11750	23,500	5,200	1.46
Hat Stiffened Panel + Angle Bracket	6.2	28,650	8400	16,800	2,710	3.50

TABLE 15. STATIC TEST RESULTS, MODIFIED COMPOSITE PANELS AT 6 INCH CRUSHING DEFLECTION

Test Specimen	Specimen Weight (lb)	Maximum Load (lb)	Average Load (lb)	Energy Absorption (in - lb)	Specific Energy Absorption (in - lb/lb)	Load Uniformity Ratio
Long Corrugated Panel	0.75	7297	5500	33000	44,000	1.33
Hat Stiffened Panel	4.50	17150	13500	81000	18,000	1.27

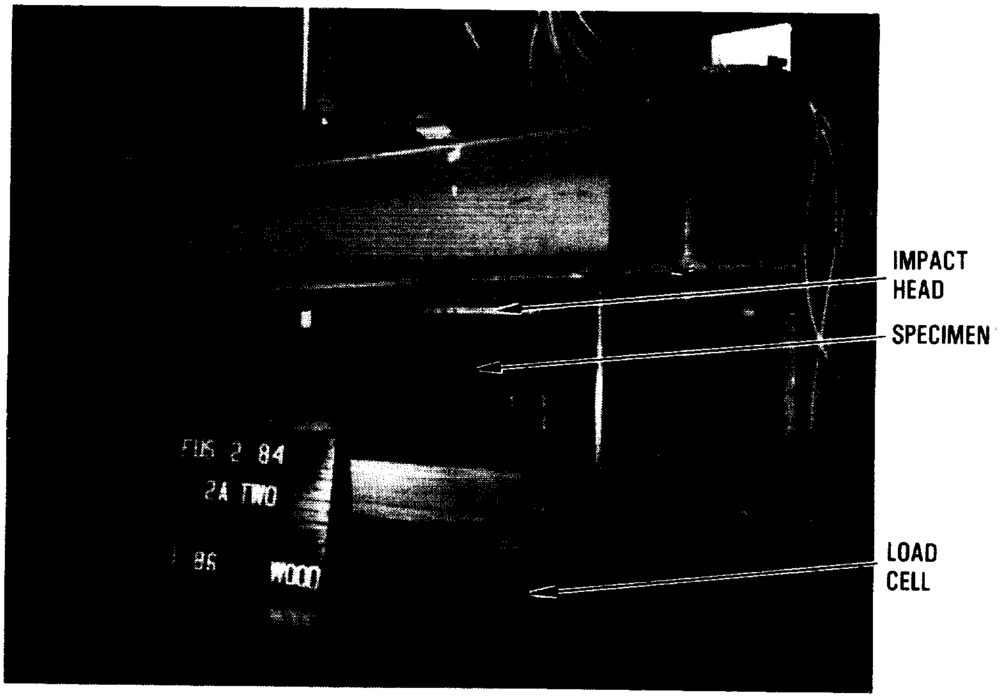

Figure 81. - Short corrugated composite column pre-dynamic test arrangement.

A free falling mass weighing 720 pounds was dropped on each of the panels. The mass was dropped from a height of 18.7 inches (impact velocity of 10 ft/sec) onto the short panel and from a height of 4.7 inches (impact velocity of 5 ft/sec) onto the long panel. In both cases, the panels failed as in the static test of the corrugated panel without chamfered ends, see Section 4.1.4. A post-test inspection of the test setup revealed that the impact surface of the free falling mass was a hard rubber pad. This hard rubber surface deflected under the chamfered edge and thus negated the crush initiation anticipated.

The long corrugated panel was salvaged and the failed end removed, thus reducing the panel height to 14 inches. The new free edge of the panel was chamfered. The rubber impact surface of the free falling mass was replaced with a steel plate and the dynamic test was repeated.

Four load cells and a deflection transducer were used to measure the force exerted on the panel and the travel of the mass after impact with the panel. The load-deflection curve is shown in Figure 82.

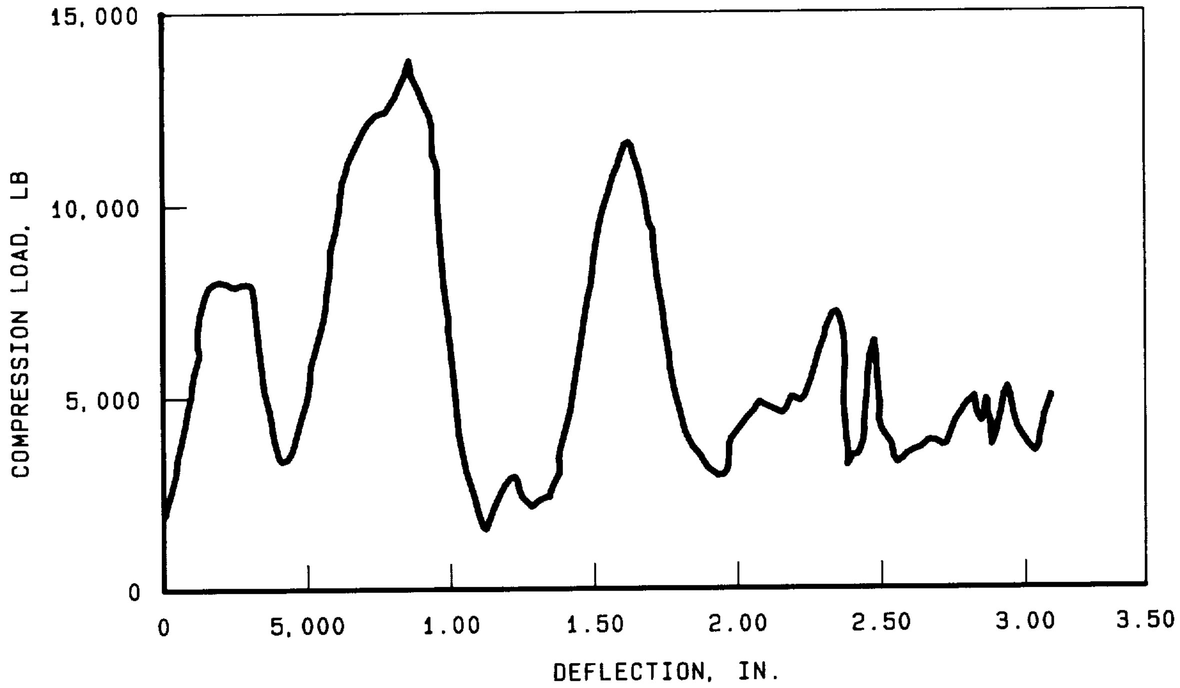

Figure 82. - Corrugated composite panel load versus deflection curve - impact velocity 10 ft/sec.

After initial impact, the panel deflected 0.85 inches as the load built up to a peak of 14,110 pounds. A total crush of approximately 3.2 inches was achieved. Based on static test results and the energy involved, this crush distance was anticipated. After reaching its peak the load oscillated about a mean of 5000 pounds. The failure mode, see Figure 83, was brooming in which the chamfer initiated failures between layers of the composite material similar to the static tests described in Section 4.2.1.

Again the panel was salvaged by cutting off the failed end reducing the height to 10 inches. The panel was mounted in the dynamic test fixture as before. A free falling mass weighing 528 pounds was dropped from a height to produce a 13.9 ft/sec impact velocity. The load-deflection curve is shown in Figure 84.

After initial impact, the free falling mass crushed the panel 0.9 inches as the load built up to a level of 14,750 pounds. The load then dropped to an average level of about 5000 pounds where it remained constant through a deflection of 3.2 inches. The failure mode was brooming, similar to that displayed in other corrugated composite panels with chamfered ends, see Figure 85.

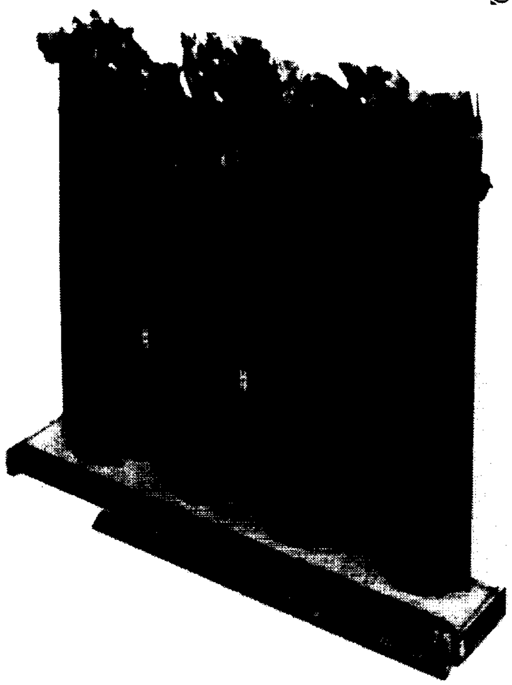

Figure 83. - Failed corrugated composite dynamic test specimen - impact velocity 10 ft/sec.

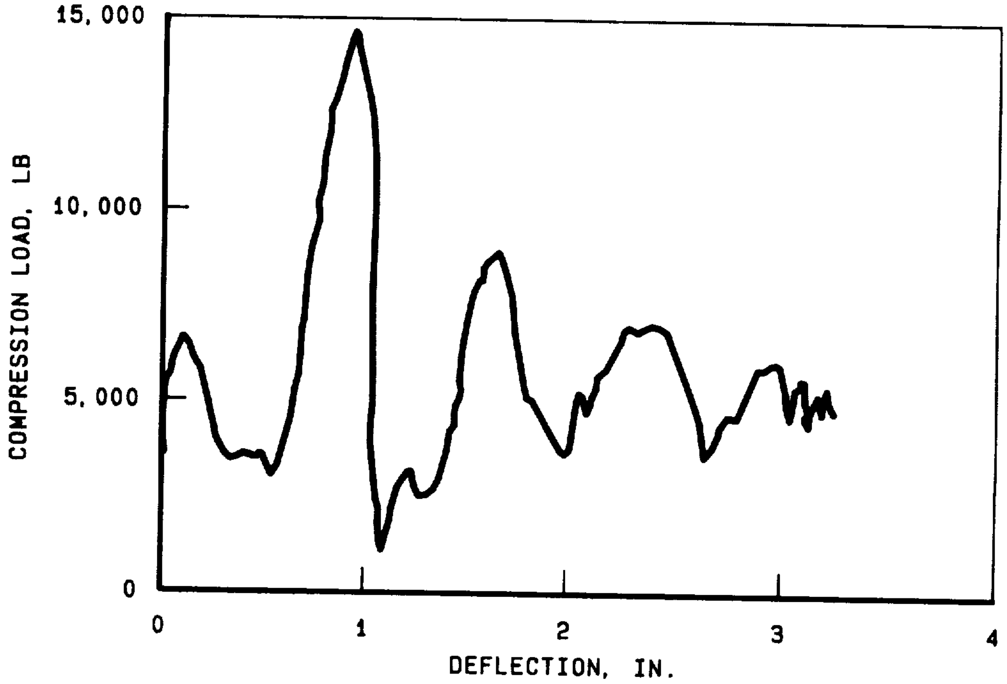

Figure 84. - Corrugated composite panel load versus deflection curve - impact velocity 13.9 ft/sec.

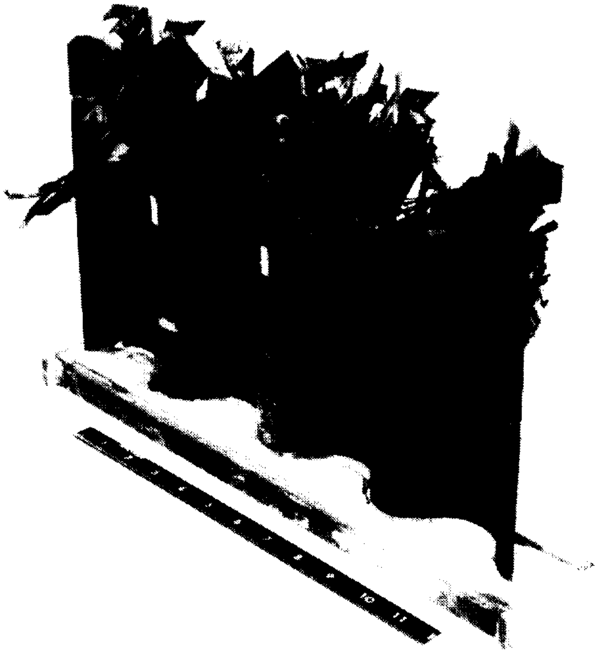

Figure 85. - Failed corrugated composite dynamics test specimen - impact velocity 13.9 ft/sec.

4.3.2 Chamfered hat-stiffened panels with mechanically fastened attachment brackets. - A hat-stiffened panel with composite attachment brackets similar to the panel described in Section 4.2.3 as shown in Figure 80 was dynamically tested. The static test panel was 29.5 inches wide and consisted of three hat-stiffeners and two bays while the dynamic test panel was 18.25 inches wide and consisted of two hat-stiffeners and a single bay.

A free falling mass weighing 528 pounds was dropped onto the panel from a height which produced an impact velocity of 11 ft/sec. The load-deflection curve is shown in Figure 86.

Following impact, the panel deflected 2.4 inches as the load built up to 26,500 pounds. The deflection then returned to approximately 1.5 inches where it remained through the duration of the test. The failure mode was very similar to that exhibited by the static test panel, see Section 4.2.3. Figure 87 shows details of brooming failure along the edge of the panel. Figure 88 shows the overall failure mode of the panel.

Since brooming failure occurred at one end it was possible to salvage the panel by removing the failed end and attachment brackets and potting it into a test frame. The undamaged end still had a mechanically fastened attachment bracket. The test panel was mounted in the test fixture again and a free falling mass weighing 528 pounds was dropped onto the panel end with the attachment bracket, from a height which produced an impact velocity of 13 ft/sec. The load-deflection curve resulting from these histories is shown in Figure 89.

C-2

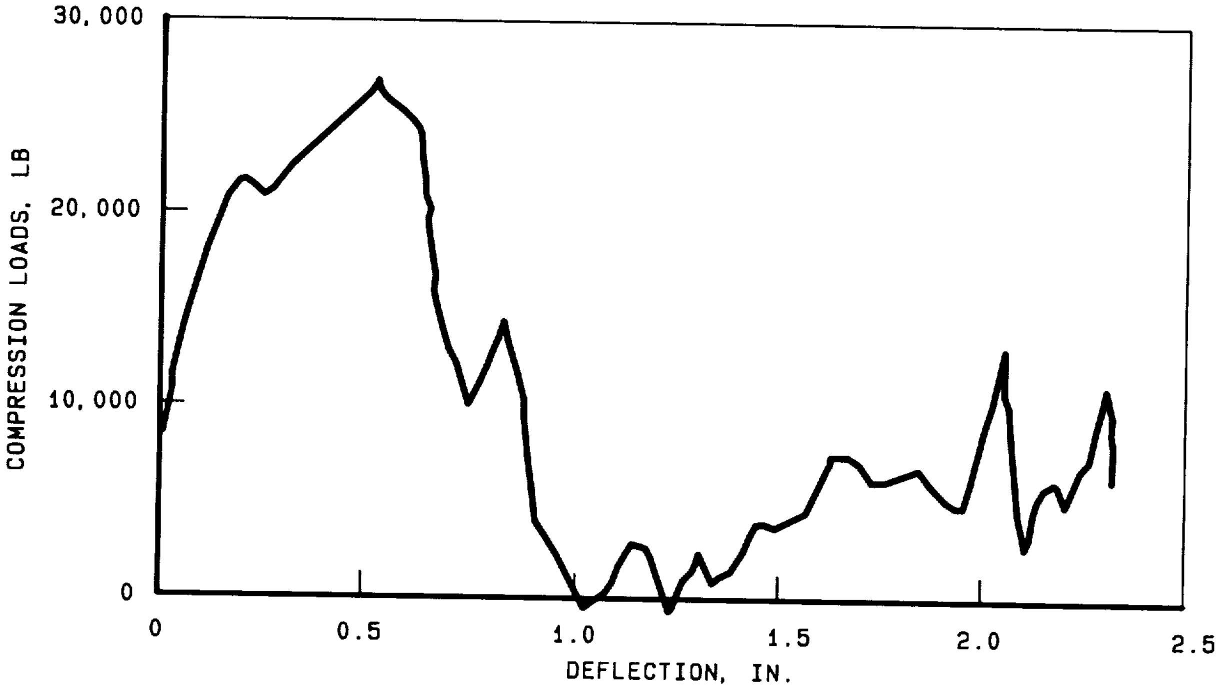

Figure 86. - Hat-stiffened composite panel/composite bracket load versus delection - impact velocity 11 ft/sec.

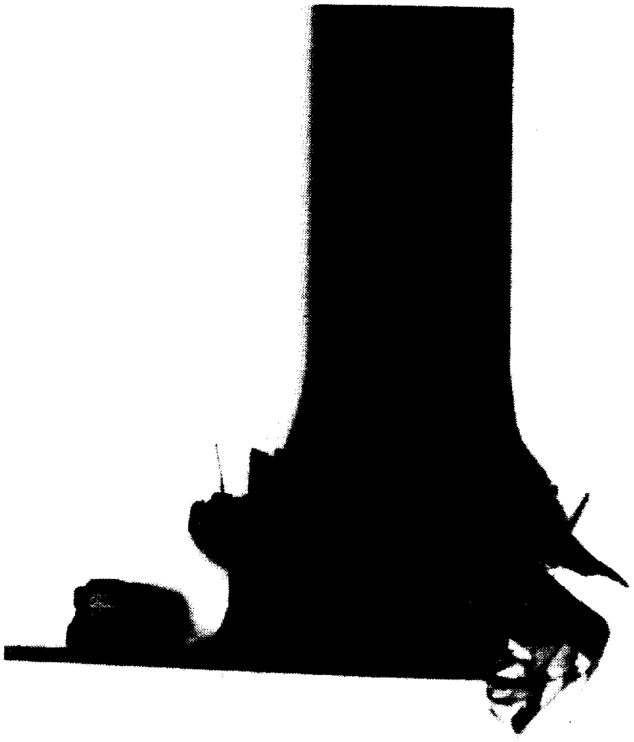

Figure 87. - Hat-stiffened composite panel/composite bracket brooming failure details - impact velocity 11 ft/sec.

ORIGINAL PAGE IS
OF POOR QUALITY

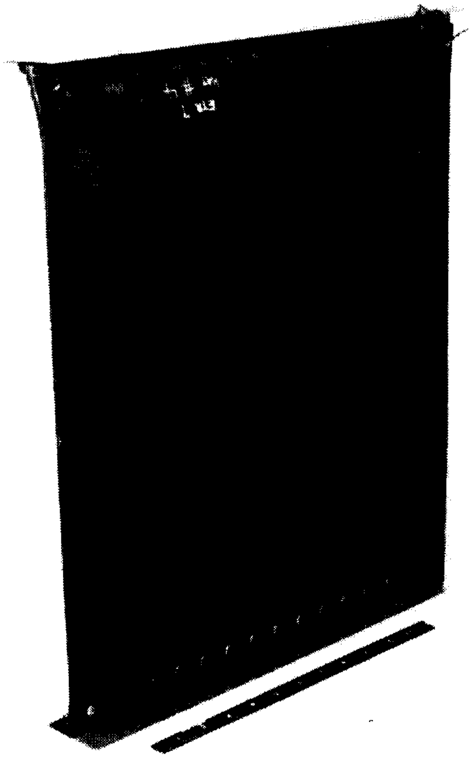

Figure 88. - Hat-stiffened composite panel/composite bracket post-failure specimens - impact velocity 11 ft/sec.

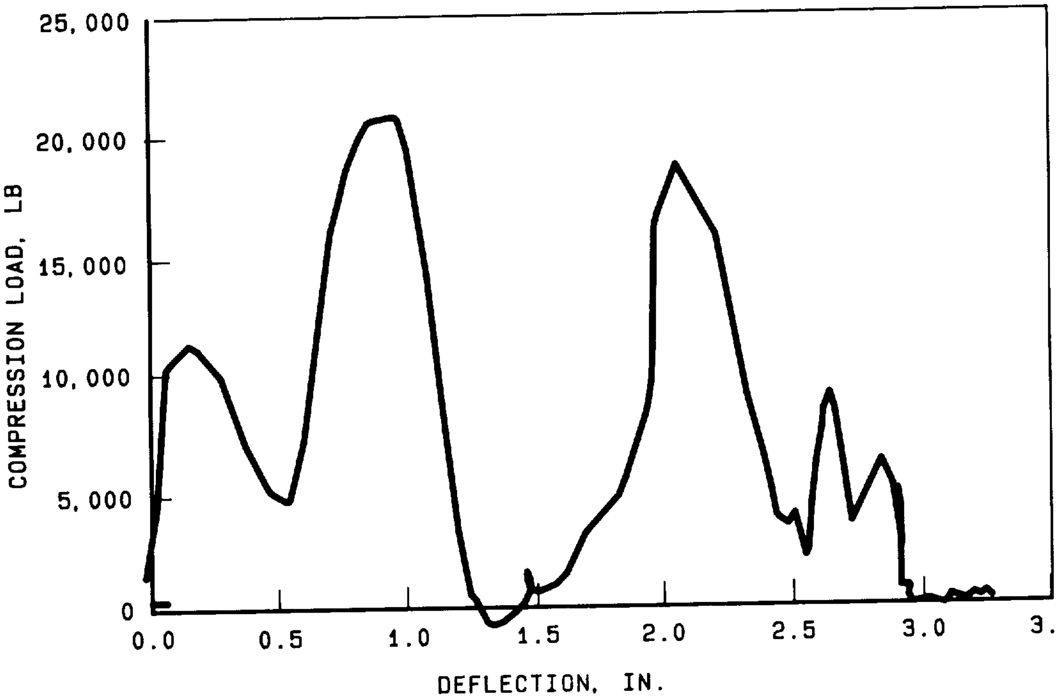

Figure 89. - Hat-stiffened composite panel/bracket (one end) load versus deflection curve - impact velocity 13 ft/sec.

ORIGINAL PAGE
BLACK AND WHITE PHOTOGRAPH

4.3.3 Chamfered hat-stiffened panel with bonded attachment bracket. - In an effort to improve energy absorption in a composite panel with caps, a specimen was fabricated with bonded brackets. It was anticipated that the bonded brackets would fail by separation from the panel skin with less tendency to force the stiffeners out of line with the load. The brackets were bonded with a high temperature structural adhesive (FM 300).

A free falling mass weighing 528 pounds was dropped onto the panel from a height which produced an impact velocity of 12 ft/sec. The load-deflection curve resulting from these histories is shown in Figure 90.

Following impact, the load built up rapidly to 18,490 pounds. At this load the brackets separated from the skin as the bond failed along the width of the panel. A brooming failure was initiated as the load dropped to an average of 9000 pounds for the duration of the test. The maximum deflection of the panel was 2.5 inches. After reaching this peak, the deflection returned to a 1.3 inches where it remained through the duration of the test. The failure mode was similar to that exhibited by other chamfered hat-stiffened composite panels except that since the brackets were separated from the skin the tendency to force the stiffeners to one side was minimized. Figure 91 shows details of brooming failure along the edge of the panel.

Figure 90. - Hat-stiffened composite panel/bonded bracket load versus deflection - impact velocity 12 ft/sec.

~~ORIGINAL PAGE IS~~
~~OF POOR QUALITY~~

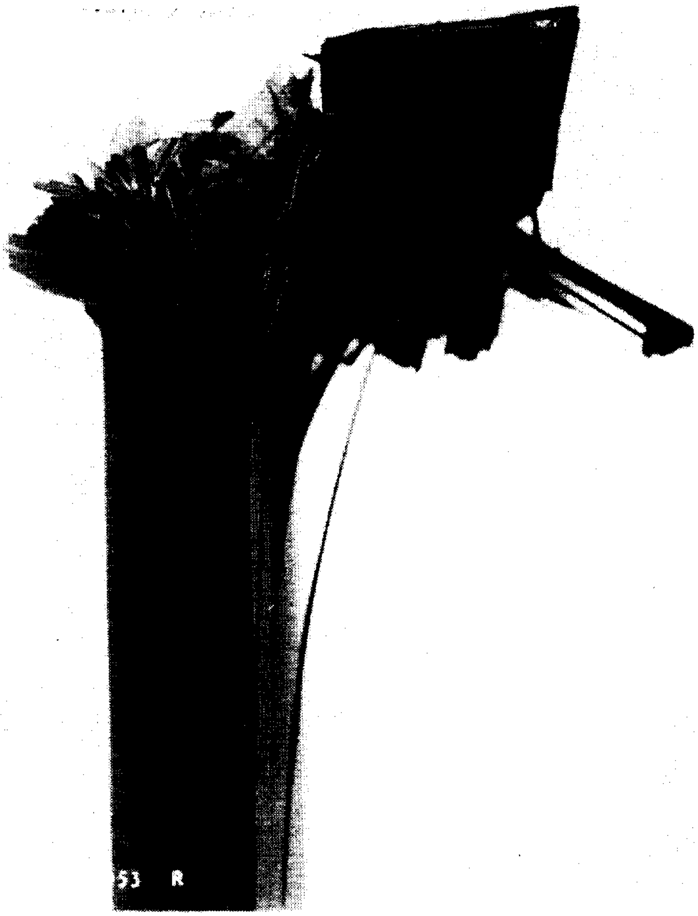

Figure 91. - Hat-stiffened composite panel/bonded bracket brooming failure mode - impact velocity 12 ft/sec.

4.3.4 Summary of modified composite panel dynamic test results. - The dynamic test results for the modified composite panels described in Sections 4.3.1, 4.3.2 and 4.3.3 are shown in Table 16. The parameters; energy absorption, average load and load uniform ratio are described earlier. The impact velocity tests ranged from 10 to 13.9 ft/sec. The limiting factor was the available free fall height for the impact head. Structural response is highly dynamic under crash impact conditions. Of special interest, therefore, is how dynamic and static test results compare. Both the corrugated and the hat-stiffened panel configurations were subjected to static and dynamic tests. The major differences in test results were the higher peak loads obtained in the dynamic tests and the correspondingly higher load uniformity ratios.

4.4 Summary of Frame Segments Static Tests Results

The frame segments are described in Section 1.2.2. The static test setup is shown in Figure 92. The load versus deflection curves for the three specimens are shown in Figures 93, 94 and 95 for the aluminum, composite concept #1, and composite concept #2 segments, respectively. The aluminum segment deformed in the manner depicted in Figure 96. The composite concept #1 exhibited a failure between fiber layers in the frame web and also in the skin. The composite concept #2, a corrugated frame section attached to a Gr/Ep skin, showed an initial failure due to separation of the frame caps from the corrugated frame webs.

ORIGINAL PAGE
BLACK AND WHITE PHOTOGRAPH

~~ORIGINAL PAGE IS~~
OF ~~POOR QUALITY~~

TABLE 16 - DYNAMIC TEST RESULTS, MODIFIED COMPOSITE PANELS

Test Specimen	Impact Velocity (ft/sec)	Maximum Load (lb)	Energy Absorption (in-lb) at inches			Average Load (lb) At 3(in)	Load Uniformity Ratio
			1.0	2.0	3.0		
Corrugated Panels	10.0	14110	8000	13300	17900	5967	2.36
	13.9	14750	6200	11600	17200	5733	2.57
Hat Stiffened Panels With Mechanically Fastened Attachment Brackets	11.0	26250	17400	18000	20900	10450	2.54
	13.0	20880	11000	13800	16000	8000	2.61
Hat Stiffened Panel With Bonded Attachment Bracket	12.0	18490	11500	17000	19000	9500 *	1.95

* At 2 inches

Figure 92. - Test setup for aluminum frame segment.

ORIGINAL PAGE
BLACK AND WHITE PHOTOGRAPH

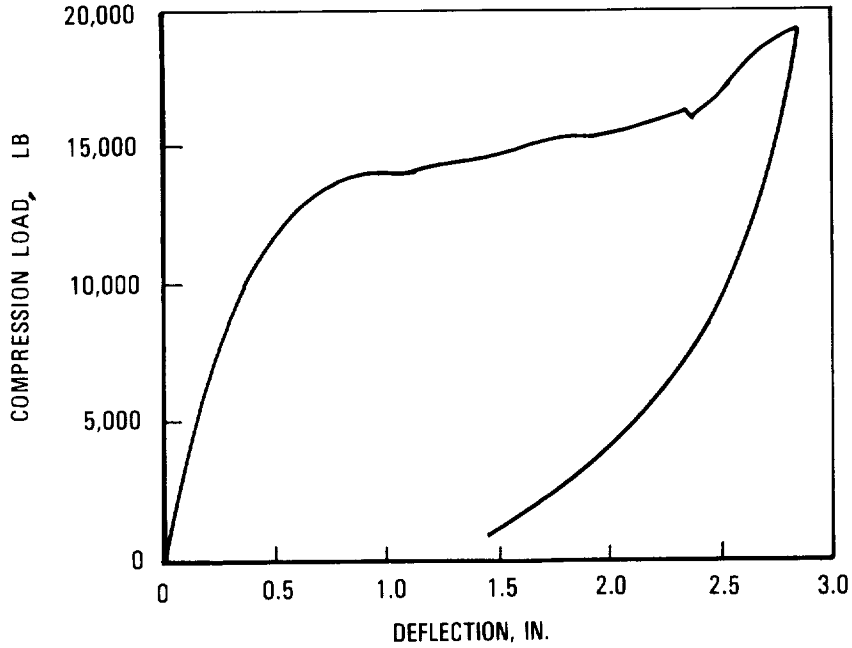

Figure 93. - Load versus deflection, aluminum frame segment.

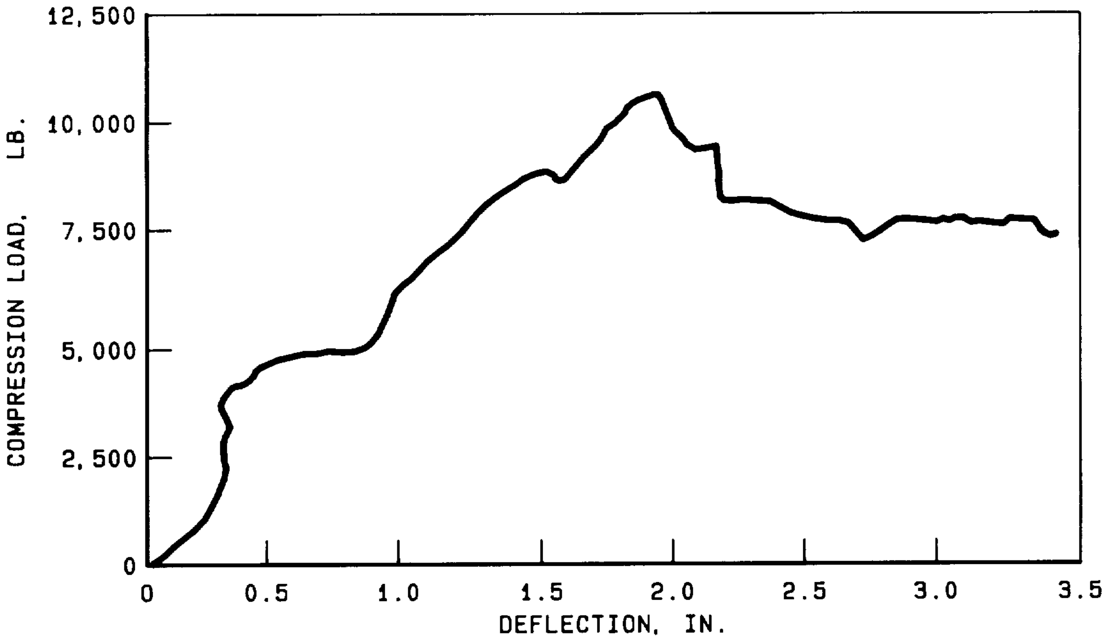

Figure 94. - Measured load versus deflection, composite frame #1.

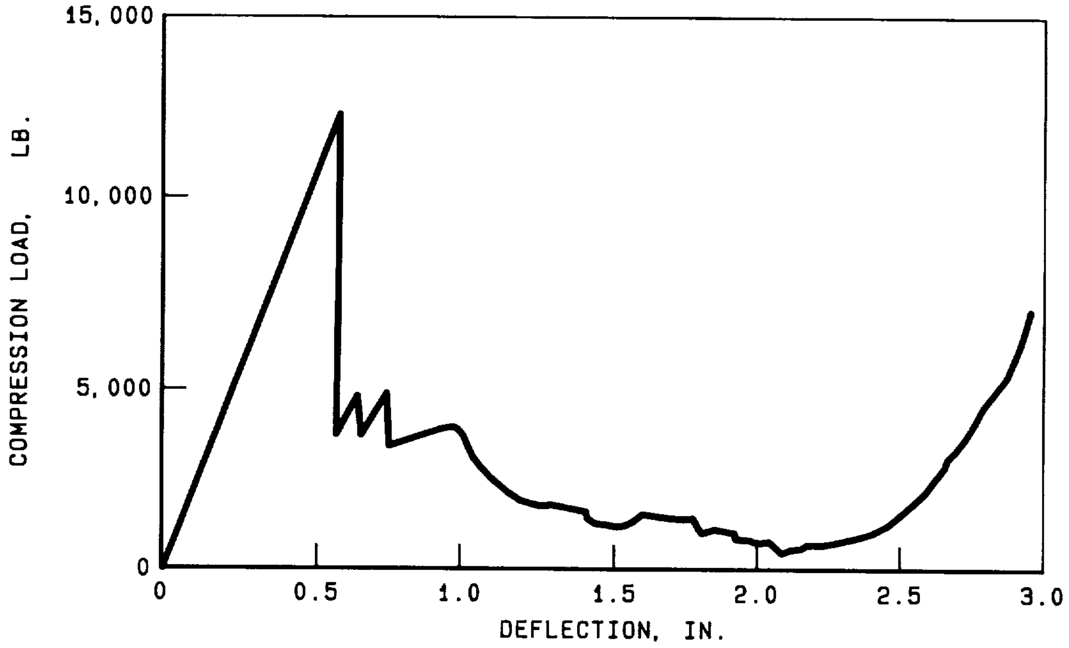

Figure 95. - Measured load versus deflection, composite frame #2.

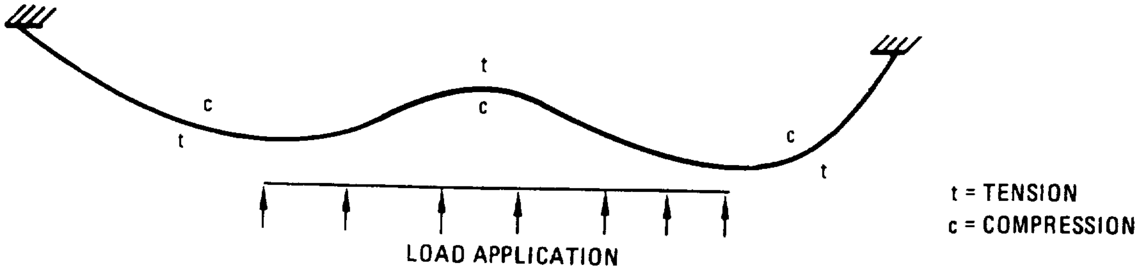

Figure 96. - Deformed shape for the aluminum frame segment.

A comparison of the failure load and energy absorption of the three frame segments is shown in Table 17. The aluminum frame exhibited the highest load, energy absorption, and specific energy absorption and the best load uniformity ratio.

TABLE 17. - COMPARISON OF FRAME SEGMENT TEST RESULTS

Frame Segment Configuration	Weight (lb)	Peak Failure Load (lb)	Deflection at Peak Fail Load (in)	Energy Absorption at 2.5 In. Deflection (in-lb)	Specific Energy (in-lb/lb)	Load Uniformity Ratio
Aluminum Z	20.80	16700*	2.50*	32600	1567	1.28
Composite Z-C	15.77	10450	1.9	16400	1040	1.59
Corrugated	15.56	12530	0.6	8450	543	3.71

*19,250 pounds at deflection of 2.86 inches

4.5 Summary of Results

The incorporation of composites into an overall design involves the interaction of more than one structural element. For example, the fuselage structure below the cargo floor referred to earlier in this section is built-up of frame section elements and shear panels which act as crushing panel elements under an impact load. Under this loading condition, the frame elements and panel elements are assumed to act in parallel in reacting the crushing load. Figure 97 illustrates the load-deflection characteristics developed during this program for several of the frame/panel combinations considered. The test results for the aluminum frame/blade-stiffened panel combination showed a disruptive failure and loss of load-carrying capability. It is hypothesized that a modified design of the stiffeners and/or specification of material would produce a more efficient post-failure load-carrying capability. Therefore, the aluminum design may be expected to show a gradual loss of load as shown. Nonetheless, composite frame/composite hat-stiffened panels with bracket attachments can achieve comparable energy absorption. The mechanically fastened bracket attachment produces an undesirable high peak failure load, which is not as evident for the bonded bracket. The reduction of the peak load, while maintaining desirable load-carrying capability, is considered a design detail that can be resolved. Based on these results, it is concluded that the feasiblity of a composite frame and panel replacing a current metal design does exist.

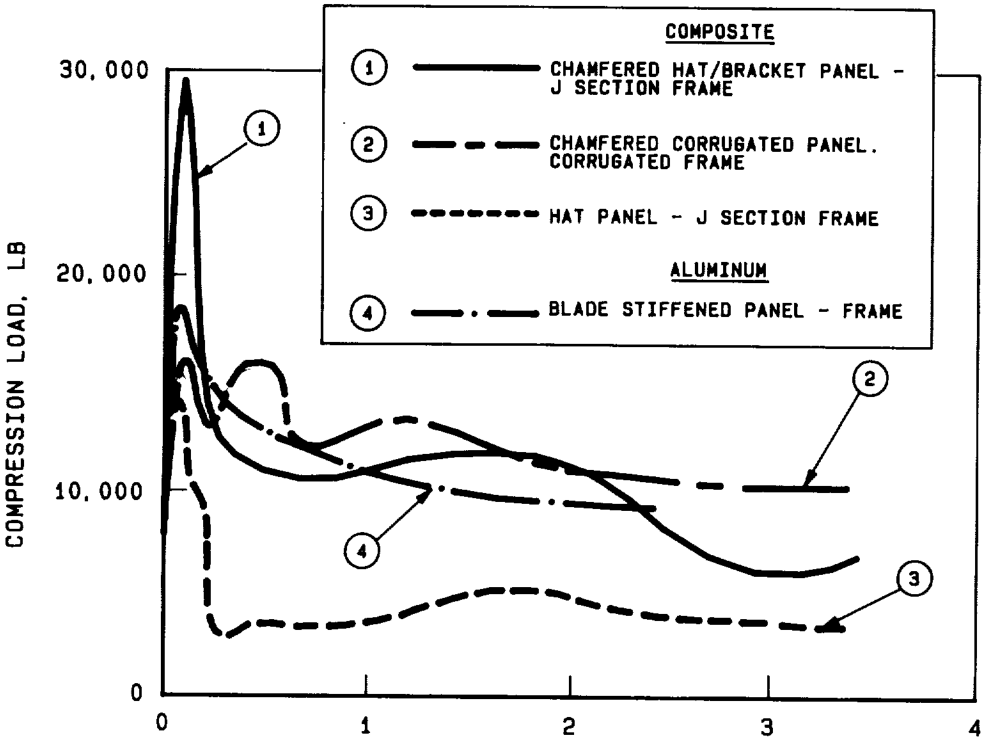

Figure 97. - Combined panel - frame static load deflection curves.

The results of the impact dynamics tests and analyses suggest that the following items are of particular concern if composites are to replace current metal designs.

- The design requirement is a function of location and loading, and quantification is necessary before alternative composites designs are pursued.
- Composite designs will most likely fail differently than the current aluminum design unless the same failure mode is designed into the structure.
- Failure mode control via the material, loading and attachment is important. If appropriate attention is paid to these details, then it is feasible to replace the metal with composites and achieve "equal or better energy absorption."
- Improved design efficiency can be achieved in excess of current metal performance, but detail design considerations are important.
- Prediction of composite failure behavior is limited but can be improved with additional tests and further understanding of potential failure modes for different design configurations and loading conditions.

5. CONCLUDING REMARKS

This program successfully achieved the major objectives of the contract. Methodology was developed for the analysis of the energy absorption of certain advanced composite structural components. Methodology was also developed for the analysis of stiffened advanced composite shells to determine the noise reduction through the shell for noise generated by external sources such as engines and turbulent boundary layer.

A series of development tests were performed to determine structural configurations and details which provide energy absorption capabilities for advanced composite fuselage structures which are as good as or better than for aluminum fuselage structures. Additional tests must be performed to determine the behaviour of larger structural components. The developments achieved in this program have demonstrated that impact dynamics criteria will not have an adverse effect on cost or weight of advanced composite structures.

Analyses of metal and composite stiffened shells demonstrated that the noise transmission loss is better with advanced composites than with metals for shells of 5 1/2 feet diameter designed to the same criteria. This is due to a reduction in the number of structural modes in the composite shell compared to the aluminum shell. This more than offsets the adverse effects of reduced wall mass. These analyses will be verified by tests which will be performed by NASA LARC using a composite fuselage shell fabricated as part of the program. Additional work must be performed through parametric analyses to extend the analytical investigation to widebody fuselage shells. If the results of such analyses follow the same trend then the introduction of advanced composites to fuselage shells will not require any increase in interior trim mass to maintain interior noise levels at those of metallic fuselage shells.

REFERENCES

1. Jackson, A. C.; Campion, M. C.; and Pei, G. "Study of Utilization of Advanced Composites in Fuselage Structures of Large Transports," NASA CR 172404, September 1984.

2. Wittlin, G. and Gamon, M.A., "Experimental Program for the Development of Improved Helicopter Structural Crashworthiness Analytical and Design Techniques," Lockheed-California Company, USAAMRDL-TR-72-72.

3. Wittlin, G. and Gamon, M.A., "Full Scale Crash Test Experimental Verification of Method of Analysis for General Aviation Airplane Structural Crashworthiness," Lockheed-California Company, FAA-RD-77-188.

4. Wittlin, G. and Lackey, F., "Analytical Modeling of Transport Aircraft Crash Scenarios to Obtain Floor Pulses," Lockheed-California Company, NASA CR 166089, DOT/FAA/CT-83-23, April 1983.

5. Federal Airworthiness Regulations Part 25 Airworthiness Standards: Transport Category Airplanes.

6. Wittlin, G. and Park, K.C., "Development and Experimental Verification of Procedures to Determine Nonlinear Load-Deflection Characteristics of Helicopter Substructures Subjected to Crash Forces," Lockheed-California Company, USAAMRDL-TR-74-12, May 1974.

7. Pope, L.D., Wilby, E.G., and Wilby, J.F., "Propeller Aircraft Interior Noise Model," NASA CR-3813, 1984.

8. Lowson, M.V., "Prediction of Boundary Layer Pressure Fluctuations," AFFDL-TR-67-167 (1968).

9. Farley, G.L.: "Engery Absorption of Composite Materials," Journal of Composite Materials, Vol. 17, May 1983.

10. Cronkhite, J.D. and Burrows, L.T.: "Crashworthiness of Helicopter Composite Structures," Proceedings of AHS National Specialists' Meeting on Composite Structure, Philadelphia, PA, March 23-25, 1983.

APPENDIX A
IMPACT DYNAMICS METHODOLOGY

A1.1 Analytical Procedures

The load deflection curve predicted by program LDCURVE is derived in three steps. In the first, a failure load is predicted using static analysis methods; in the second, a post failure curve is derived; and in the third, the failure load estimate is mated with the post failure curve to give the total load-deflection curve.

The analytical method followed in predicting the failure load is dependent on the specimen configuration and the material from which it is fabricated. For aluminum specimens subjected to a compression load, the analytical procedures follow those developed by K. C. Park and G. Wittlin described in detail in Reference A1. For specimens fabricated from composite materials and subjected to a compression load, the analytical procedures follow those developed at the Lockheed California Company.

Two procedures are available for predicting the post failure behavior of the specimen - the plastic hinge curve option and the exponential curve option. The plastic hinge curve option is based on a semi-empirical method suggested by Park and Wittlin, Reference A1. In this procedure, it is assumed that the applied compression load causes the specimen to deflect in a direction parallel to the applied load. As the specimen deflects, the cross sectional properties distort and completely collapse or fold over due to warping. Plastic hinges are assumed to form at each end and at a point midway between the loaded ends of the specimen. A semi-empirical curve is used to simulate this behavior. The constants defining the curve are a function of the undistorted, as well as the distorted cross sectional properties of the specimen. The exponential curve option is provided to accommmodate post failure behavior which can not be simulated by the plastic hinge curve option. In this option, an exponential curve is used to simulate the post failure behavior of the specimen. The coefficients defining the curve must be determined from data obtained experimentally.

In the final step of the analysis procedure, the failure load and deflection corresponding to the failure load are combined with the post failure curve to produce the total load deflection curve. The curve is characterized by a curve which exhibits a linear stiffness from the origin to the failure point and then varies according to the post failure behavior defined above. The energy absorption capability of the specimen as well as the load uniformity ratio are determined from this curve.

In the Static Failure Load Prediction and the Load Deflection Curve sections of this report, analytical and empirical expressions are presented. No attempt has been made to present the detailed development of these expressions. However, the references from which they were extracted are identified. Empirical data required in the evaluation of expressions are not included in the sections. Rather, the data, in the form of tables and curves, are included in a User's Guide.

A1.2 Program LDCURVE

The analytical procedures described in Section A1.1 have been coded and collected into program LDCURVE. The program is an interactive program written in FORTRAN language and runs on the Digital Equipment Corporation VAX 11/780 computer and VT-100 terminal. The major routines of program LDCURVE along with a brief description of their operational function follows.

LDCURVE - An executive routine which collects basic parameter data and controls the flow of the LDCURVE program.

SECPRO - A routine in which the cross sectional properties of the specimen are computed. If the specimen is fabricated from composite materials, SECPRO calls three addition routines (COMAIN, HYBCM1, HYBCM2) in which equivalent material properties (Young's Modulus, Poisson's Ratio, Shear Modulus) of the composite layup are computed for the specimen cross section.

STFPAN - A routine used to calculate the static failure load of an aluminum, stiffened panel specimen subjected to a compression load. The routine considers localized failure modes associated with short panel behavior (monolothic, wrinking, interrivet buckling); failure modes associated with Euler column behavior; and failure modes associated with the transition region between short column and Euler column behavior.

COSTIF - A routine used to calculate the static failure load of a composite, stiffened panel specimen subjected to a compression load. The routine considers localized failure modes associated with the buckling of the individual elements of the specimen cross section and failure modes associated with Euler column behavior. In the later analysis, equivalent section area and moment of inertia properties determined in SECPRO are used.

FUSFR - A routine used to calculate the static failure load of a segment of fuselage frame structure. The procedure used in the routine is based on the bending analysis of a curved beam subjected to in-plane bending. For a frame segment fabricated from composite materials, equivalent section area and moment of inertia properties determined in SECPRO are used.

CORRUG - A routine used to calculate the static failure load of a corrugated specimen fabricated from composite materials and subjected to a compression load. The routine considers localized failure modes of the corrugation configuration.

POSTB - A routine called when the exponential curve option is selected to compute the load deflection curve of the specimen. The routine uses the static failure deflection and load determined for the specimen and a post failure exponential curve to define the total load deflection curve.

POSTC - A routine called when the plastic hinge curve option is selected to compute the load deflection curve of the specimen. The routine uses the static failure load determined for the specimen and post failure plastic hinge dependent empirical curve to define the total load deflection curve.

PLTT - A routine used to plot the predicted load deflection curve. This routine uses the Integrated Software Systems Corporation graphics software package DISSPLA.

A2.0 STATIC FAILURE LOAD PREDICTION

A flow diagram, outlining the major computational paths followed in program LDCURVE in predicting the failure load of the specimens under consideration in this program, is shown in Figure A-1a/1b. Of the paths shown, only the path followed in predicting the failure load of panels fabricated from aluminum materials is based on well established methods. These methods have been developed over the years by numerous authors, References A2 - A5, from analytical procedures which have been refined into semi-empirical methods based on large amounts of experimental data. Other computational paths, are based on analytical methods which are not as well established. The methods are still under development and are under study by many investigators.

A2.1 Section Properties

As part of the failure load analysis, cross sectional properties such as area, moment of inertia, centroidal axis location, etc. are required. These properties are determined by dividing the cross sectional shape into equivalent rectangular elements. The cross sectional properties of the various rectangular elements are determined separately and then combined to given the cross sectional properties of the idealized shape.

A2.1.1 Metal section properties. - The procedure for computing the cross sectional properties of sections fabricated from aluminum materials is well documented in elementary Strength of Material text books such as Reference A8. The procedure is simple and straight forward and will not be discussed further in this report. The simple procedure has been mechanized in subroutine SECPRO.

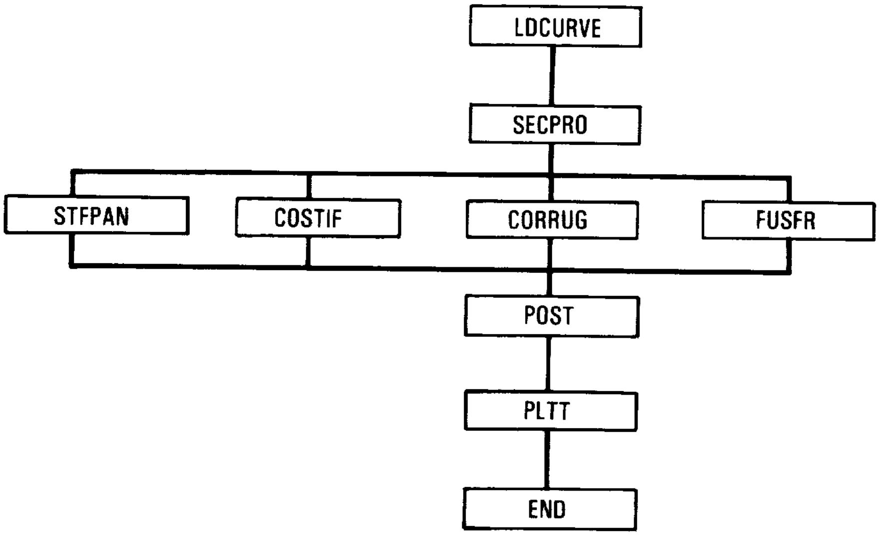

Figure A-1a. - LDCURVE program flow diagram routine.

A2.1.2 Composite section properties. - The procedure for computing the cross sectional properties of sections fabricated from composite materials such as composite fibers is similar to that followed for sections fabricated from homogeneous materials. In this case, however, equivalent laminate Elastic Modulus, Poisson's Ratio and Shear Modulus are used. The section properties of specimens fabricated from non-homogeneous materials are also computed in subroutine SECPRO. The equivalent material properties are supplied to SECPRO by subroutines HYBCM2.

A2.2 Stiffness Properties of Composite Sections

The procedure adapted for predicting the failure load of a specimen fabricated from a composite material is based on the procedures developed by Lockheed-California Company. The intitial step in the analysis is to determine the stiffness and compliance properties of the specimen. Elements of the [A], [B] and [D] matrices are calculated in subroutine HYBCM1. Matrix operations are performed in subroutine HYBCM2.

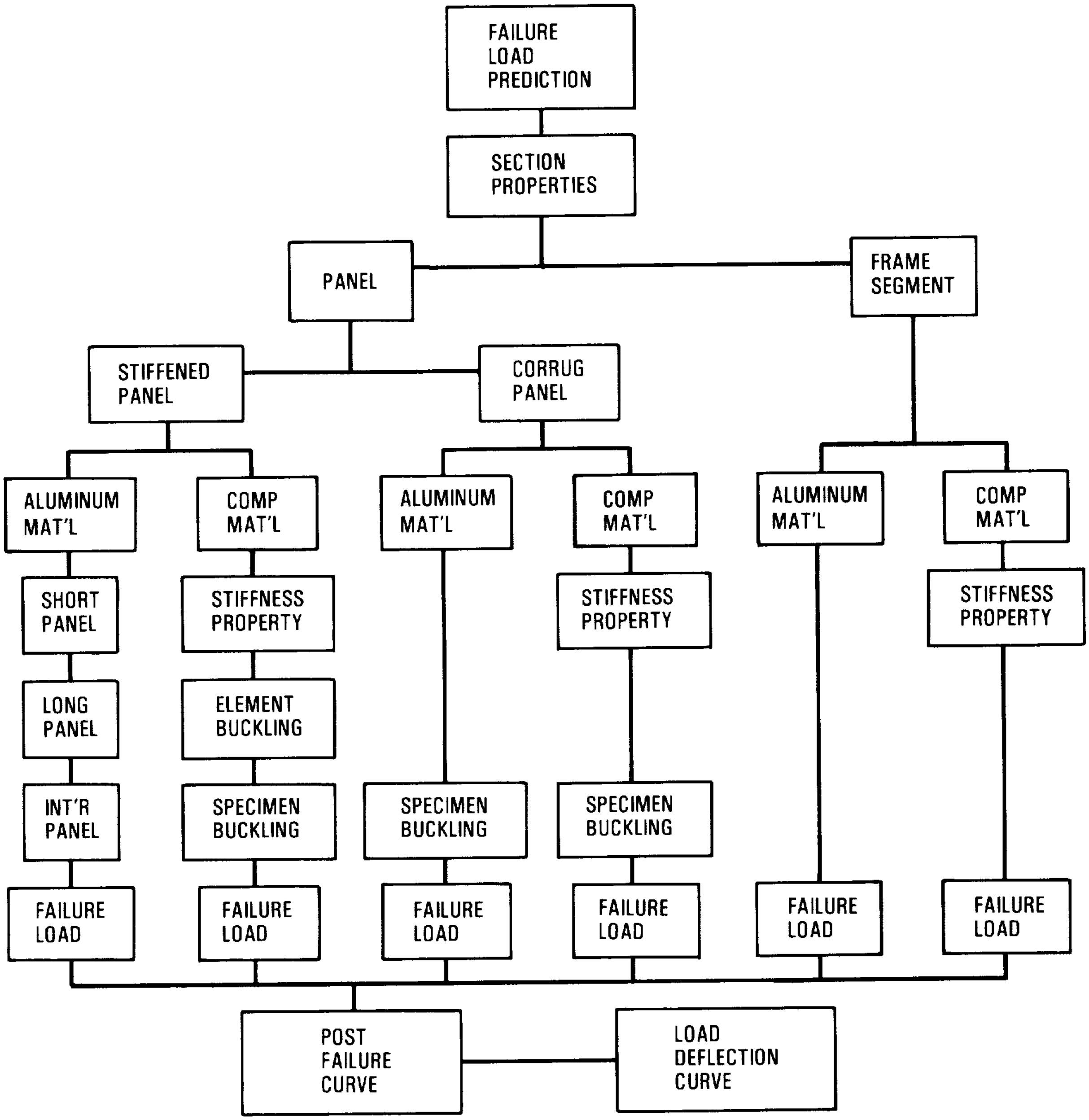

Figure A-1b. - Flow diagram - program LDCURVE.

A2.3 Panels Subjected to Compression Loads

In the static failure load analysis of a panel subjected to a compression load, two basic panel configurations are considered: the stiffened panel and the corrugated panel.

The stiffened panel configuration consists of a flat face sheet to which is attached several stiffeners. The stiffeners are assumed fabricated from the same material as the face sheet and are orientated in a direction parallel to the direction of loading. For stiffened panels fabricated from an isotropic material (in this study - aluminum), the stiffeners may be an integral part of the face sheet or they may be attached to the face sheet by rivets or spotwelds. For stiffened panels fabricated from an orthotropic material, (in this study - composite) the stiffeners are assembled to be an integral part of the face sheet.

The corrugated panel consists of a single plate which has been formed into a series of corrugations. The corrugations are assumed to be orientated parallel to the direction of loading.

A2.3.1 Stiffened metal panels. - The procedure adapted for predicting the failure load of a stiffened panel subjected to a compression load is that developed by Park and Wittlin, Reference A1. Although originally developed for the analysis of helicopter substructure subjected to crash forces, the procedure is general in nature and well suited for the analysis of panels subjected to compression loads.

The analysis investigates the failure load associated with each of three characteristic panel lengths. The three characteristic panel lengths are:

Short panel (ratio of equivalent length to radius of gyration less than 30) - These panels generally exhibit failure modes charcterized as crippling.

Long panel - These panels behave essentially as Euler columns.

Intermediate length panel - These panels generally fail as a result of combined crippling and column instability with torsional effects often evident.

A2.3.2 Composite specimens. - The procedure followed in predicting the failure load of a composite panel subjected to a compression load is based on the analysis procedure developed by Lockheed-California Company. In the analysis the idealized elements used in the calculation of section properties (Section A2.1.2) define flat plates. The buckling load for each of the idealized plates is computed.

The buckling load calculations are made in subroutine ORBUCK. Two boundary condition options have been considered - (1) four sides of the idealized plate simply supported and (2) three sides simply supported and the fourth side free. In both boundary condition options, the loaded ends are simply supported. The elements of the partially inverted bending stiffness submatrix [D] are used in the computation of the buckling loads. After computing the buckling loads of each of the idealized plate elements, the element loads are combined to give the minimum buckling load for the specimen.

A2.3.3 Corrugated panels. - The analytical procedure followed to determine the failure load of a corrugated panel subjected to a compression load is based on the analytical methods developed by Lockheed-California Company.

The analysis of the composite corrugated panel is also accomplished in subroutine CORRUG. In the analysis the failure load is determined based on a general instability failure as well as a local instability failure. The minimum stress produced in these two failure modes is used to determine the failure load value. Equivalent stiffness properties are used in the calculation of the critical stresses.

A2.4 Fuselage Frame Sections

The analysis procedure followed to determine the failure load of a fuselage frame section is based on the elastic analysis of curved arches as discussed in references A7 through A9. The equations used in program LDCURVE are taken from Reference A7. These equations reduce to those given in Reference A8 when the radius of the circular arch is large compared to the cross sectional moment of inertia of the arch. End condition options are pinned or fixed.

A2.4.1 Metal specimens.- The analysis of the metal fuselage frame section is accomplished in subroutine FUSFR. The analysis is straight forward and consists of the simple substitution of appropriate parameter data into the above equations. The section properties are supplied by subroutine SECPRO.

A2.4.2 Composite specimens.- The analysis of the composite fuselage frame section is also accomplished in subroutine FUSRF. For the composite section, however, equivalent section properties supplied by subroutine SECPRO are used.

A3.0 LOAD DEFLECTION CURVE

A3.1 Post Failure Load Deflection Curve

Except for the cases of simple geometry and boundary conditions, available methods for predicting the behavior of structures after the failure load has been reached requires a sophisticated level of analysis. Therefore, two simplified methods have been provided in program LDCURVE for predicting the behavior of the specimens. The first is a simplified semi-empirical method suggested by Park and Wittlin, reference A1, that is based on the formation of plastic hinges. The second is even more simplified in that it allows for input of coefficient data which define an exponential representation of the load deflection curve.

A3.1.1 Plastic hinge curve. - In the analysis of Park and Wittlin, the following assumptions are made:

- At the threshold of failure load, full plastic hinges are developed at constrained supports and at the mid span of the specimen.
- The free warping energy of the flange of the stiffener is neglected.
- The effect of strain hardening is neglected.
- The influence of the axial force on the plastic hinge mechanism of the stiffened panel is neglected.
- The effect of geometrical imperfection sensitivity is neglected.

A sketch of a typical segment of stiffened panel, during post failure deformation is shown in Figure A-2. As the panel is axially loaded it shortens and plastic hinges are formed at each end and at a point midway between the loaded ends of the panel. As the compression load persists the panel continues to bend until the stiffener distorts and collapses. Park and Wittlin suggest a post failure curve with the general shape shown in Figure A-3. The curve corresponding to the minimum plastic hinge moment is based on the assumption that the stiffener completely collapses or folds over due to warping. This condition results in a much lower stiffener moment of inertia and bending stiffness than would be obtained if the stiffener remained fully formed. This mode of failure also yields a lower deflection per given load than would be expected when compared to test data. Thus, the assumption of a completely collapsed stiffener leads to an overly conservative hinge moment and thus leads to greater deflections than the test data appears to warrant. The curve corresponding to the maximum plastic hinge moment is based on the assemption that the stiffeners do not deform and remain fully formed. This assumption leads to predicted deflections which are smaller than seem warranted when compared to test data.

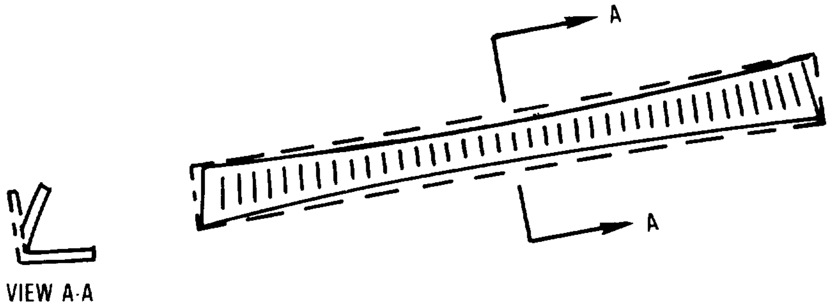

(a) INTERMEDIATE WARPING OF FLANGE DUE TO FORCED BENDING OF WEB.

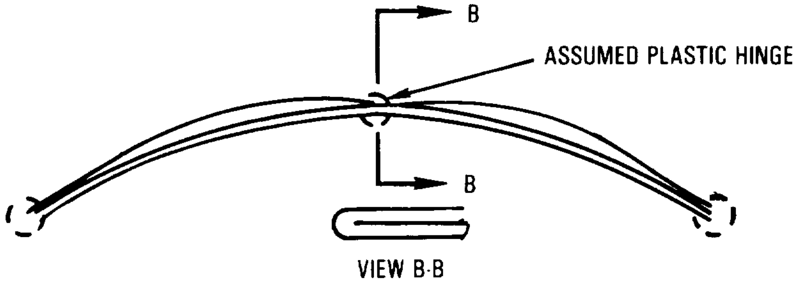

(b) LIMITING CASE OF FLANGE FOLDING DUE TO FREE WARPING.

Figure A-2. - Stiffened panel segment during post failure deformation.

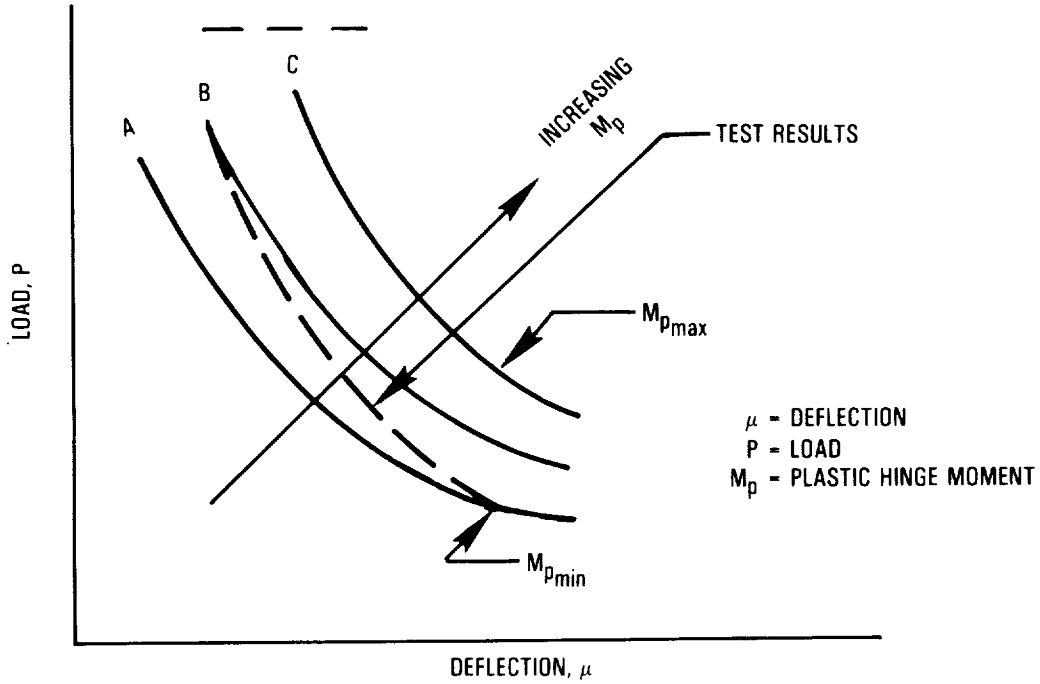

Figure A-3. - Post-failure load-deflection curves.

A3.1.2 *Exponential curve*.- The exponential curve option is provided to accommodate post failure behavior which can not be simulated by the plastic hinge option. The general equation for the curve is

$$F = F_{min} + \frac{A}{\delta k}$$

where

F = post failure load

F_{min} = asymptotic load

δ = post failure deflection

k = exponent

A = $\delta_f^k (F_f - F_{min})$

δ_f = failure deflection

F_f = failure load

The coefficient, A, and exponent, k, must be determined from data obtained experimentally.

A3.2 Total Load Deflection Curve

In the final step of the analysis procedure, the deflection corresponding to the failure load is obtained from the intersection of the failure load and a coinciding load from the post failure load deflection curve. The total load deflection curve is represented by a curve which exhibits a linear stiffness from the origin to the failure point and then varies according to the post failure behavior defined above. The energy absorption capability of the specimen as well as the load uniformity ratio are determined from this curve.

REFERENCES

A1 Wittlin, G. and Park, K. C. "Development and Experimental Verification of Procedures to Determine Nonlinear Load-Deflection Characteristics of Helicopter Substructures Subjected to Crash Forces, "USAAMRDL-TR-74-12, May 1974.

A2 Gerard, G. and Herbert, B. "Handbook of Structural Stability, Part I - Buckling of Flat Plates," NACA TN 3781, July 1957.

A3 Becker, H. "Handbook of Structural Stability, Part II - Buckling of Composite Elements," NACA TN 3782. July 1957.

A4 Gerard, G. "Handbook of Structural Stability, Part IV - Failure of Plates and Composite Elements," NACA TN 3784, August 1957.

A5 Gerard, G. "Handbook of Structural Stability, Part V - Compressive Strength of Flat Stiffened Panels, NACA TN 3785, August 1957.

A6 Shanley, F. R. Strength of Materials. New York: McGraw-Hill Book Company, Inc., 1957.

A7 Roark, Raymond J. Formulas for Stress and Strain, Fourth Edition. New York: McGraw-Hill Book Company, Inc., 1965.

A8 Blake, Alexander, Practical Stress Analysis in Engineering Design. New York: Marcel Dekker, Inc., 1982.

A9 Blake, Alexander, "How to Find Deflection and Moment of Rings and Arculate Beams," Product Engineering, January, 1963.

APPENDIX B

ACOUSTIC TRANSMISSION METHODOLOGY

Program Description

The computer program developed for this study is summarized in Figure B-1. An understanding of the computer program operation is facilitated by reference to the flow diagram in Figure B-2. There are five main FORTRAN subroutines:

1. "ABD" which computes the material property matrices and stiffener geometry from an input data set.
2. "CYL2D" which computes the acoustic modes for a cross section of the fuselage with or without a floor.
3. "MRPCOMP" which computes the resonant frequencies and symmetric and unsymmetric mode shapes for the fuselage structure with and without a floor.
4. "MRPMOD" takes the symmetric and unsymmetric modal data generated by MRPCOMP and conditions the data for use by the interior noise prediction program.
5. "PAINML" is the interior noise prediction subroutine. It takes the two-dimensional acoustic mode data from CYL2D and the conditioned structural mode data from MRPMOD to compute interior noise levels.

Included in the PAINML subroutine are the capabilities to:

1. Add interior trim elements to the fuselage wall.
2. Simulate a free-field exponential horn excitation of the fuselage.
3. Simulate a reverberant field excitation of the fuselage.
4. Simulate a laboratory or inflight turbulent boundary layer excitation.
5. Use previously measured or calculated propeller noise to excite the fuselage.

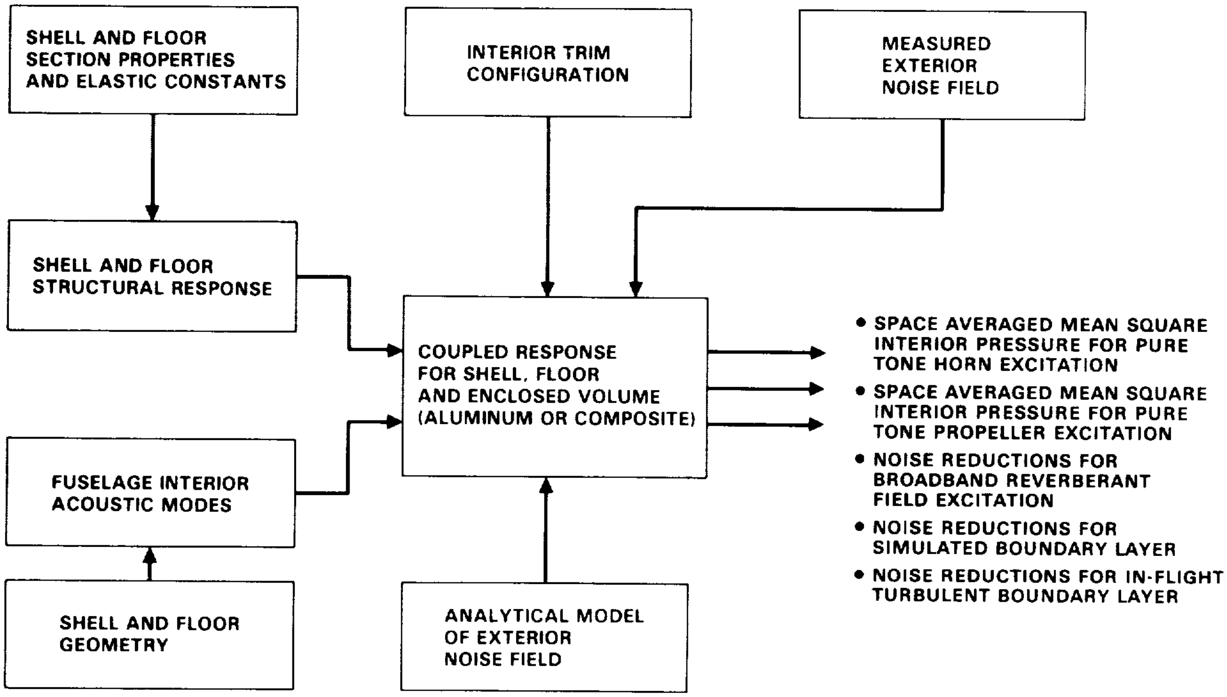

Figure B-1. - Acoustic transmission prediction program.

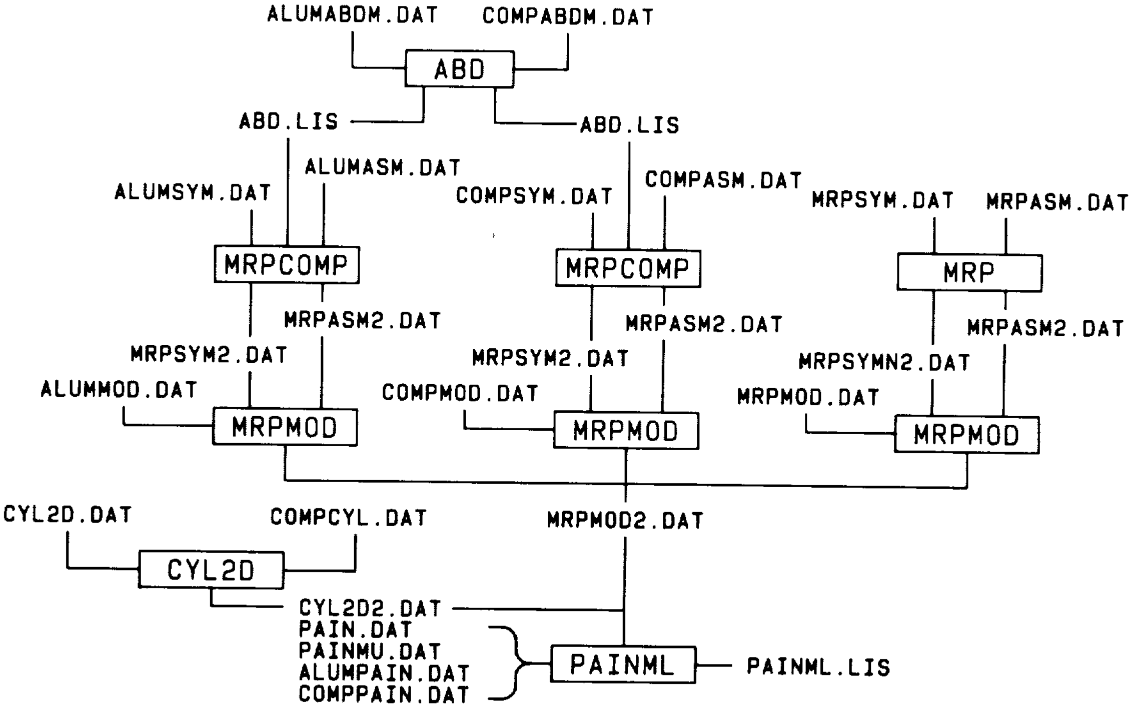

Figure B-2. - Acoustic analysis flow diagram.

The input and output files or data sets for each of the main subroutines are briefly described below.

ABDLIS - Output file and listing from the ABD stiffener program. Will be used by MRPCOMP program as input file.

ALUMABDM.DAT - Input file for ABD stiffener program for aluminum.

ALUMASN.DAT - Input file for MRPCOMP program for aluminum.

ALUMMOD.DAT - Input file for MRPMOD program for aluminum.

ALUMPAIN.DAT - Input file for PAINML program for aluminum.

ALUMSYM.DAT - Input file for MRCOMP program for aluminum.

COMPABDM.DAT - Input file for ABD stiffener program for composite.

COMPCYL.DAT - Input file for CYL2D program for composite and aluminum.

COMPASM.DAT - Input file for MRPCOMP program composite.

COMPMOD.DAT - Input file for MRPMOD program for composite.

COMPPAIN.DAT - Input file for PAINML program for composite.

COMPSYM.DAT - Input file for MRPCOMP program for composite.

CYL2D.DAT - Input file for CYL2D program (Original Test Case).

CYL2D2.DAT - Output file from CYL2D program. Will be used by PAINML program as input file.

MRPASM.DAT - Input file for MRP program (Original Test Case).

MRPASM2.DAT - Output file from MRPCOMP. Will be used by MRPMOD program as input file.

MRPMOD.DAT - Input file for MRPMOD program (Original Test Case).

MRPMOD2.DAT - Output file from MRPMOD program. Will be used by PAINML program as input file.

MRPSYN.DAT - Input file for MRP program (Original Test Case).

PAIN.DAT - Input file for PAINML program (Original Test Case).

PAIND.DAT - Input file for PAINML program (Original Test Case).

PAINML.LIS - Final Output (Predicted Interior Noise).

Theory of Boundary Layer Noise Transmission - Stiffened Composite Fuselage Cabin With Trim

This section contains an overview of the theoretical methods to be used to predict noise inside the cabin of a composite aircraft arising from a (convected) turbulent boundary layer on the exterior.

The fuselage is assumed to have a composite skin stiffened by composite frames (rings) and composite stringers. Also, it is assumed to have a composite floor stiffened by composite transverse floor beams (floor frames) and composite longitudinal stiffeners (floor stringers). The interior of the fuselage is assumed to be lined with a trim consisting of a number of different layers of insulation, airgaps, or septor (in any combination), with the final layer exposed inwardly being the trim panel.

The basis for the interior noise prediction methodology is a power balance. The net time averaged acoustic power being radiated inwardly by the vibration of the trim lining (panel) must be equal the net time averaged power absorbed in the cabin volume or on its bounding surfaces (including the transmitting trim), i.e.,

$$W_{in} = W_{diss} \cdot \qquad (1)$$

The objectives of this approach are to express the inflowing power in terms of the known external fluctuating pressure (turbulent boundary layer) and the dissipated power in terms of the acoustic pressure in the cabin. Equation (1) is used to determine the cabin acoustic pressure as a function of the external fluctuating pressure. This analytical method has been documented in References B1, B2 and B3, and has been validated for noise and tone transmission through a variety of aircraft type structures. Unstiffened and stiffened cylinders analyses are validated for propeller noise transmission through a model aluminum fuselage with floor (similar to the composite fuselage of concern) in References B4 and B5. Validation studies were also performed for propeller noise transmission into the cabin of a turboprop commuter aircraft (Reference B6) and jet noise transmission into the payload bay of the space shuttle orbiter vehicle (Reference B7).

The analytical model assumes that there are no acoustic losses in the cabin volume, all sound in the cabin originates at the wall and is absorbed on the wall. The first key to understanding the problem is to realize that the sound pressure level in the cabin space must rise until the net power inflow is zero (averaged in time and over the bounding surface of the cabin). This result must be true because a stationary value in the cabin) cannot exist if either one of the inwardly or outwardly flowing power components exceeds the other. The second key is that the surface velocity (of the trim lining) has two components. One is called the "driving velocity" which causes power transmission into the space, and the other is called the "absorbing velocity," which results in a power outflow from the cabin. The absorbing velocity, v_a, is the trim response that would result from excitation by an independent sound field in the interior space. The driving velocity, v , of the trim, is the velocity that drives the interior, i.e., it is the component of the total surface velocity of the trim lining (given by v_2) necessary for there to be a net inward flowing power of zero, if the cabin space is excited by the trim

$$v_2 = v_\omega + v_a \cdot \tag{2}$$

Note that if v is zero (no external excitation leads to $v = o$)

$$v_2 \Big|_{v_\omega = 0} = v_a = -\frac{\beta}{\rho c} p_2^i \tag{3}$$

Here β is the admittance looking into the trim (the reciprocal of the impedance), ρ and c are the density and sound speed in the cabin, and p_2^i is the acoustic pressure in the cabin on the surface of the trim. it can be shown, Reference B5, that

$$\beta = \varrho c \, \frac{-\omega^2 a_{21} Z_1 + i\omega a_{22}}{i\omega a_{11} Z_1 + a_{12}} \tag{4}$$

where the a_{ij} are elements of a trim transfer matrix, a matrix that describes the transfer of pressure and displacement (or velocity) across the multilayer trim

$$\begin{Bmatrix} p_2^i \\ w_2 \end{Bmatrix} = \begin{bmatrix} a_{11} & a_{12} \\ a_{21} & a_{22} \end{bmatrix} \begin{Bmatrix} p_1^i \\ w_1 \end{Bmatrix} \tag{5}$$

where

w_1 = displacement of the fuselage skin

p_1^i = pressure on the inner surface of the skin

w_2 = displacement of the trim panel

p_2^i = pressure on the trim surface exposed to the cabin

Z_1 = local impedance of fuselage structure

Since Z_1 is a substantial "backing" impedance,

$$\beta \simeq \frac{-\varrho c \omega^2 a_{21} Z_1}{i\omega a_{11} Z_1} = \frac{i\varrho c \omega a_{21}}{a_{11}} \tag{6}$$

Substituting (6) into (3), and then (3) into (2) gives

$$v_2 = v_\omega - \frac{i\omega a_{21}}{a_{11}} p_2^i$$

or, in terms of the "driving displacement" $w_\omega = + i v_\omega/\omega$, and the net displacement $w_2 = + i v_2/\omega$,

$$w_2 = w_\omega + \frac{a_{21}}{a_{11}} p_2^i \tag{7}$$

But using the trim transfer matrix, equation (5), it is found that

$$w = \frac{w_1}{a_{11}} + \frac{a_{21}}{a_{11}} p_2^i \tag{8}$$

By comparing (7) and (8), it is found that the driving displacement is

$$w_\omega = \frac{w_1}{a_{11}} \tag{9}$$

It can also be shown, Reference B4, by an elaborate analysis, that w_2 is also approximately w_1/a_{11} (actually this is almost obvious if β is small enough), so that inwardly flowing power can be calculated based on w_2 using

$$\left|w_2\right|^2 = \tau_t \left|w_1\right|^2 \tag{10}$$

where $\tau_t = \left| a_{11}^{-1} \right|^2$ is effectively the "transmission coefficient" of the trim. The importance of equation (10) is that it relates trim lining displacement (or velocity) to sidewall displacement (or velocity) for purposes of power transmission through the trim.

Power Radiated to Cabin

Let $p_2^i(t)$ and $v_2(t)$ be random noises. The inflowing power (radiation to the interior) is, on the average

$$W_{in} = \int_{\bar{x}} < p_2^i (\bar{x}, t)\, v_2 (\bar{x}, t) >_t d\bar{x},$$

where $\bar{x}$ is the sidewall area through which the TBL noise is flowing. It can be shown, Reference B2 that this is given by

$$W_{in} = \mathrm{Re}\int_{\bar{x}}\int_{0}^{\infty} S_{p_2^i v_2}(\bar{x}, \omega)\, dw\, d\bar{x}, \tag{11}$$

where $S_{p_2^i v_2}(\bar{x}, \omega)$ is the cross power spectral density of pressure (on the trim) with trim velocity, and is given by

$$S_{p_2^i v_2}(\bar{x}, w) = -i\rho w^3 \int_{\bar{x}} G_p(\bar{x}|\bar{x}'; \omega)\, S_{w_2}(\bar{x}'|\bar{x}; \omega)\, d\bar{x}' \tag{12}$$

where $G_p(\bar{x}|\bar{x}', \omega)$ is the Green's function for the interior space, and S_{w_2} is the cross PSD of trim displacement resulting from the excitation. According to the model used to define the driving displacement, this latter term is related to the cross PSD of sidewall structure displacement according to equation (10), i.e.,

$$S_{w_2}(\bar{x}|\bar{x}'; \omega) = \tau_t\, S_{w_1}(\bar{x}|\bar{x}'; \omega) \tag{13}$$

S_{w_1} is given in terms of the modes, r, of the composite fuselage by, Reference B1

$$S_{w_1}(\bar{x}|\bar{x}'; \omega) = X_e^2\, S_{p_{b1}}(\omega) \sum_{r} \left|\alpha_{rr}\right|^{2} \psi^{r}(\bar{x})\, {}^{r}(\bar{x}')\, j_r^2(\omega), \tag{14}$$

where α_{rr} is the modal receptance, $\psi^r(\bar{x})$ is the mode shape, $S_{p_{b1}}(\omega)$ is the power spectral density of the TBL noise, and $j_r^2(\omega)$ is the joint acceptance function of the mode r to the convected turbulent boundary layer. X_e is the exterior surface area of the fuselage shell.

After substitution of (12), (13), and (14) into (11), and performance of the integrations, the following result is found for the inflowing power for a given band, of width $\Delta\omega$, through sidewall area X into cabin volume V:

$$W_{in}^{\Delta\omega} = \frac{\langle P_{b1}^2 \rangle_{\Delta\omega}}{C_\omega} \frac{4X^2}{\varrho V} \tau_{ML} \tau_t$$

$$\cdot \sum_n \epsilon_n \eta_n \sum_r \frac{jr^2(\omega)\, f'^2(n, r)\, \Omega(n, r)}{M_r^2} . \qquad (15)$$

Here $\langle P_{b1}^2 \rangle_{\Delta\omega}$ is the band-limited mean square blocked pressure for the TBL noise (band $\Delta\omega = c_\omega \omega$, where ω = center frequency of band). The overbar implies an average value over the excited structural area X_e. The following are nondimensional variables

$\overline{M}_r = Mr / \frac{mX_e}{4}$ = the normalized mass

$\tau_{ML} = \frac{2\rho c}{\omega m}^{2}$ = the mass law transmission coefficient (based on average sidewall mass m and interior ρ and c)

$\Omega(n,r)$ = a frequency (and damping) dependent receptance function

τ_t = the trim transfer coefficient

$jr^2(\omega)$ = the joint acceptance evaluated at w

$f'(n,r)$ = the structure interior coupling factor

ϵ_n = the acoustic mode normalization constant

η_n = the acoustic mode loss factor

Here

$$\Omega\,(n,\,r) = \frac{\omega^2\omega_n^2}{D_{nr}}\left[\left(\frac{c_r - c_n}{4}\right)\ell n_n \right.$$

$$+ \left(\frac{2\,c_n\,(b_r - b_n) - b_n\,(c_r - c_n)}{4\,\eta_n\omega_n^2}\right)\mathrm{arctan}_n$$

$$+ \left(\frac{c_n - c_r}{4}\right)\overset{\psi}{\ell\, n_r}$$

$$\left. + \left(\frac{2c_r\,(b_n - b_r) - b_r\,(c_n - c_r)}{2 \qquad 4\,\eta'_r\,\omega_r^2}\right)\mathrm{arctan}_r\right]$$

Reference (B3) may be consulted for definition of terms in $\Omega(n,r)$, however it is noted here that this term determines how structural and acoustic modes exchange energy in the frequency domain, ω_n and ω_r are resonance frequencies of acoustic and structural modes, η_r' is a loss factor associated with structural mode r. It reduces to η_r, the structural mode loss factor (of the bare composite structure) if there is no trim on the sidewall:

$$(\eta'_r)^2 = \frac{|C_W|^2}{\bar{m}_r^2\,\omega_r^4} - \frac{2\,C_W^I\,\eta_r}{\bar{m}_r\omega_r^2} + \eta_r^2$$

The term $C_W = C_W^R + i\,C_W^I$ is defined by components of the trim transfer matrix, i.e.,

$$C_W = \frac{-a_{12}\,a_{22}}{1 + a_{12}\,a_{21}}$$

Note η_r' represents damping (for acoustic transmission purposes) that is "gained" by trimming the bare fuselage. $\bar{\bar{m}}_r$ is a "weighting" function that depends on placement of the trim.

The structure-interior coupling function is given by

$$f'(n, r) = \frac{1}{X} \int_X \psi^r(\bar{x})\, \phi_n(\bar{x})\, d\bar{x},$$

where $\phi_n(\bar{x})$ is the acoustic mode shape, normalized so that

$$\frac{1}{V} \iiint_V \phi_n^2 \, dV = \frac{1}{\varepsilon_n}.$$

Power Absorbed from Cabin

The flow of power to the wall is derived similarly, except it is based on absorbing surface velocity, defined in terms of the wall admittance β

$$W_{diss} = \frac{1}{\varrho c} \int_X \int_0^\infty \mathrm{Re}\,[\beta] S_{p_2 i}(\bar{x}, \omega)\, d\,\bar{x}\, d\omega$$

By expressing the internal pressure over the wall in terms of the modes of the cabin, and limiting W_{diss} to band, $\Delta\omega$, it can shown, Reference B3, that

$$W_{diss}^{\Delta\omega} = \frac{V}{\varrho c^2} \sum_n \frac{\eta_n \omega_n^2}{w} <P_n^2>_{s,t}^{\Delta\omega} \tag{16}$$

where $\langle P_n^2 \rangle_{s,t}^{\Delta\omega}$ is the space-average mean square pressure in the cabin attributable to acoustic mode n (at frequency ω).

Now the space-average mean square pressure in the interior is the sum of the $\langle P_n^2 \rangle_{s,t}^{\Delta\omega}$, i.e.,

$$\langle P_i^2 \rangle_{s,t}^{\Delta\omega} = \sum_n \langle P_n^2 \rangle_{s,t}^{\Delta\omega}$$

Equating (15) and (16), solving for $\langle P_n^2 \rangle_{s,t}^{\Delta\omega}$, and substituting into (17) gives

$$\langle P_i^2 \rangle_{s,t}^{\Delta\omega} = \frac{4\, c^2}{c_\omega} \frac{X^2}{V^2} \tau_{ML}\, \tau_t\, \overline{\langle P_{b1}^2 \rangle}_{\Delta\omega} \cdot \sum_n \omega_n^{\frac{n}{2}} \sum_r \frac{j_r^2(\omega)\, f'^2(n, r)\, \Omega(n, r)}{\bar{M}_r^2} \qquad (18)$$

This is the desired result (i.e., one form of the required solution). It is used at frequencies where modal data can be generated. However, acoustic modal data is so dense, that it becomes impractical to compute (or store) above certain frequencies (the larger the fuselage, the lower these frequencies become). Thus it is necessary to put equation (18) into another form that is calculable (while maintaining its integrity), assuming that at the frequencies of concern, the acoustic modal data are available.

High Frequency Model (no modal acoustic data)

The basic requirement is to realize that the response is going to be that of resonant acoustic modes, i.e., n acoustic modes within bandwidth $\Delta\omega$. The transmitting structural modes will be either resonance controlled i.e., r structural modes within bandwidth $\Delta\omega$ or mass controlled ($r < \Delta\omega$). Each acoustic mode n and structural mode r with resonance frequencies ω_n and ω_r in band $\Delta\omega$ is assumed to be "distributed" in $\Delta\omega$ with a uniform probability distribution function

$$P(\omega_r) = \frac{\omega_r - \omega}{\Delta\omega} + \frac{1}{2}$$

$$P(\omega_n) = \frac{\omega_n - \omega}{\Delta\omega} + \frac{1}{2}$$

In other words, there is assumed to be equal likelihood of finding modes known to be resonant in $\Delta\omega$ anywhere in the band. ω_n and ω_r are now considered to be random variables.

The expected value of (18) for these assumed distributions is

$$E\left[< P_i^2 >{}^{\Delta\omega}_{s,t}\right] = \frac{\tau_t \, \tau' \, \overline{X}}{2 \, \bar{\alpha} \, S} < P_{b1}^2 > \Delta\omega, \tag{19}$$

where the transmission coefficient τ' is

$$\tau' = \tau_f' + \tau_R'$$

with

$$\tau_{f'} = \tau_f \left(\frac{2 \displaystyle\sum_{r < \Delta\omega} j_r^2(\omega) \, j_r^{2\,\text{rev}}(\omega)/\overline{M}_r^{\,2}}{\displaystyle\sum_{r < \Delta\omega} \left[j_{r\,(\omega)}^{2\,\text{rev}\;2} \right]} \right)$$

and
$$\tau_{R'} = \tau_R \frac{< j_{r\,(\omega)_r}^2 \; j_{r\,(\omega_r)}^{2\;\text{rev}}/\overline{M}^2 >_{r\varepsilon\Delta\omega}}{< j_{r\,(\omega_r)}^{2\;\text{rev}} >^2_{r\varepsilon\Delta\omega}}$$

Here τ_f = field incidence transmission coefficient for mass controlled panels

$$\tau_f = \frac{32}{\pi} \frac{X}{m^2} \varrho^2 \sum_{r < \Delta\omega} \left[j^{2\ \mathrm{rev}}_{r(\omega)} \right]^2,$$

and τ_R = resonant (or resonance controlled) transmission coefficient

$$\tau_R = \left(2 n_r \pi^2 c_0 \eta^{\mathrm{ext}}_{\mathrm{rad}} \eta^{\mathrm{int}}_{\mathrm{rad}} / \varrho_0 \omega \eta_r' \right) \left(\frac{4 \varrho c}{Xe} \right)$$

The external and internal looking radiation efficiencies are the following

$$\eta^{\mathrm{ext}}_{\mathrm{rad}} = \frac{2 \varrho_0 \omega Xe}{\pi m v_{c_0}} < jr^{2\ \mathrm{rev}}(\omega) >_{r \in \Delta\omega}$$

$$\eta^{\mathrm{int}}_{\mathrm{rad}} = \frac{2 \varrho \omega\ X}{\pi m c} < jr^{2\ \mathrm{rev}}(\omega) >_{r \in \Delta\omega}$$

n_r is the structural modal density (band $\Delta\omega$) and $\overline{\eta}_r'$ is the average $\overline{\eta}_r'$ over $\Delta\omega$.

Also is the absorption coefficient of the cabin space

$$\bar{\alpha} = \frac{4 \omega V \overline{\eta}_n}{cS}$$

where S is the absorbing surface area.

Equation (19) is limited to frequencies where n_r, $\overline{\eta}_r$, $\overline{M}_r$, $j_r^2(\omega)$, $j_r^2(\omega)^{\mathrm{rev}}$, and $\overline{\eta}_n$ can be calculated or estimated to a high level of confidence. The band average acoustic loss factor $\overline{\eta}_n$ is computed with

$$\overline{\eta}_n = \frac{2c}{\omega V}(\lambda\xi) \tag{20}$$

where $\xi = \mathrm{Re}[\beta]$ is the sidewall conductance (calculated with equation (4)). Note that no acoustic modal data is required in equation (19). Also note that structural modal properties are wrapped in the joint acceptance functions. What becomes important are the wavenumbers of the structural modes (i.e., their distribution, in general, as one moves across the various frequency bands). Since joint acceptances for higher frequencies are insensitive to boundary conditions (especially for TBL excitation), these functions are usually very well behaved, and often asymptote at a low enough frequency to allow their estimation to extremely high frequencies.

Structural Model

The fuselage structural mode shapes are of the following forms:

Symmetric modes:

$$\psi^r(\bar{x}) = \psi^r(z,\theta) = \phi_M(z) \sum_{n=0}^{n^*} (-1)^n C_{Mn}^r \cos n\theta$$

Antisymmetric modes:

$$\psi^r(\bar{x}) = \psi^r(z,\theta) = \phi_M(z) \sum_{n=1}^{n^*} (-1)^n C_{Mn}^r \sin n\theta$$

The C_{Mn}^r are the generalized coordinates for the bending deflections of the fuselage (with floor) that describe the circumferential mode shape. These coefficients must be computed for the stiffened composite fuselage. The C_{Mn}^r, resonance frequencies ω_r, and modal masses M_r are computed with the structure program MRPCOMP (the composite fuselage structures program). The C_{Mn}^r form an (approximately) orthogonal set of vectors (column matrices) for modes that are predominantly bending modes (modes having mainly energy in bending of sidewall or floor). For those type modes, the $\psi^r(\bar{x})$ are (approximately) an orthogonal set. Neither the $C_M^r n$ nor the $\psi^r(\bar{x})$ are orthogonal for fuselage modes that are predominantly stretching (dilatational) modes. But this is of no consequence, since M_r takes large values for those modes (relative to the M_r of bending modes), and in effect "throws out" the stretching modes.

Excitation models

The excitation is described by the joint acceptance functions

$$j_r^2(\omega) = \frac{1}{X_e^2} \int_{X_e} \int_{X_e'} C_{pb1}(\bar{x}/\bar{x}';\omega)\psi^r(\bar{x})\psi^r(x')d\bar{x}d\vec{x}' \tag{21}$$

The above reduces to

$$j_r^2(\omega) = j_M^2(\omega) \cdot j_N^2(\omega)$$

$$j_N^2(\omega) \cong \sum_n (C_{Mn}^r)^2 \, j_n^2(\omega)$$

The axial component is

$$j_M^2(\omega) = \int_0^1 \int_0^1 C_z[L(z_1 - z_2);\omega] \; \phi_M(z_1) \; \phi_M(z_2) dz_1 dz_2$$

where $z_1 = z/L$; $z_2 = z'/L$

Here, for either progressive acoustic wave with decaying coherency or turbulent boundary layer noise

$$C_z[L(z_1-z_2);\omega] = \exp\left[-\ {}_z\left|z_1-z_2\right|\right]\cos\bar{k}_z(z_1-z_2)$$

$$\bar{\delta}_z = \delta_z L;\ \bar{k}_z = k_z L;\ k_z = \omega/U_c$$

and from Reference (B8), with U as the free stream velocity U_c as the convection velocity, and δ^* as the boundary layer displacement thickness

$$\delta_z = \frac{\omega}{U_c}\left\{(0.1)^2 + \frac{0.034U_c\ ^2}{\omega\delta^*}\right\}^{1/2}$$

$$\frac{U_c}{U\infty} = 0.59 + 0.3\exp[-0.89S]$$

$$S = \omega_{\delta}{}^*/U\infty$$

$$\frac{\delta^*}{z} = \frac{0.37}{8}Re_z{}^{-0.2}\left\{1 + \left(\frac{Re_z}{2.9 \times 10^7}\right)^2\right\}^{0.1}$$

$$Re_z = \frac{U\infty z}{\nu},\ \nu = \text{kinematic viscosity}$$

The circumferential components of the joint acceptance are

<u>Symmetric modes</u>

$$j_n^2(\omega) \qquad j_n^2(\omega,\psi) = \int_0^1\int_0^1 C_y[2\pi a(y_1\ y_2);\omega]\cos 2n\pi y_1 \cos 2n\pi y_2\, dy_1 dy_2$$

Antisymmetric modes

$$j_n^2(\omega)\, j_n^2(\omega,\phi) = \int_0^1 \int_0^1 C_y[2\pi a(y_1 \; y_2);\omega] \sin 2n\pi y_1 \sin 2n\pi y_2 \, dy_1 dy_2$$

where

$$C_y[2\pi a(y_1 - y_2);\omega] = \exp\,[-\bar{\delta}_y |y_1 - y_2|]$$

$$y_1 = y/2\pi a;\; y_2 = y'/2\pi a$$

$$\delta_y = 2\pi a \delta_y$$

$$\delta_y = \frac{\omega}{U_c} \left\{ 0.72^2 + \left(\frac{0.244 U_c}{\omega \delta^*} \right)^2 \right\}^{1/2}$$

The local pressure spectrum at distance z from the nose of the aircraft is

$$S_{\rho_{b1}}(\omega) = \left(\frac{0.006q}{1 + 0.14\, M^2} \right)^2 \frac{*}{U_\omega (1 + 2^2)^{3/2}}$$

where M is the Mach number and $q = 1/2\ \rho_o U_\infty^2$ is the dynamic head.

In the interest of brevity, the joint acceptances are not presented.

Discrete Stiffener Methodology

The discrete stiffeners are modeled through their strain and kinetic energies as follows.

The strain energy for the longitudinal stringers can be written as,

$$U_{st} = \sum_{j=1}^{NST} \left(\iint_{A_s} \int_0^L \tfrac{1}{2} E_s \epsilon_{xt}^2 \, dAs \, dx + \int_0^L \tfrac{1}{2} G_s J_s \left(\frac{\partial \phi}{\partial x}\right)^2 dx \right)_j \qquad (22)$$

where

ϵ_{xt} = Longitudinal strain on element with area dAs at a distance z above the neutral surface of the shell wall = $\epsilon_x - z \dfrac{\partial ws}{\partial x}$

ϵ_x = $\dfrac{\partial us}{\partial x}$ = longitudinal strain at neutral surface of shell

θ = Twist of stiffener = $\dfrac{\partial ws}{\partial y}$

E_s = Young's modulus for stiffener material

$G_s J_s$ = Torsional stiffness of stiffener

NST = Number of stringers

U_s, V_s, W_s = Displacement components at neutral surface of shell

Substitution for ϵ_{xt} in equation (22) yields,

$$U_{st} = 1/2 \sum_{j=1}^{NST} \int_0^L \left\{ E_s \left[A_s \left(\frac{\partial u}{\partial x}\right)^2 - 2 \bar{z}_s \frac{\partial u_s}{\partial x} \frac{\partial^2 W_s}{\partial X^2} + I_{os} \left(\frac{\partial^2 W_s}{\partial x^2}\right)^2 \right] \right. \qquad (23)$$

$$\left. + G_s J_s \left(\frac{\partial^2 W_s}{\partial x \partial y}\right)^2 \right] dx$$

where the first term accounts for the stretching of the stringer, $z_s A_s E_s$ for the eccentricity of the centroid of the stiffener relative to the shell wall ($\bar{z}_s$ is the z-coordinate of the centroid relative to the middle surface of the shell), E_sI_{os} for the bending stiffness and G_sJ_s for the twisting stiffness of the stringer.

For a composite stiffener, it can be shown that these are given by (see Figure B-3 for the definition of the stiffener geometry),

$$E_sA_s = A^{W}_{11}\, h_{ST} + A^{TF}_{11}\, w_{s1} + A^{BF}_{11}\, w_{s2} \tag{24}$$

$$E_sA_s\bar{z}_s = \tfrac{1}{2}A^{W}_{11}\, h^{2}_{st} + w_{s1}A^{TF}_{11}\, h_{st} + w_{s2}A^{BF}_{11}\, z^{*} \tag{25}$$

$$E_sI_{os} = \frac{1}{3}A^{W}_{11}\, h^{3}_{ST} + w_{s1}\left[D^{TF}_{11} + A^{TF}_{11}\, h^{2}_{st}\right] + w_{s2}\left[D^{BF}_{11} + A^{BT}_{11}\,(z^{*})\right]^{2} \tag{26}$$

$$z^{*} = \tfrac{1}{2}\,(t_{s2} + h_{skin}) \tag{27}$$

$$G_sJ_s = 4\, D^{W}_{66}\,(h_{ST}-t_{s2}) + 4\left[D^{TF}_{66}\, w_{s1} + D^{BF}_{66}\, w_{s2}\right] \tag{28}$$

where A_{11}, D_{11}, D_{66} are standard extensional and bending stiffnesses of a composite laminate.

A similar expression can be written for the ring frames. Equation (23) for the longitudinal stringer and a similar one for the ring frames will be combined with the strain energy of the shell to generate a stiffness matrix for a discretely stiffened cylindrical shell. However, equation (23) involves only integration over the length of the shell with the angular coordinate being evaluated at the location of the stringer. A similar situation exists with the strain energy of the ring frame, viz, integration around the circumference of the shell with the axial coordinate evaluated at the longitudinal position of the ring frame. Both of these integrals will be

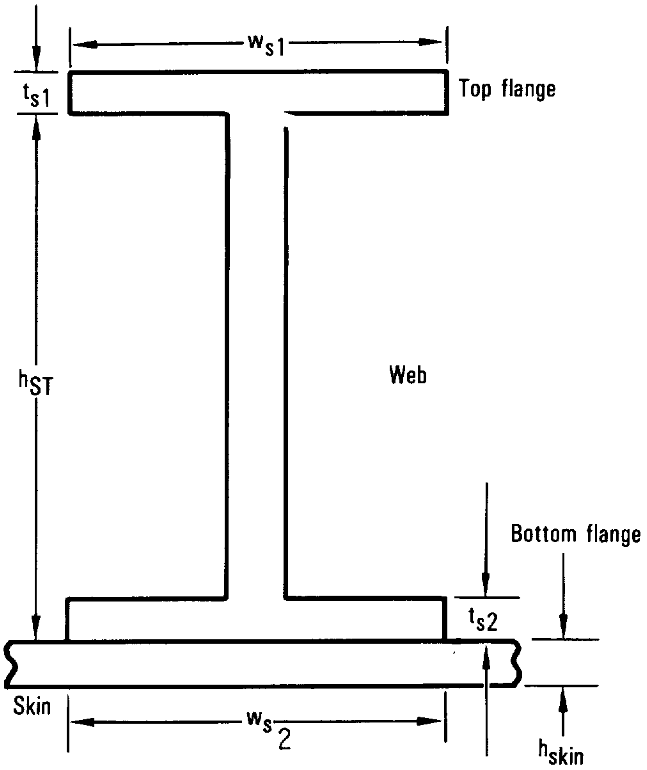

Figure B-3. - Geometry of stiffener.

added to the strain energy of the shell which involves double integration over the surface of the shell. To implement this addition, equation (23) can be rewritten as ($y = R\Theta$).

$$U_{ST} = 1/2 \sum_{j=1}^{NST} \int_{y=0}^{2\pi R} \int_{x=0}^{L} \delta(\theta - \theta_j) \left\{ E_s \left[A_s \left(\frac{\partial u_s}{\partial x}\right)^2 - 2\bar{z}_s A_s \left(\frac{\partial u_s}{\partial x}\right) \left(\frac{\partial^2 w_s}{\partial x^2}\right) + I_{0s} \left(\frac{\partial^2 w_s}{\partial x^2}\right) \right] + G_s J_s \left(\frac{\partial^2 w_s}{\partial x \partial y}\right)^2 \right\} dx\, dy \tag{29}$$

where $(\Theta - \Theta_j)$ is the Dirac delta function and has the properties

$$\delta(\theta - \theta_j) = 0 \text{ for } \theta \neq \theta_j \tag{30}$$

and,

$$\int_0^{2\pi} \delta(\theta - \theta_j) f(\theta)\, d\theta = f(\theta_j) \tag{31}$$

A similar relation exists for the frame, viz.,

$$U_F = 1/2 \sum_{k=1}^{NR} \int_{y=0}^{2\pi R} \int_{x=0}^{L} \delta(x - x_k) \left\{ E_R \left[A_r \left(\frac{\partial v_s}{\partial y} + \frac{w_s}{R} \right)^2 \right. \right.$$

$$\left. \left. - 2\bar{z}_R A_R \left(\frac{\partial^2 w_s}{\partial y^2} \right) \left(\frac{\partial v_s}{\partial y} + \frac{w_s}{R} \right) + I_{OR} \left(\frac{\partial^2 w_s}{\partial y^2} \right)^{2} \cdot \right] + G_R J_R \left(\frac{\partial^2 w_s}{\partial x \partial y} \right)^2 \right\} dx\, dy \tag{32}$$

Both u_{ST} and u_F are now in a form which can be directly added to the strain energy of the shell and a single integral obtained.

Mass matrices for the stiffened cylinder are derived from the kinetic energy expressions for the stringers and ring frames. For the stringers,

$$T_{ST} = 1/2 \sum_{\partial = 1}^{NST} \int_0^{2\pi R} \int_0^{L} \delta\,(\theta - \theta_j)\, \varrho_s \left[A_s\, (\dot{u}_s^2 + \dot{v}_s^2 + \dot{w}_s^2) + 1_p^s \left(\frac{\partial w_s}{\partial y} \right)^2 \right] dx\, dy \tag{33}$$

In equation (33), the terms multiplied by A (the cross-sectional area of the stringer) represents the translational kinetic energy, and the term multiplied by I_p (the polar moment of inertia about the middle surface of the shell wall) represents the rotational kinetic energy of the stringer. A similar expression exists for the ring frame,

$$T_F = 1/2 \sum_{k=1}^{NR} \int_0^{2\pi R} \int_0^{L} \delta\,(x - x_k)\, \varrho_R \left[A_R\, (\dot{u}_s^2 + \dot{v}_s^2 + \dot{w}_s^2) + I_P^R \left(\frac{\partial \overset{2}{\dot{w}}_s}{\partial x} \right)^2 \right] dx\, dy \tag{34}$$

In equation (33) and (34), the dot above the displacement component signifies a derivative with respect to time, in the standard fashion.

Cylinder Analysis

The preceding strain and kinetic energies for the stiffeners are added to those of the shell. Employing the shell theory known as the "Reissner-Naghdi-Berry" shallow shell theory, the strain energy for a laminated composite shell can be written as (y = Rθ).

$$U_{SH} = 1/2\int_{y=0}^{2\pi R}\int_{x=0}^{\ell} \{\sigma\}^T \{\varepsilon\}\, dx\, dy$$

$$= 1/2\int_{0}^{2\pi R}\int_{0}^{\ell} ([D]\, [G_s]\, \{u\}^T\, [G_s]\, \{u\}\, dx\, dy \tag{35}$$

Where

$$\{u\} = [U_s, V_s, W_s]^T = \text{vector of shell displacement components} \tag{36}$$

$$[D] = \begin{bmatrix} [A_{ij}] & [0] \\ [0] & [D_{ij}] \end{bmatrix} = [D]^T \tag{37}$$

$$[G_s] = \begin{bmatrix} \frac{\partial}{\partial x} & 0 & \frac{1}{r}\frac{\partial}{\partial \theta} & 0 & 0 & 0 \\ 0 & \frac{1}{r}\frac{\partial}{\partial \theta} & \frac{\partial}{\partial x} & 0 & \frac{1}{r^2}\frac{\partial}{\partial \theta} & \frac{1}{r}\frac{\partial}{\partial x} \\ 0 & \frac{1}{r} & 0 & \frac{-\partial^2 w}{\partial_x{}^2} & \frac{-1}{r^2}\frac{\partial^2}{\partial \theta^2} & \frac{-2}{r}\frac{\partial^2}{\partial x \partial \theta} \end{bmatrix}^T \tag{38}$$

$$[A_{ij}] = \begin{bmatrix} A_{11} & A_{12} & A_{16} \\ A_{12} & A_{22} & A_{26} \\ A_{16} & A_{26} & A_{66} \end{bmatrix} \tag{39}$$

$$[D_{ij}] = \begin{bmatrix} D_{11} & D_{12} & D_{16} \\ D_{12} & D_{22} & D_{26} \\ D_{16} & D_{26} & D_{66} \end{bmatrix} \tag{40}$$

Equations (39) and (40) are the stretching and bending matrices, respectively, for a laminated composite shell. The total strain energy for the discretely stiffened shell is then the sum of equations (35), (29) and (32),

$$U_{CYL} = U_{SH} + U_{ST} + U_F \tag{41}$$

The same can be said for total kinetic energy,

$$T_{CYL} = T_{SH} + T_{ST} + T_F \tag{42}$$

where,

$$T_{SH} = 1/2 \int_0^{2\pi R} \int_0^L \rho_{SH} t(\dot{u}_s^2 + \dot{v}_s^2 + \dot{w}_s^2)\, dx\, dy \tag{43}$$

and where t is the thickness of the shell wall and $_{SH}$ is the mass density of the shell material. The terms T_{ST} and T_F are given in equations (33) and (34).

The displacements of the shell are taken in the form of the finite series,

$$u_s = \sum_{M=0}^{M^*} \sum_{n=0}^{n^*} U^s_{Mn} \, X_{uM}(x) \, \psi_{un}(\theta)$$

$$v_s = \sum_{M=0}^{M^*} \sum_{n=0}^{n^*} V^s_{Mn} \, X_{vM}(x) \, \psi_{vn}(\theta)$$

$$w_s = \sum_{M=0}^{M^*} \sum_{n=0}^{n^*} w^s_{Mn} \, X_{wM}(x) \, \psi_{wn}(\theta) \qquad (44)$$

which can be cast into the matrix form,

$$\{u\} = \begin{Bmatrix} u_s \\ v_s \\ w_s \end{Bmatrix} = [N_s]\,\{q_s\} \qquad (45)$$

where, $[N_s]$ is a matrix of size 3x3M*n* and

$$\{q_s\} = \begin{Bmatrix} \bar{u}_s \\ \bar{v}_s \\ \bar{w}_s \end{Bmatrix} = \text{vector of shell generalized coordinates} \qquad (46)$$

$$\{\bar{u}_s\} = \left\{\begin{bmatrix} U_{00} \\ U_{01} \\ \vdots \\ U_{0n^*} \\ U_{1n^*} \\ \vdots \\ U_{M^*n^*} \end{bmatrix}\right\}, \{\bar{v}_s\} = \left\{\begin{bmatrix} V_{00} \\ V_{01} \\ \vdots \\ V_{0n^*} \\ V_{1n^*} \\ \vdots \\ V_{M^*n^*} \end{bmatrix}\right\}, \{\bar{w}_s\} = \left\{\begin{bmatrix} W_{00} \\ W_{01} \\ \vdots \\ W_{0n^*} \\ W_{1n^*} \\ \vdots \\ W_{M^*n^*} \end{bmatrix}\right\} \tag{47}$$

and where $[N_x]$ is a matrix of the functions $\underline{\overline{X}}$ and ψ from equation (44).

Substitution of equation (43) into equation (41) leads to a matrix equation of the form,

$$U_{CYL} = \tfrac{1}{2} \{q_s\}^T [K_s] \{q_s\} \tag{48}$$

where $[K_s]$ is the stiffness matrix for the stiffened cylinder (without a floor).

In a similar manner, the kinetic energy of the stiffened cylinder can be put into the form,

$$T_{CYL} = \tfrac{1}{2} \{q_s\}^T [M_s] \{\dot{q}_s\} \tag{49}$$

where M_s is the mass matrix. In terms of matrix $[N_s]$, the shell stiffness and mass matrices are given by.

$$[K_s]_{shell} = \int_0^{2\pi R} \int_0^{L} [N_s]^T [G_s]^T [D] [G_s] [N] \, dx \, dy \tag{50}$$

and,

$$[M_s]_{shell} = \int_0^{2\pi R} \int_0^{L} \varrho S H^t \, [N_s]^T \, [N_s] \, dx \, dy \tag{51}$$

In addition to (50) and (51) for the shell there are the contributions for the discrete stiffeners.

The floor is modeled in the same way as the cylinder except that the floor itself is a flat plate, rather than a cylinder. Stiffeners are modeled in exactly the same manner as for the cylinder. The resulting strain and kinetic energies have the form (the floor displacements are expanded similarly to the cylinder),

$$U_p = ½ \, \{q_p\}^T \, [K_p] \, \{q_p\} \tag{52}$$

and,

$$T_p = ½ \, \{\dot{q}_p\}^T \, [M_p] \, \{q_p\} \tag{53}$$

The total strain and kinetic energies for the stiffened cylinder and floor are given by,

$$U = U_{CYL} + U_p = ½ \begin{Bmatrix} q_s \\ q_p \end{Bmatrix}^T \begin{bmatrix} \overline{K}_s & 0 \\ 0 & K_p \end{bmatrix} \begin{Bmatrix} q_s \\ q_p \end{Bmatrix} = ½ \, \{q\}^T \, [K^*] \, \{q\} \tag{54}$$

and,

$$T = 1/2 \begin{Bmatrix} \dot{q}_s \\ \dot{q}_p \end{Bmatrix}^T \begin{bmatrix} M_s & 0 \\ 0 & M_p \end{bmatrix} \begin{Bmatrix} \dot{q}_s \\ \dot{q}_p \end{Bmatrix} = 1/2 \{\dot{q}\}^T [M^*] \{\dot{q}\}, \tag{55}$$

where,

$$\{q\} = \begin{Bmatrix} q_s \\ q_p \end{Bmatrix},$$

is the combined vector of all the generalized coordinates of the shell and plate.

The components of the coordinate vector q are not independent because constraint equations must be introduced to insure displacement compatibility at the interface between the plate and shell. The floor partition can be taken to be fixed or pinned along the line of attachment to the shell. For a rigid attachment, the shell and plate displacements obey the relations (see Figure B-4) for shell-floor geometry),

$$\begin{aligned} & u_s = u_p \\ & w_s \sin\theta_1 + v_s \cos\theta_1 = v_p \\ & w_s \cos\theta_1 - v_s \sin\theta_1 = w_p \\ & \frac{v_s}{r} - \frac{1}{r}\frac{\partial w_s}{\partial \theta} + \frac{\partial w_p}{\partial y} = 0 \end{aligned} \tag{56}$$

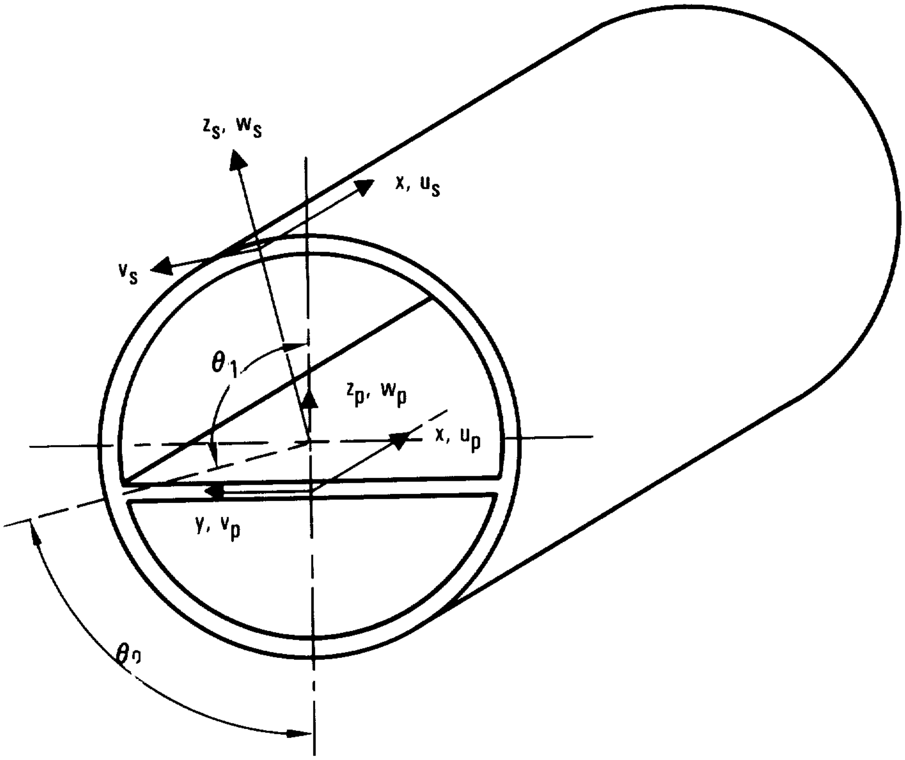

Figure B-4. - Circular cylindrical shell with a longitudinal partition.

In the case of a hinged connection the last equation is dropped. The equation in (56) can be put into matrix form,

$$[c]\{q\} = \{0\} \tag{57}$$

Applying Hamilton's Principle and adjoining the constraint equations by introducing a vector of Lagrange multipliers in the standard way leads to the equations of motion, and constraint, for the system.

If $\{q\}$ is partitioned into a set of independent coordinates $\{q_1\}$ and dependent coordinates $\{q_2\}$, the constraint equations can be manipulated and the dependent coordinates and Lagrange multipliers can be algebraically eliminated. The equations of motion then take the form:

$$[M]\{\ddot{q}_1\} + [K]\{q_1\} = \{0\}, \qquad (58)$$

in which

$$[M] = [E]^T [M^*] [E], \; [K] = [E]^T [K^*] [E], \qquad (59)$$

where

$$[E] = \left[\begin{array}{c} I \\ \hline [C_2]^{-1} [C_1] \end{array}\right], \qquad (60)$$

and C_1 and C_2 are obtained from the partitioned constraint equations

$$\left[C_1 \; \vdots \; C_2\right] \begin{Bmatrix} q_1 \\ q_2 \end{Bmatrix} = \{0\} \qquad (61)$$

The eigenvalue problem for the frequencies and mode shapes of the discretely stiffened shell with floor is finally obtained by letting $\{q^1\}$ be harmonic with time, which yields

$$[K]\{q_1\} = \omega^2 [M]\{q_1\} \qquad (62)$$

The eigenvalues of equation (62) are the natural frequencies of the shell structure with floor. From the corresponding eigenvectors, the mode shapes can be calculated.

In this study, the longitudinal plate function $\overline{\underline{X}}$ (x) are the same for the plate and the shell. These functions are expressed in terms of a single function $\theta_{M(x)}$ according to

$$X_{uM} = \phi'_M(x)$$

$$X_{vM} = \phi_M(x)$$

$$X_{wM} = \phi_M(x)$$

The functions $\phi_M(x)$ are the mode shapes of a uniform beam. The boundary conditions used in this study are those of a simply supported beam, so $\phi_M(x) = \sin M\pi x/L$. The circumferential functions for the symmetric (about the shell centerline) modes of the shell are,

$$\psi_{un} = \cos n\theta$$

$$\psi_{vn} = \sin n\theta$$

$$\psi_{wm} = \cos n\theta$$

for the antisymmetric modes,

$$\psi_{un} = \sin n\theta$$

$$\psi_{vn} = -\cos n\theta$$

$$\psi_{wn} = \sin n\theta$$

A similar set is used for the symmetric and antisymmetric modes of the plate (floor)

Stiffened Shell Equations

The previous analysis was valid for a monocoque composite cylinder. In this section, the additional terms necessary to include the effects of discrete stiffeners are given. As with the shell, the discrete stiffeners are modeled through their strain and kinetic energies.

The strain energy for a longitudinal stringer can be written as

$$U_{ST} = \sum_{j=1}^{NST}\left(\int_{X=0}^{L}\iint_{A_S} 1/2\, E_S \epsilon_{XT}{}^2\, dA_S\, dX + \int_{X=0}^{L} 1/2\, G_S J_S \left(\frac{\partial \phi}{\partial X}\right)^2 dX\right)_j \tag{63}$$

where

ϵ_{xt} = longitudinal strain on element with area dAs at a distance z above the neutral surface of the shell wall = $E_x - z \dfrac{\partial \omega_s}{\partial x}$

$\epsilon_x = \dfrac{\partial \eta_s}{\partial x}$ = longitudinal strain at neutral surface of shell

ϕ = twist of stringer = $\dfrac{\partial \omega_s}{\partial y}$

and where E_s, G_sJ_s, and N_{st} are Young's modulus, torsional stiffness of the stiffener, and number of stringers, respectively.

Substitution for ϵ_{xt} in equation (63) yields (y=R)

$$U_{ST} = 1/2 \sum_{j=1}^{NST} \int_{X=0}^{L} \left\{ E_S \left[A_S\left(\frac{\partial U_S}{\partial X}\right)^2 - 2z_S\left(\frac{\partial U_S}{\partial X}\right)\left(\frac{\partial^2 W_S}{\partial X^2}\right) + I_{OS}\left(\frac{\partial^2 W_S}{\partial X^2}\right)^2\right] + G_S J_S \left(\frac{\partial^2 W_S}{\partial X \partial Y}\right)^2 \right\} \partial X \tag{64}$$

where the first term accounts for the stretching of the stringer, $\bar{z}_s A_s E_s$ for the eccentricity of the centroid of the stiffener relative to the shell wall ($\bar{z}_s$ is the z-coordinate of the centroid of the stiffener), $E_s I_{os}$ for the bending stiffness and $G_s J_s$ for the twisting stiffness of the stringer.

In equation (64), the jth stringer is to be evaluated at a specific circumferential position $\theta = \theta_j$. It will be convenient to refer all strain energies to an integration over the entire surface of the shell. Accordingly, equation (64) can be rewritten as

$$U_{ST} = 1/2 \sum_{j=1}^{NST} \int_{\theta=0}^{2\pi} \int_{X=0}^{L} \delta(\theta - \theta_j) \left\{ E_S \left[A_S \left(\frac{\partial U_S}{\partial X}\right)^2 - 2\bar{z}_S A_S \left(\frac{\partial U_S}{\partial X}\right)\left(\frac{\partial^2 W_S}{\partial X^2}\right) + I_{OS}\left(\frac{\partial^2 W_S}{\partial X^2}\right)^2 \right] + \frac{G_S J_S}{R^2}\left(\frac{\partial^2 W_S}{\partial X \partial \theta}\right)^2 \right\} dX\, R\, d\theta \quad (65)$$

where $\delta(\theta - \theta_j)$ is the Dirac delta function which has the properties

$$\delta(\theta - \theta_j) = 0 \text{ for } \theta \neq \theta_j \quad (66)$$

and

$$\int_0^{2\pi} \delta(\theta - \theta_j)\, f(\theta)\, d\theta = f(\theta_j)$$

Similarly for the ring frames,

$$U_R = 1/2 \sum_{k=1}^{NR} \int_0^{2\pi}\int_0^{L} \delta(X - X_k) \left\{ E_R \left[A_R \left(\frac{1}{R}\frac{\partial V_S}{\partial \theta} + \frac{W_S}{R}\right)^2 - 2\bar{z}_k \frac{A_R}{R^2}\frac{\partial^2 W_S}{\partial^2 \theta^2}\left(\frac{1}{R}\frac{\partial V_S}{\partial \theta} + \frac{W_S}{R}\right) + \frac{I_{OR}}{R^4}\left(\frac{\partial^2 W_S}{\partial \theta^2}\right)^2 \right] + \frac{G_R J_R}{R^2}\left(\frac{\partial^2 W_S}{\partial X \partial \theta}\right)^2 \right\} dX\, R\, d\theta \quad (67)$$

where each ring is located at $x=x_k$, there are "NR" rings, and $(x-x_k)$ is also a delta function.

Using equation (45), U_{st} and U_r can be written in the form

$$U_{ST} = 1/2 \left\{q_S\right\}^T [K_{ST}] \left\{q_S\right\} \tag{68}$$

$$U_R = 1/2 \left\{q_S\right\}^T [K_R] \left\{q_S\right\} \tag{69}$$

where $[K_{st}]$ and $[K_R]$ are stiffness matrices for the stringers and ring frames. The total strain energy is the sum of U_{SH}, U_{ST} and U_R, giving

$$U_S = 1/2 \left\{q_S\right\}^T [K_S] \left\{q_S\right\} \tag{70}$$

where $[K_s]$ is the stiffness matrix for the stiffened shell and is given by

$$[K_S] = [K_{SH}] + [K_{ST}] + [K_R] \tag{71}$$

The same approach can be used for the mass matrix of the stiffened shell. For the j^{th} longitudinal stringer, the most important contributions to the kinetic energy of the stringer are those due to translation and to twisting of the stiffener, so that

$$T_j = 1/2 \int_0^L \varrho_{ST} \left[A_S \left(\dot{W}_S{}^2 + \dot{V}_S{}^2 + \dot{U}_S{}^2\right) + I_\varrho^{ST} \dot{\varphi}^2\right]_j dX \tag{72}$$

In equation (72), the first term represents the translational kinetic energy of the stringer, and the second term the rotational kinetic energy of the stringer. I_p^{ST} is the polar moment of inertia of the stiffener cross-section about the middle surface of the shell, and $\theta = \frac{1}{R} \frac{\partial \omega_s}{\partial \theta}$. Summing over all stringers and expanding the integral to a surface integral,

$$T_{ST} = 1/2 \sum_{j=1}^{NST} \int_0^{2\pi} \int_0^{L} \delta(\theta - \theta_j)\, \rho_S \left[A_S \left(\dot{W}_s^2 + \dot{V}_S^2 + \dot{U}_S^2 \right) + I_\rho^{ST} \left(\frac{1}{R} \frac{\partial \dot{W}_S}{\partial \theta} \right)^2 \right] dX\, R\, d\theta \qquad (73)$$

For the ring frames,

$$T_R = 1/2 \sum_{k=1}^{NR} \int_0^{2\pi} \int_0^{L} \delta(X - X_k)\, \rho_R \left[A_R \left(\dot{W}_S^2 + \dot{V}_S^2 + \dot{U}_S^2 \right) + I_\rho^{R} \left(\frac{\partial \dot{W}}{\partial X} \right)^2 \right] dX\, R\, d\theta \qquad (74)$$

Use of equation (45) permits T_{ST} and T_R to be written in the form

$$\begin{aligned} T_{ST} &= 1/2 \left\{ \dot{q}_S \right\}^T \left[M_{ST} \right] \left\{ \dot{q}_S \right\} \\ T_R &= 1/2 \left\{ \dot{q}_S \right\}^T \left[M_R \right] \left\{ \dot{q}_S \right\} \end{aligned} \qquad (75)$$

where $[M_{ST}]$ and $[M_R]$ are mass matrices for the assembly of stringers and ring frames. Adding the kinetic energies for the shell, the stringers, and ring frames gives

$$\begin{aligned} T_{\substack{\text{STIFFENED} \\ \text{SHELL}}} &= T_{SH} + T_{ST} + T_R \\ &= 1/2 \left\{ \dot{q}_S \right\}^T \left[M_S \right] \left\{ \dot{q}_S \right\} \end{aligned} \qquad (76)$$

where the mass matrix for the stiffened shell is given by

$$[M_S] = [M_{SH}] + [M_{ST}] + [M_R] \qquad (77)$$

Floor Partition

The floor of the fuselage is modeled as a stiffened composite panel. Proceeding in a manner similar to that used for the shell, the strain energy for the plate is given by

$$U_P = 1/2 \int_{Y=-b}^{b} \int_{X=0}^{L} \{\widetilde{U}_P\}^T [G_P]^T [0] [G_P] \{\widetilde{U}_P\} \, dXdY \tag{78}$$

where

$$\{\widetilde{U}_P\}^T = [U_P, V_P, W_P] \tag{79}$$

is a vector of floor displacement components, [D] is given by equation

$$\left[\begin{array}{c|c} A_{ij} & B_{ij} \\ \hline B_{ij} & D_{ij} \end{array}\right]$$

and $[G_p]$ is the matrix differential operator given by

$$[G_P]^T = \left[\begin{array}{c|c|c|c|c|c} \partial/\partial X & 0 & \partial/\partial Y & 0 & 0 & 0 \\ \hline 0 & \partial/\partial Y & \partial/\partial X & 0 & 0 & 0 \\ \hline 0 & 0 & 0 & -\dfrac{\partial^2}{\partial X^2} & -\dfrac{\partial^2}{\partial Y^2} & -2\dfrac{\partial^2}{\partial X \partial Y} \end{array}\right] \tag{80}$$

The plate displacements are also expanded in a finite series

$$\begin{aligned} U_P &= \sum_{m=0}^{m^*} \sum_{n=0}^{n^*} U^P_{mn} \, X_{Um}(X) \, \xi_{Un}(Y) \\ V_P &= \sum_{m=0}^{m^*} \sum_{n=0}^{n^*} V^P_{mn} \, X_{Vm}(X) \, \xi_{Vn}(Y) \\ W_P &= \sum_{m=0}^{m^*} \sum_{n=0}^{n^*} W^P_{mn} \, X_{Wm}(X) \, \xi_{Wn}(Y) \end{aligned} \tag{81}$$

The longitudinal functions are the same as those used for the shell and are given by equations

$$X_{uM} = \phi'_M (x)$$

$$X_{vM} = \phi_M (x)$$

$$X_{wM} = \phi_M (x)$$

The functions $\phi_M(x)$ are the mode shapes of a uniform beam. The boundary conditions used in this study are those of a simply supported beam, so $\phi_M(x) = \sin M x/L$.

The plate transverse functions are:

For symmetric modes,

$$\xi_{Un} = \cos \frac{n\pi Y}{2b}$$

$$\xi_{Vn} = \sin \frac{n\pi Y}{2b} \tag{82}$$

$$\xi_{Wn} = \cos \frac{n\pi Y}{2b}$$

For antisymmetric modes,

$$\xi_{Wn} = \cos \frac{n\pi Y}{2b}$$

$$\xi_{Un} = \sin \frac{n\pi Y}{2b}$$

$$\xi_{Vn} = -\cos \frac{n\pi Y}{2b} \tag{83}$$

$$\xi_{Wn} = \sin \frac{n\pi Y}{2b}$$

Writing the plate expansion in matrix form,

$$\{\widetilde{U}_p\} = \begin{Bmatrix} U_p \\ V_p \\ W_p \end{Bmatrix} = [N_p]\{q_p\} \tag{84}$$

where $[N_p]$ is a 3x3m*n* matrix of the $X(x)$ and $\zeta(y)$ functions, and $\{q_p\}$ is a vector of plate displacement generalized coordinates similar to those defined for the shell in equation (47).

Using equation (84) in equation (78) leads to

$$U_p = 1/2\{q_p\}^T [K_p]\{q_p\} \tag{85}$$

where the floor stiffness matrix is derived from

$$[K_p] = \int_{-b}^{b} \int_{0}^{L} [N_p]^T [G_p]^T [D] [G_p] [N_p]\, dX\, dY \tag{86}$$

This matrix is augmented for the contributions of longitudinal and transverse stiffeners, as was done for the stiffened shell in equation (71).

The kinetic energy of the stiffened plate has the same form as the stiffened shell, so that

$$T_p = 1/2\{\dot{q}_p\}^T [M_p]\{q_p\} \tag{87}$$

where the mass matrix for the plate is

$$[M_p] = \int_{-b}^{b} \int_{0}^{L} (\varrho p h) [N_p]^T [N_p]\, dX\, dY \tag{88}$$

and is augmented for the contributions of the stiffeners, as was done in equation (77).

Coupling of Shell and Floor: Constraint Equations

The total strain energy for the coupled stiffened shell and floor system can be written in the form

$$U = U_S + U_P = 1/2 \begin{Bmatrix} q_S \\ q_p \end{Bmatrix}^T \begin{bmatrix} K_S & 0 \\ 0 & K_P \end{bmatrix} \begin{Bmatrix} q_S \\ q_P \end{Bmatrix} = 1/2 \{q\}^T [K^*] \{q\} \tag{89}$$

where [K*] is the uncoupled structural stiffness matrix, and where

$$\{q\} = \begin{Bmatrix} q_S \\ q_P \end{Bmatrix} \tag{90}$$

is the combined vector of all generalized coordinates of the shell and plate.

In a similar fashion, the total kinetic energy for the system is the sum of the kinetic energies for the shell and panel,

$$T = T_S + T_P = 1/2 \begin{Bmatrix} \dot{q}_S \\ \dot{q}_P \end{Bmatrix}^T \begin{bmatrix} M_S & 0 \\ 0 & M_P \end{bmatrix} \begin{Bmatrix} \dot{q}_S \\ \dot{q}_P \end{Bmatrix} = 1/2 \{\dot{q}\}^T [M^*] \{q^*\} \tag{91}$$

where [M*] is the uncoupled mass matrix for the entire stiffened structure.

The components of the coordinate vector $\{q\}$ are not independent because the constraint equations must be introduced to insure displacement compatibility at the interface between the plate and shell. The floor partition can be taken to be fixed or pinned along the line of attachment to the shell. For a rigid attachment, the shell and plate displacements obey the relations

$$
\begin{aligned}
&u_s = u_p \\
&w_s \sin\theta_1 + v_s \cos\theta_1 = v_p \\
&w_s \cos\theta_1 - v_s \sin\theta_1 = w_p \\
&\frac{v_s}{r} - \frac{1}{r}\frac{\partial w_s}{\partial \theta} + \frac{\partial w_p}{\partial y} = 0
\end{aligned}
\qquad (92)
$$

In the case of a hinged connection the last equation is dropped.

The equations in (92) can be put into the form after substitution of equations (45), (84), and (90).

$$[C]\{q\} = \{0\} \qquad (93)$$

Applying Hamilton's Principle and adjoining the constraint equations by introducing a vector of Lagrange multipliers in the standard way leads to the equations of motion and constraint for the system.

If $\{q\}$ is partitioned into a set of independent coordinates $\{q_1\}$ and dependent coordinates $\{q_2\}$, the constraint equations can be manipulated and the dependent coordinates and Lagrange multipliers can be algebraically eliminated. The equations of motion then take the form:

$$[M]\{\ddot{q}_1\} + [K]\{q_1\} = \{0\} \qquad (94)$$

in which

$$[M] = [E]^T [M^*] [E] , [K] = [E]^T [K^*] [E] \qquad (95)$$

where

$$[E] = \left[\begin{array}{c} I \\ \hdashline [C_2]^{-1}\,[C_1] \end{array}\right] \tag{96}$$

and C_1 and C_2 are obtained from the partitioned constraint equations

$$\left[C_1 \,\vdots\, C_2\right] \begin{Bmatrix} q_1 \\ q_2 \end{Bmatrix} = [0] \tag{97}$$

The eigenvalue problem for the frequencies and mode shapes of the discretely stiffened shell with floor is finally obtained by letting $\{q_1\}$ be harmonic with time, which yields

$$[K]\,\{q_1\} = \omega^2\,[M]\,\{q_1\} \tag{98}$$

The eigenvalues of equation (98) are the natural frequencies of the stiffened shell-floor structure. From the corresponding eigenvectors, the mode shapes can be calculated.

REFERENCES

B1 Pope, L.D., Wilby, E.G., and Wilby, J.F., "Propeller Aircraft Interior Noise Model," NASA CR-3813, 1984.

B2 Pope, L.D., and Wilby, J.F., "Band-Limited Power Flow into Enclosures," JASA, 62, 906-911 (1977).

B3 Pope, L.D., and Wilby, J.F., "Band-Limited Power Flow into Enclosures, II," JASA, 67, 823-826 (1980).

B4 Pope, L.D., Rennison, D.C., Willis, C.M., and Mayes, W.H., "Development and Validation of Preliminary Analytical Models for Aircraft Interior Noise Prediction," JSV 82 (4), 541-575 (1982).

B5 Pope, L.D., Wilby, E.G., Willis, C.M., and Mayes, W.H., "Aircraft Interior Noise Models: Sidewall Trim, Stiffened Structures, and Cabin Acoustics with Floor Partition," JSV 89 (3), 371-417 (1983).

B6 Pope, L.D., "Propeller Aircraft Interior Noise Model: Utilization Study and Validation," NASA CR 172428 (1984).

B7 Wilby, J.F., Piersol, A.G., and Wilby, E.G., "An Evaluation of Space Shuttle STS-2 Payload Bay Acoustic Data and Comparison with Predictions," Bolt Berancek and Newman, Inc., Report No. 4748 (1982).

B8 Lowson, M.V., "Prediction of Boundary Layer Pressure Fluctuations," AFFDL-TR-67-167 (1968).

1. Report No. NASA CR-4035	2. Government Accession No.	3. Recipient's Catalog No.

4. Title and Subtitle Transport Composite Fuselage Technology—Impact Dynamics and Acoustic Transmission	5. Report Date December 1986 6. Performing Organization Code
7. Author(s) A. C. Jackson, F. J. Balena, W. L. LaBarge, G. Pei, W. A. Pitman, and G. Wittlin	8. Performing Organization Report No. LR 31038
9. Performing Organization Name and Address Lockheed-California Company P.O. Box 551 Burbank, CA 91520	10. Work Unit No. 11. Contract or Grant No. NAS1-17698
12. Sponsoring Agency Name and Address National Aeronautics and Space Administration Washington, DC 20546	13. Type of Report and Period Covered Contractor Report 14. Sponsoring Agency Code

15. Supplementary Notes

Langley Technical Monitor: Marvin Dow
Final Report

16. Abstract

A program was performed to develop and demonstrate the impact dynamics and acoustic transmission technology for a composite fuselage which meets the design requirements of a 1990 large transport aircraft without substantial weight and cost penalties.

The program developed the analytical methodology for the prediction of acoustic transmission behavior of advanced composite stiffened shell structures. The methodology predicted that the interior noise level in a composite fuselage due to turbulent boundary layer will be less than in a comparable aluminum fuselage. The verification of these analyses will be performed by NASA Langley Research Center using a composite fuselage shell fabricated by filament winding.

The program also developed analytical methodology for the prediction of the impact dynamics behavior of lower fuselage structure constructed with composite materials. Development tests were performed to demonstrate that the composite structure designed to the same operating load requirement can have at least the same energy absorption capability as aluminum structure.

17. Key Words (Suggested by Author(s)) Composites, Fuselage, Acoustic Transmission, Impact Dynamics	18. Distribution Statement [redacted] Subject Category 24

19. Security Classif. (of this report) Unclassified	20. Security Classif. (of this page) Unclassified	21. No. of Pages 170	22. Price

[redacted]

NASA-Langley, 1986

[redacted]

[redacted]